LA-UR-20-30403
Approved for public release; distribution is unlimited.

Title: CISME report on experiments with HMX powder, PBX 9501 prills, and heated PBX 9501

Author(s): Holmes, Matthew David
Heatwole, Eric Mann
Broilo, Robert M.
Schulze, Peter Andreas
Feagin, Trevor Alexander
Erickson, Michael Andrew Englert
Dickson, Peter
Parker, Gary Robert Jr.

Intended for: Report

Issued: 2020-12-22

CISME report on experiments with HMX powder, PBX 9501 prills, and heated PBX 9501

Holmes, Matthew D.
Heatwole, Eric M.
Broilo, Robert M.
Schulze, Peter A.
Feagin, Trevor A.
Englert-Erickson, Michael A.
Dickson, Peter M.
Parker, Gary R.

Los Alamos National Laboratory
M-6 Explosives Applications and Special Projects
High Explosives Thermal and Mechanical Response Team

November 23, 2020

Abstract

The ability to predict post-ignition explosive response is relevant to explosives safety, particularly weapons assembly/disassembly operations that must operate under a sufficiently conservative safety basis to meet risk mitigation criteria for inadvertent nuclear detonation (IND). In particular, hazard determinations hinge on whether the PBX 9501 main charge can ultimately attain detonation from an initial, non-shock, ignition stimulus. The CISME experiment uses a spherical explosive charge, which is thermally ignited in the center using a fiber-delivered infrared laser pulse. This ignition mechanism—i.e. a localized thermal hotspot—is representative of the ignition-causing insults typical in accident scenarios, including low-velocity impact, drop, skid, and punch events. In fiscal year 2018 CISME experiments were conducted with pristine PBX 9501 spheres, confined and unconfined. Sub-detonative, low-violence reactions were observed. Here we report experiments conducted since 2018. The explosive charge was varied: experiments were conducted with room temperature pour-density HMX powder and prills of PBX 9501, and heated, thermally damaged PBX 9501. Experiments were conducted in a confined configuration, with two 4 mm-thick stainless-steel hemispherical shells bolted around the sphere. Detonation, via DDT (deflagration-to-detonation transition) was observed in the 3-inch diameter powdered HMX and the 6-inch diameter heated and thermally-damaged PBX 9501 tests. No transition to DDT was observed in smaller diameters for those configurations, and no DDT was observed for pour-density prills of PBX 9501 of any diameter. The original test series demonstrated that the response of pristine, undamaged PBX 9501 to a central ignition is relatively benign. This new test series shows that increased porosity, lack of polymer binders and thermal damage can greatly increase the violence of the post-ignition response, up to and including detonation. These results bridge the explosive response of PBX 9501 from sub-detonative through detonation as a function of diameter and provide valuable test cases for modeling efforts that strive to capture the DDT threshold. By exploring explosive response in a more representative 3D geometry, we can also benchmark these new results to more plentiful DDT datasets generated from testing in 1D tube confinement (the historical test configuration)–the configuration upon which almost all DDT models were developed.

Table 1. Test matrix summary of results.

	PBX 9501 prills	Heated PBX 9501	HMX powder
1.5 inch	Sub-detonative (test 6)	Not tested	VIOLENT, unlikely DDT (test 2)
3 inch	Sub-detonative (test 5)	VIOLENT, unlikely DDT (test 8)	DDT probable (test 1)
6 inch	Sub-detonative (test 4)	DDT probable (test 7)	Not tested
10 inch	VIOLENT, unlikely DDT (test 3)	Not tested	Not tested

Table of Contents

1. Introduction

The experiments reported here were motivated by the first round of testing that was performed in 2018 fiscal year. Minor alterations were made to the design, setup, and diagnostics from those original tests. The fiscal year 2018 report[1,2] should be considered an integral precursor to this report.

1.1. Summary of previous CISME experiments

The purpose of the fiscal year 2018 CISME experiment series was to determine whether pristine PBX 9501—i.e. thermally and mechanically undamaged material at nominal pressing density—could undergo DDT (deflagration-to-detonation transition) in a conservatively large, heavily confined charge, when ignited at the center of the charge. The intention was to correlate the HE response to radius length as the primary experimental variable.

Eight tests were conducted in 2018: a test matrix with diameters of 1.5 inch, 3 inch, 6 inch, and 10 inch in both confined and unconfined variations was completed. In no case was a violent response observed. The most violent outcome consisted of a pressure burst of the confined variations, accompanied occasionally by a brief, small, weak fireball. Uniformly, the bolts holding the two metal hemispherical shells failed, and the shells were ejected, somewhat deformed but intact, at velocities up to ≈75 m/s.

1.2. Focus for current CISME experiments

The relatively benign (as explosions go) response in the 2018 tests was encouraging from a viewpoint of explosives safety. However, for the purposes of model development, it is preferable to find a threshold in the behavior—to bridge the response from "no-go" to "go"—in order to provide a dataset that can exercise the ability to model a range of reaction violence. The initial round of testing did not yield any "go" results (i.e. DDT) that could be used to establish a threshold prediction.

Three explosive composition/condition scenarios were chosen for testing: unheated, neat HMX powder (no binder, pour-density), unheated PBX 9501 prills (with binder, pour-density), and heated, thermally damaged PBX 9501 (increased porosity and more sensitive delta-phase HMX).

It is well-known that increasing the porosity of a composition can increase the propensity to undergo DDT[3-6]. This is understood to be a consequence of both the increased surface area available for deflagration (particularly in the early stages of the deflagration) as well as a source for compressive heating as porosity provides opportunity for compaction (particularly in the latter stages of the DDT process).

Additionally, there exist representative, conservative accident scenarios in which higher-porosity explosive is created in the course of the incident. For example, a mechanical impact of the charge may crack and rubblize the explosive, increasing the effective porosity. A fuel fire causes thermal damage which volatilizes binder, induces a phase change in the HMX, and causes thermal expansion, all of which increase porosity.

HMX powder provides a worst-case proxy for the potential DDT response of PBX 9501. This is to say: though PBX 9501 is unlikely to exhibit *as violent* a response as HMX powder to accidental insults, it is extremely unlikely that it will exhibit a *more violent* response than HMX powder. HMX powder has been observed to DDT relatively easily, in numerous experiments with moderate confinement[3].

The slurry process that is used to synthesize PBX 9501 produces molding powder granules, or "prills," which are binder-coated globules of HMX crystals. Figure 1 is a photograph of PBX 9501 prills and HMX powder. The prills range in size, with a mean diameter of 1.82 ± 0.74 mm[7]. Using the prills at pour-density in the CISME test provides a material state that is hypothesized to exhibit an intermediate response between neat HMX powder and consolidated PBX 9501 and can be considered a condition representing severe mechanical damage (i.e. rubblizing damage) happening prior to ignition. Most importantly, when compared to neat HMX powder, it can elucidate the effects of binder on reaction violence evolution, while controlling for the variable of porosity.

Figure 1. Photos of PBX 9501 molding prills (left) and Class 1 HMX powder (right).

2. DDT background and dimensionality

The deflagration-to-detonation transition has been studied extensively over the past thirty years using quasi one-dimensional geometries, i.e. tubes. DDT tubes permit the confinement to be increased by strengthening and thickening the tube wall, while still allowing some diagnostic access. The original hypothesis for the "Type I" mechanism for DDT in consolidated material is presented in reference [4]. LANL has contributed considerably to that original hypothesis, particularly with regard to PBX explosives subjected to thermal damage. This work, and the current modern view of 1D DDT, is presented in reference [3].

A key element of the 1D DDT mechanism is the formation of a dense compact of compressed material that acts as a piston driving further compression inside the tube. The tube geometry serves to minimize the role of tensile strength of the HE and flame propagation down fractures, by maintaining continuous compressive forces on the unreacted bed of explosive without the complexity of divergent flow.

When a deflagration is permitted to propagate in a 2D or fully 3D geometry, it is unknown whether the compressive piston formation will continue to play an important role in DDT. Higher geometries permit divergent flow and the establishment of tensile hoop stress that can form and open fractures that subsequently serve as preferential flow paths for combustion product gases and flame. Fracture provides additional reactive surface for flames to amplify the reaction, but also provides vent paths for pressure relief that might quench the reaction. This is a complex counteractive interplay with outcomes that are currently difficult to predict or simulate. Recently, we have begun to address the role of fracture during dynamic reaction, specifically to determine the effect of pre-loading pressure on post-ignition propagation[8]. One thing is certain: 1D DDT tubes do not permit opening of fractures oriented in the direction of the tube axis and therefore the physical effects of preferential flow are not captured by this testing configuration. We currently do not know if, or how, this possible omission from our understanding of DDT mechanics will affect HE response in higher dimensional (i.e. more realistic) geometries.

We have considered a 2-dimensional geometry with the MCCO (Mechanically Confined Cook Off) test in 1998 [9] and a 2D Hot DDT test in 2011 [10]. The MCCO tests showed that mechanical behavior of the explosive during ignition played a key role in the response. The 2D DDT test observed DDT in heated PBX 9501 over run distances of <32 mm. These experiments showed that DDT was possible with run distances similar to that observed in the 1D tubes. As with 1D tubes, however, the 2D test configurations may have also been influenced by unknown boundary effects on the HE-metal interface. The only way to eliminate these potential testing errors is to use a 3D configuration. The trade-off is that it is considerably more difficult to diagnose the internal features of reaction evolution inside a 3D test. The solution we have taken is to test in 1-, 2- and 3-dimensional configurations and then attempt to piece together a complete story.

Large charges of PBX 9501 have been heated and allowed to cookoff, resulting in DDT. The LSAC (Large-Scale Annular Cookoff) addressed a weapons-relevant scale charge of explosive subjected to an abnormal thermal environment such as a fuel fire [11-14,5]. Though it is believed that DDT occurred during that test, the purpose of the test was to validate a thermal kinetics model that could predict the time and location of ignition, and no attempt was made to predict the level of post-ignition violence.

As far as we are aware, CISME is the first experiment using a canonical 3D spherical geometry in an attempt to directly address the DDT mechanism.

2. Experiment

2.1. Explosives

2.1.1. Consolidated PBX 9501

Spheres were manufactured by uniaxially pressing a 12-inch diameter right-circular cylinder then machining the cylinder down to a sphere. A 0.125-inch diameter hole was drilled to the center of the sphere for the fiber optic igniter (this was the smallest hole that could be drilled consistent with LANL explosive machining safety requirements). Although four sizes of consolidated 9501 were manufactured, in the end only two of these charge sizes were tested (6-inch and 3-inch diameters) because these sizes straddled the go/no-go response threshold and the other tests would have been superfluous. The dimensions and associated masses are listed in Table 2. Final density of the charges was measured using water immersion; the average density for all charges in this machining job was 1.8407 g/cc with a standard deviation of 0.0015 g/cc. For background information on characterizing internal density gradients of uniaxially pressed charges, consult reference [15].

2.1.2. PBX 9501 prills

The PBX 9501 prills used in these experiments originate from Holstein lot BAE08H145-015. For the prills and HMX powder charges, the final density of the charge is calculated using the measured mass of powder that went into each shot and the known volume of the interior of the sphere, per design. These calculated densities are listed in the shot record (Table 8).

2.1.3. HMX powder

The HMX powder used in these experiments was manufactured by Eurenco on 3/25/10, lot number 20143217, Grade B, Class 1, and met the MIL-DTL-45444C standard[16]. Grade B signifies that it is 98% pure; Class 1 designates particle size. Class 1 is the coarsest designation established in the standard. Note that PBX 9501 is comprised of a dry blend of Class 1 (coarse) and Class 2 (fine) HMX in a 3:1 weight ratio. Although the MIL standard designates particle size through sieves, more accurate data characterizing the particle size distribution is available from Skidmore, et. al[17]. They report a particle size of 234 μm for the peak of the distribution of the Class 1 HMX.

2.2. Design

Please refer to the first CISME report[1] for complete original design details. Dimensions and explosive properties for the eight tests reported here are summarized in Table 2.

Table 2. Design details for the eight tests.

Test Number	Explosive	Heated?	Charge Diameter	Internal Diameter of Confinement	Charge Mass	Charge Density	Density as %TMD[18]
1	HMX powder	NO	3 inch	3.005 inch	240.3 g	1.0321 g/cc	54.3%
2	HMX powder	NO	1.5 inch	1.505 inch	28.3 g	0.9676 g/cc	50.9%
3	PBX 9501 prills	NO	10 inch	10.005 inch	8,053 g	0.9371 g/cc	50.5%
4	PBX 9501 prills	NO	6 inch	6.005 inch	1,849 g	0.9952 g/cc	53.7%
5	PBX 9501 prills	NO	3 inch	3.005 inch	226 g	0.9707 g/cc	52.3%
6	PBX 9501 prills	NO	1.5 inch	1.505 inch	28.9 g	0.9881 g/cc	53.3%
7	PBX 9501	YES	6 inch	6.199 inch	3,393 g	1.841 g/cc	99.3%
8	PBX 9501	YES	3 inch	3.102 inch	422 g	1.841 g/cc	99.3%

All tests in this series used 4 mm thick 304 stainless steel hemispherical shells for confinement (same as original tests). All charges are centrally ignited. The through-hole for the hypodermic tubing housing the igniter was changed from square to a 0.083-inch diameter round hole to provide a tighter fit that would clamp and secure the tubing

without requiring epoxy potting in the flange, better accommodating assembly and disassembly (Figure 2). The charge assembly is supported in a polycarbonate frame which also serves as fixturing for PDV probes (Figure 3).

Table 3. Photographs of the fiber optic feedthrough on the shells and the polycarbonate fixturing frame.

Figure 2. Photograph from Test 8 partway through assembly. Note the feedthrough groove, the diametral clearance for thermal expansion, the vent grooves in the flange, and the routing of thermocouple wires out of one of the grooves.

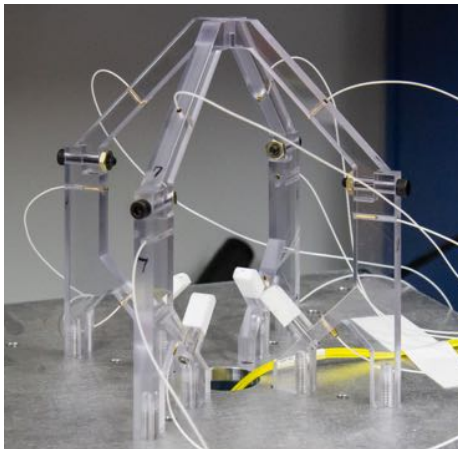

Figure 3. Polycarbonate frame used to support shot. Depicted here is the heated 3 inch version. Note the white ceramic (heat-resistant) supports at the bottom. PDV probe locations are also visible.

None of the design changes are deemed to alter the amount of "dynamic" confinement available that would be relevant for a transition to detonation, as compared to the original design. The mass, thickness of the shells, and number and type of bolts is unchanged from the original design, and any gas path through newly introduced holes in the flange or the fill hole at the top of the sphere will experience choked flow at the reaction rates necessary for DDT. The quasi-static confinement strength can be characterized using the bolt information provided in Table 4.

Table 4. Rated failure strength of confinement for different diameters. Note this is a minimum failure strength rating; actual failure strength is likely to be much higher, even in quasi-static conditions. Dynamic failure will be considerably higher still, as a result of the strain-rate strength dependence of the steel.

Charge Diameter	Bolt Size	Number of Bolts	Bolt tensile rating (psi)	Total rated tensile strength of bolted flange (pounds)
1.5in	#10-24	12	150000	29754
3in	1/4-20	18	150000	81837
6in	1/4-20	24	150000	109116
10in	1/4-20	24	150000	109116

2.2.1. Two different versions of the igniter were used for these FY19 experiments.

The igniter design used in the original CISME experiments was modified in order to survive 200˚C and to accommodate thermocouples for measuring the central temperature. A diagram of the two igniter configurations is shown in Table 5. The same optical fiber was used as previously: Thorlabs® model FT400EMT; 400±8 μm diameter core, 425±10 μm cladding diameter, 1040±30 μm Tefzel™ coating outer diameter[19]. Although the fiber is rated to a maximum temperature of 135 ˚C, we performed our own heating tests to confirm that the fiber survives to successfully ignite the thermite packet at a temperature of 200˚C. The fiber optic is potted inside hypodermic tubing (McMaster® #8988K27, 304 stainless steel, 0.083-inch OD, 0.049-inch ID) using a low-viscosity high-temperature Duralco® 4461N epoxy. The furcation tubing was stripped off for the final portion of fiber that is potted (the Tefzel™ coating remains. For the heated tests only, two 40 AWG PTFE-insulated type K thermocouples (Omega® part 5TC-TT-K-40-72) were potted inside the tubing alongside the fiber optic. The protruding tip of the optical fiber is mechanically cleaved by hand, approximately flush with the end of the hypodermic tubing.

For the consolidated charge, 100 mg of thermite is poured down the hole and lightly hand tamped with a plastic rod. The hypodermic tubing subassembly is inserted to the bottom of the hole, with the tip of the optical fiber touching the thermite. The subassembly is potted by injecting Duralco® 4461N epoxy using a long hypodermic needle affixed to a syringe until the hole is filled (the syringe permits the hole to be filled from the bottom up to avoid any air bubbles).

For the HMX powder and PBX 9501 prill experiments, a packet of thermite must be pre-affixed to the hypodermic tubing assembly, so that the assembly can be pre-inserted into the sphere before the powder or prills are poured through the fill hole. A thin-walled polypropylene 0.2 ml "PCR" sample tube was used as a cup for the thermite (these tubes were used only because they are coincidentally ideal for the purpose). 200 mg of thermite was inserted into cup; this fills the cup to a depth of ≈15 mm from the tip of the cup. The pre-potted hypodermic tubing subassembly was submerged below the surface of the thermite approximately halfway, so that the tip of the igniter is ≈7 mm from the tip of the cup. Duralco® 4461N epoxy was poured into the top of the sample tube, filling the remaining volume and creating a mechanically robust igniter tip (Figure 5)[1].

The thermite used in the experiments is a stoichiometric mixture of aluminum (Al) and iron II,III oxide Fe_3O_4. The aluminum is in powdered form, sourced from Valimet® as their H-5 product. The H-5 aluminum is characterized by Valimet using Microtrac equipment to have a particle distribution as follows: 90% <15 µm, 50% <8 µm, 10% <4 µm. The iron oxide is procured as powder from Alfa Aesar, product 12374-A7. This product is sieved through a No. 325 mesh (by the manufacturer) which yields a maximum particle size of 44 µm. These powders are mixed using a LabRAM™ acoustic mixer in a weight % ratio of 3.22:1 iron oxide to aluminum (this is the stoichiometric ratio). The chemical reaction is:

$$3Fe_3O_4(s)+8Al(s) \xrightarrow{\Delta H=-3.677\frac{kJ}{g}} 9Fe(s) + 4Al_2O_3(s)$$

Note when modeling the heat evolved from this reaction, that 3.298 kJ/g reaction heat is released from solid reactants to liquid products, and the last 0.379 kJ/g is released as the molten reactants solidify.

Table 5. Illustration of igniter configurations.

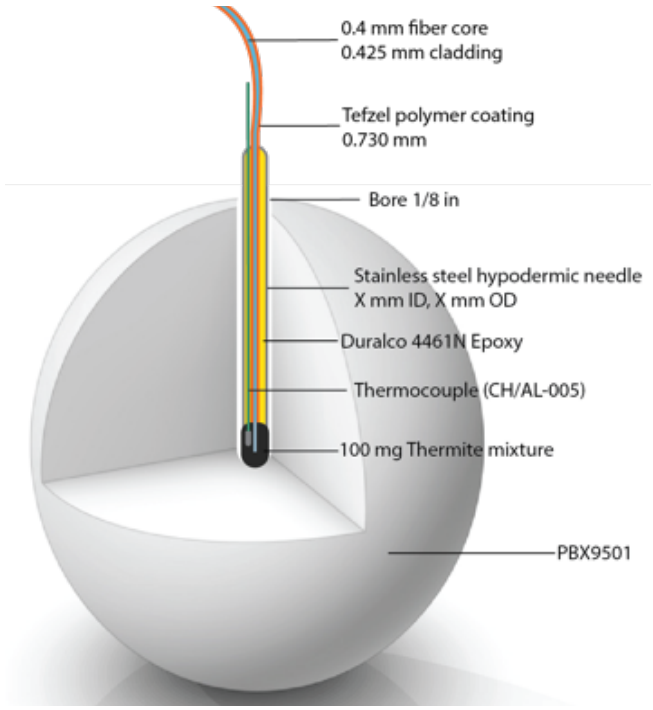

Figure 4. Igniter configuration used for heated, consolidated PBX 9501 tests.

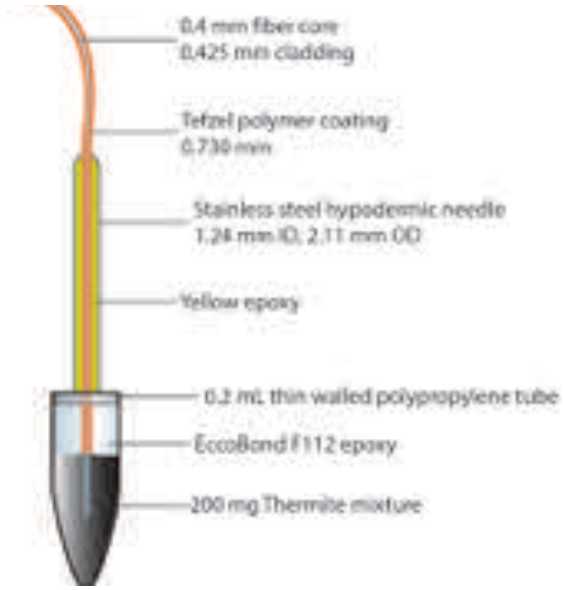

Figure 5. Igniter assembly that was suspended in the cavity of the sphere for the powder and prill experiments.

[1] Our initial igniter tip consisted of a homemade slurry of epoxy and thermite, into which the fiber tip was submerged until the slurry cured. The result was a "PBT" (polymer-bonded thermite) tip. This design did not work well, however. The laser pulse would cleave the tip in two halves—presumably due to a small amount of trapped gas being formed and popping the PBT apart—which then served to mechanically separate the laser pulse from the PBT material. Ultimately, the PBT material would fail to ignite. In retrospect, this behavior is readily explained: the thermite reaction is heavily dependent on particle size, and the exothermic chemistry is only activated when molten aluminum contacts molten iron oxide. Finer particle size and better mixing enhances the ability to ignite the thermite, and to increase the rate of the ensuing reaction. Forming the thermite into a solid PBT serves to inhibit heat transfer and buffer the metal particles. Consequently, we moved to a "cup" geometry that maintains the thermite in a loose powdered form.

2.2.2. Laser Pulse

The laser is an IPG Photonics® model YLR-300/3000-QCW-MM-AC-Y12. The laser operates at 1070 nm and is capable of 300 W continuous or 3000 W at a maximum pulse length of 10ms. The shape and power of the laser pulse are controlled using an analog pulse generator in conjunction with an SRS® DG-535 delay generator. Beam energy is calibrated using a with an Ophir® FPE80BF-DIF-C pyroelectric sensing head connected to an Ophir® StarBrite™ power/energy meter. Additional information on the laser and methods of laser ignition are available in the related Fracture Effects on Explosive Response (FEER) experiment report [20].

Experiments 1 through 7 were ignited with the laser pulse profile illustrated in Figure 6. Experiment 8 was ignited with the laser pulse shown in Figure 7. Values summarizing the pulse characteristics are given in Table 6.

The actual laser power is measured in-situ for each experiment with a power meter internal to the laser. This measurement is made on the beam before it passes down multiple fiber segments and optical couplings. The fiber segments and couplings attenuate the power significantly. Attenuation was measured to be 67% prior to experimentation using a surrogate potted fiber subassembly. That attenuation is taken as the approximate attenuation for all experiments (attenuation for each individual experiment cannot be measured before the fiber assembly is potted into the charge because the high-power of a single laser pulse irrevocably damages the final fiber segment). The final output laser power is subject to the quality of the final optical connection (which is newly made for each experiment) and the transmission/reflection ratio at the cleaved fiber tip. We estimate a 20% uncertainty for laser power, based on variations observed during preliminary characterization of the fiber probes. Data provided in the figures and tables is scaled by the measured attenuation and so represents the best estimate of pulse characteristics delivered to the thermite igniter.

Table 6. Laser pulse characterization.

Test	Nominal Laser Power	Nominal Pulse Duration	Actual Total Pulse Energy Delivered
1-7	217 W	15 ms	1.45 J
8	190 W	50 ms	9.91 J

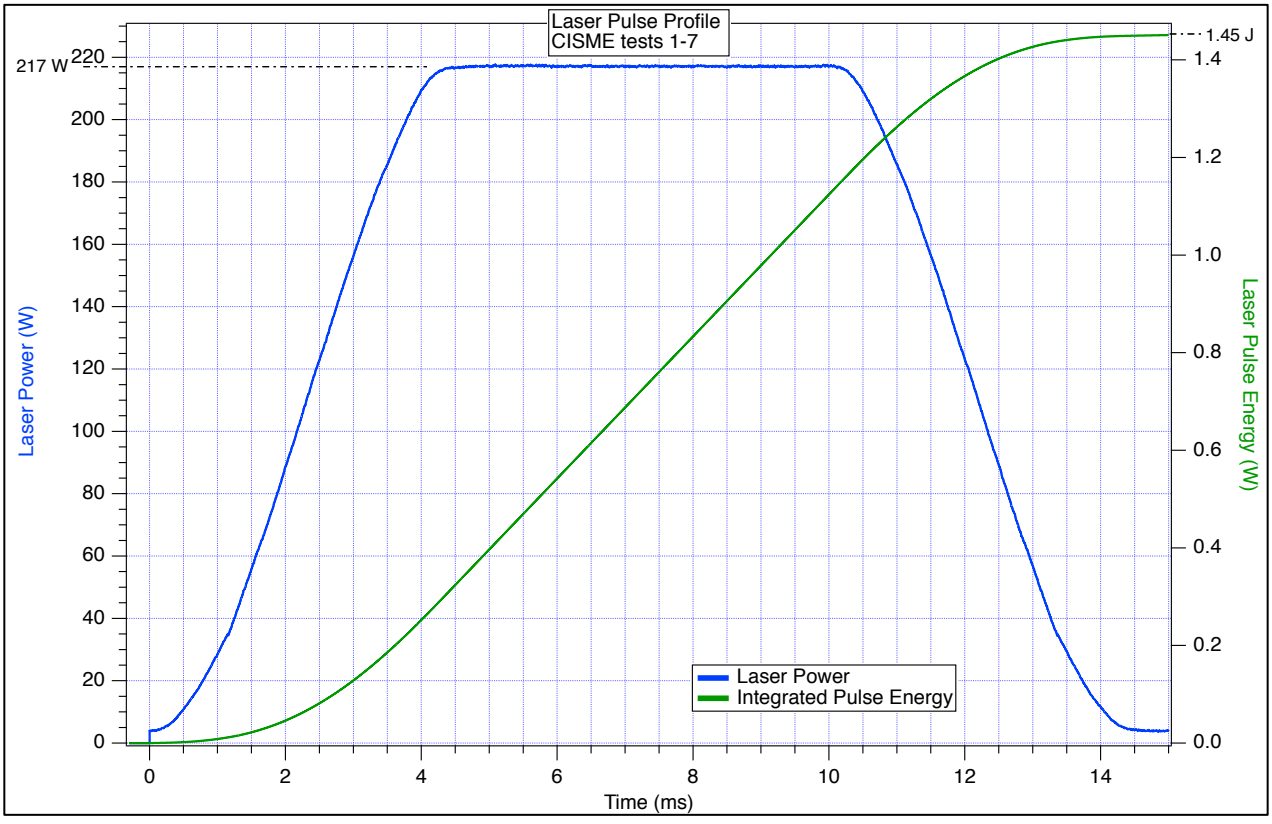

Figure 6. Pulse shape and energy delivered for Tests 1-7. This includes the estimation of attenuation.

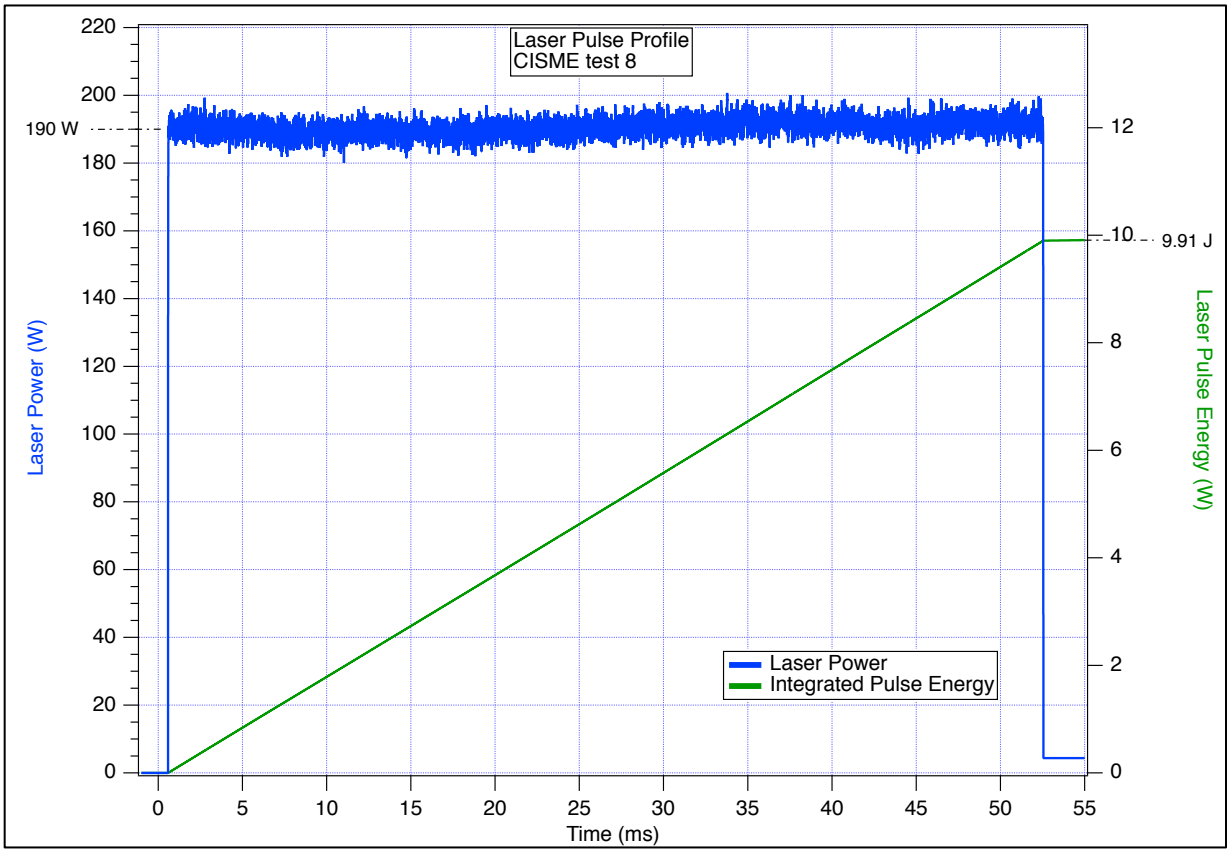

Figure 7. Pulse shape and energy delivered for Test 8, including estimated attenuation. The pulse shape for Test 8 differed from the other tests due to inadvertent changes in the triggering setup made after Test 7.

2.1.1. Experimental Characterization of Ignition Subassembly

Small-scale experiments were performed in the laboratory to characterize the ignition timing of the thermite igniter subassembly.

To characterize the laser-thermite ignitor function times, they were tested under similar conditions in triplicate. High speed videography was used to estimate the average time needed to ignite and fully react the thermite. In each of the trials, the laser was turned on and required a 17.4 ± 12.5 ms dwell time before the thermite began to react. The thermite then required a further 3.3 ± 1.4 ms to fully react. As can be seen there is a substantial amount of variability in the time it takes for the laser to begin to ignite the thermite. Future work is planned to minimize the deviations in the function time of the ignitor.

2.1.2. HMX Powder and 9501 Prills Design Changes

For the powder and prills tests in this series, the same internal diameter of the confinement sphere was used as for the original test series (Table 8). This diameter was sized only slightly larger than the explosive charge diameter, to allow for assembly.

Modification to the shell design was necessary for the prill and powder shots, to permit assembly. A variation was designed with a fill hole at the top, to allow the prills or powder to be poured into the vessel. The cover for the fill hole is “keyed” to the top of the shells to increase strength, but is not gas tight. Table 7 contains figures documenting this design.

Additionally, the slot at the bottom for the hypodermic tubing containing the fiber optic was changed from an oversized square—which required epoxy potting last year—to a half-cylinder precisely matched to the outside diameter of the hypodermic tubing. This allows the hypodermic tubing to be clamped into position using the shells prior to pouring the energetic.

Table 7. Documentation of the fill-hole design used for powdered HMX and PBX 9501 prills experiments.

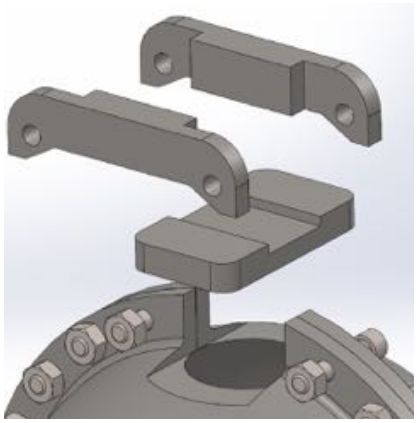

Figure 8. Exploded view of the fill hole design.

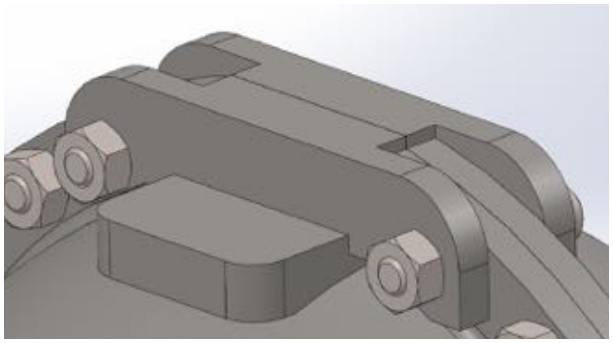

Figure 9. Fill hole design, assembled.

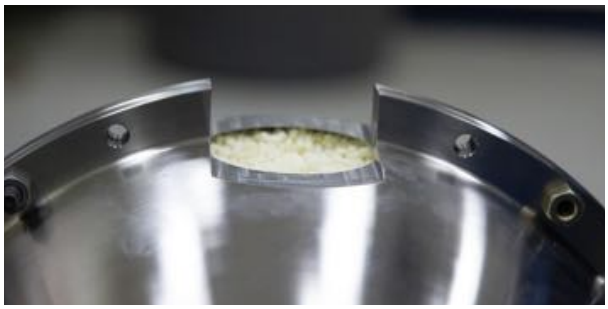

Figure 10. View of Test 3 during assembly. Prills have been poured to the top in the 10-inch diameter sphere.

2.2.3. Heated PBX 9501 Design

For the heated PBX 9501 experiments, the internal diameter of the confinement was increased to accommodate for thermal expansion of the explosive to allow for porosity to develop and for the $\beta \rightarrow \delta$ (beta- to-delta-) phase transition of the HMX. To choose an ullage amount, a model was used to predict the thermal expansion, evolution of porosity, and $\beta \rightarrow \delta$ phase transition of the HMX component. Additional details on the model and the predictions are discussed in section 2.3. The internal diameter of the confinement was chosen to allow for 10% volumetric expansion of the PBX 9501 and are listed in Table 2. Design drawings for the spheres can be found in Appendix A.

Grooves were machined into the mating faces of the bolt flange, which, when bolted together, form vent holes for gas to escape. The purpose of these holes is to permit the gases that are produced during the long period of hot, thermal conditioning to escape. This encourages pyrolysis of binder into volatile products, thereby exacerbating the evolved porosity that is available when the charge is ignited. The grooves are visible in Figure 2.

In both of the heated tests (Test 7 and 8), eight small squares (≈1cm) of high-temperature 3M VHB tape were placed in the sphere, four in each hemispherical shell, at ≈45˚ from the azimuth before inserting the solid PBX 9501 charge. These foam pads acted as spacers to suspend the charge away from the metal wall. The purpose of this was to avoid the initially asymmetric thermal transfer situation in which the charge rests on the bottom of the cavity with all of the diametral clearance air gap at the top. The spacers create a geometry in which there exists a narrow air gap around the entire charge, so that initial heat transfer is purely radiative and convective, until such point as thermal expansion fully compresses the foam pads and the charge comes into conductive contact with the wall of the sphere.

Heating of the spheres was accomplished using fiberglass-insulated Nichrome wire, fastened to the surface of the hemispheres using Kapton (polyimide) tape (Figure 12). A BK Precision® DC power supply (model BK9115) was used for heating. The power supply is capable of maximum 80 V, 60 A, 1200 W. The power supply can be controlled via a USB interface using a Labview® Virtual Instrument (VI) subroutine provided by the manufacturer. Another Labview® VI, custom-designed in-house, implemented a PID control algorithm and used the subroutine USB interface to vary the voltage of the power supply to achieve the desired heating profile.

For the heated experiments, boundary temperatures on the exterior surface of the stainless steel were monitored using thermocouples (Omega® model 5SRTC-TT-K-36-72). Data capture was accomplished through the Labview® heating control software, at a rate of 1 Hz. Thermocouples were electrically insulated and taped to the exterior using polyimide tape, insulated from direct contact with heaters and convective air currents using small squares of foil-backed fiberglass, as shown in Figure 11.

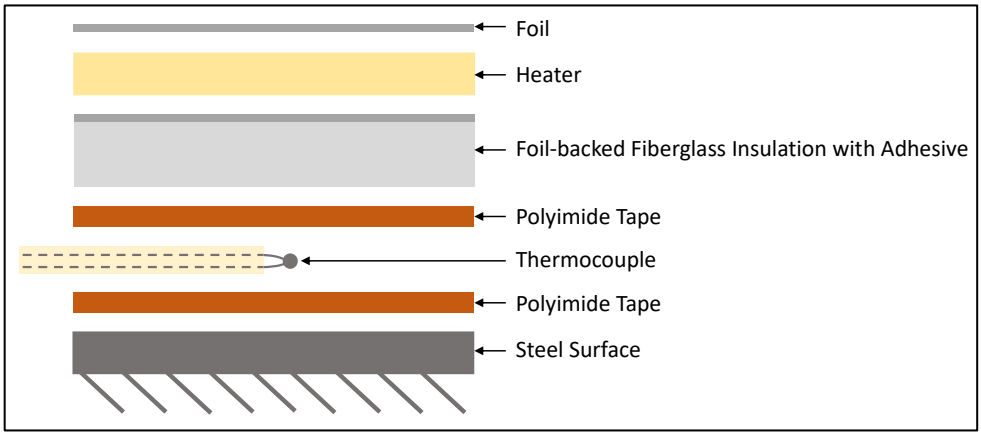

Figure 11. Diagram of how exterior thermocouples are fastened to steel surface (when used).

The assembly is wrapped in aluminum foil (Figure 13) to insulate the shot, radiatively and from convective air currents (preliminary heater tuning tests revealed this level of insulation to be sufficient).

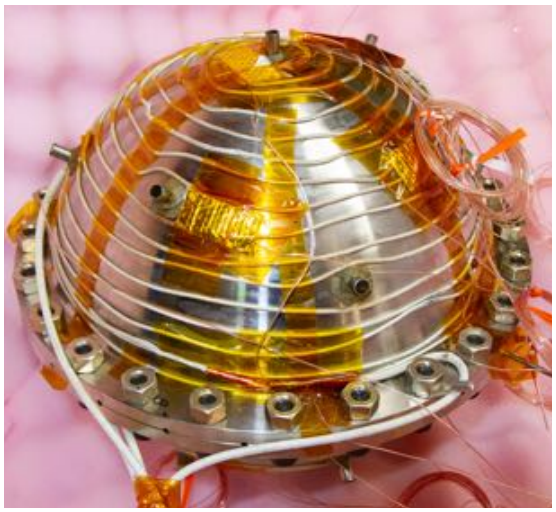

Figure 12. Test 8 partway through assembly. Fiberglass-insulated nichrome heater wire is taped to the surface. Thermocouples are insulated with small pads of foil-covered fiberglass. Hollow tubes are epoxied to surface to provide unobstructed "windows" for the PDV probes after the shot is wrapped in aluminum foil.

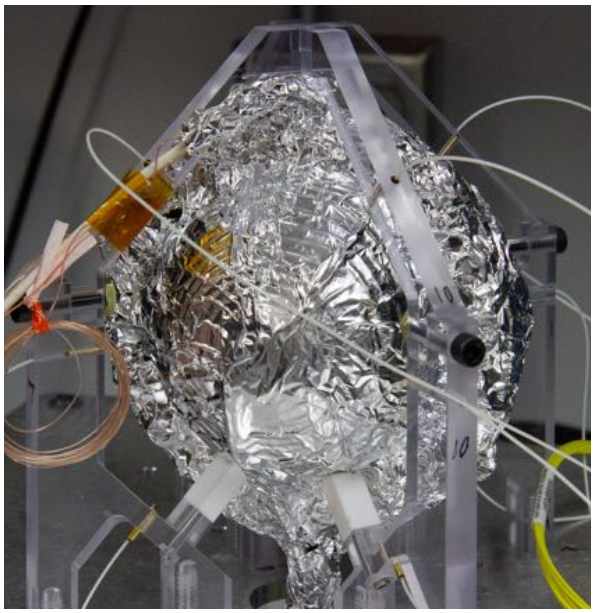

Figure 13. Test 8 wrapped in foil and installed in frame.

2.3. Thermal Profile and Heated HMX Model

In a heated explosive experiment, numerous design aspects must be carefully optimized in order to contrive a conservative, worst-case scenario. In this section we discuss thermochemistry considerations for HMX, details of a kinetics model, details of a porosity and volumetric expansion model, and the resulting design choices motivated by the model predictions.

Thermal damage is a crucial aspect when considering the DDT in plastic bonded explosives. For example, to the best of the authors' knowledge, pristine PBX 9501 has never undergone DDT. The exposure of PBXs to thermal insults results in several chemical and morphological changes to the explosive which increases the likelihood of DDT.

The most obvious consequence of thermal damage is the thermal decomposition of HMX and binders in PBX 9501. This decomposition creates porosity due to two main effects. First, the HMX and binders turn to gas, leaving porosity where the solid material used to be. Secondly, the binder in PBX 9501 softens at higher temperatures which allows the crystals of HMX to mechanically rearrange when exposed to decomposition gas pressure in the newly formed pores. Crystal-binder debonding and microcracking also leads to volumetric expansion and additional porosity.

Another important aspect of thermal damage is the $\beta \rightarrow \delta$ phase change in HMX that occurs in the range of 150-190 ˚C[21]. δ-phase HMX is worse—from a DDT perspective—than β-phase for two reasons: a) delta is more shock sensitive, b) the phase transition to delta phase is accompanied by volumetric expansion, comminution of average particle size from HMX crystallite fracturing and correspondingly increased porosity and surface area[22].

The $\beta \rightarrow \delta$ phase transition does not occur instantaneously, but is characterized by a kinetic process that is a function of temperature and time. The kinetics of the phase transition are an integral part of the Dickson four-step cookoff kinetics model[23-25]. We implement these Dickson four-step kinetics in an FEA simulation.

We iterated simulation runs, altering heating ramp rate, soak temperature, and soak duration, to choose a thermal profile for the CISME heated experiments according to the following considerations:

1. Maximize the fraction of PBX 9501 that undergoes the $\beta \rightarrow \delta$ phase transition, thus striving for a uniform material state at the time of ignition.

2. Avoid inadvertent self-ignition of the PBX 9501 prior to our desired ignition time.

3. Find durations short enough that we can execute the experiment in a reasonable period of time (ideally a single work shift).

The nominal choice of thermal profile was determined to consist of a ramp at ≈4 ˚C/min to a soak temperature of 170 ˚C. The temperature referenced is the boundary temperature on the exterior surface of the sphere. This boundary soak temperature is maintained for a duration of hours. Then the boundary temperature is ramped to 180 ˚C until the temperature at the center of the charge rises to a temperature ≈165 ˚C. The experiment is then centrally ignited with the laser.

The predictions for the conversion of $\beta \rightarrow \delta$ HMX for this chosen thermal ramp are shown for the 3-inch charge in Figure 14 and for the 6-inch charge in Figure 15. The actual measured experimental ramps and thermal profiles used for Test 7 and 8 closely followed this nominal ramp and are shown in section 3.4.

Two competing considerations drove the sizing of the ullage available for expansion of the explosive. For a conservative scenario, it is desirable to convert the maximum possible fraction of HMX from beta to delta phase. To achieve this requires volume for expansion, as it has also been shown that confinement will inhibit the beta-delta phase transition as a function of pressure[26,27]. However, it is also desirable for the explosive to completely fill the available free volume (often termed *ullage*) at the time of ignition in order maximize the mechanical confinement and prevent preferential flow paths for flames between the case and the charge. The available ullage for expansion must therefore be sufficient to allow the phase change, but small enough to ensure the explosive fills the available volume before ignition.

A porosity model was developed by Heatwole and is documented in reference [3]. It is known that PBX 9501 will expand to approximately 15% more than its original volume in a manner which gives rise to a reasonably homogenous porosity[22,28]. The internal diameter of the hemispherical shells was chosen to provide 10% volumetric ullage, which leaves ample room for the $\beta \rightarrow \delta$ phase transition and introduces the porosity necessary to sensitize the explosive to the DDT process while ensuring that the expansion during thermal expansion completely fills the available free space.

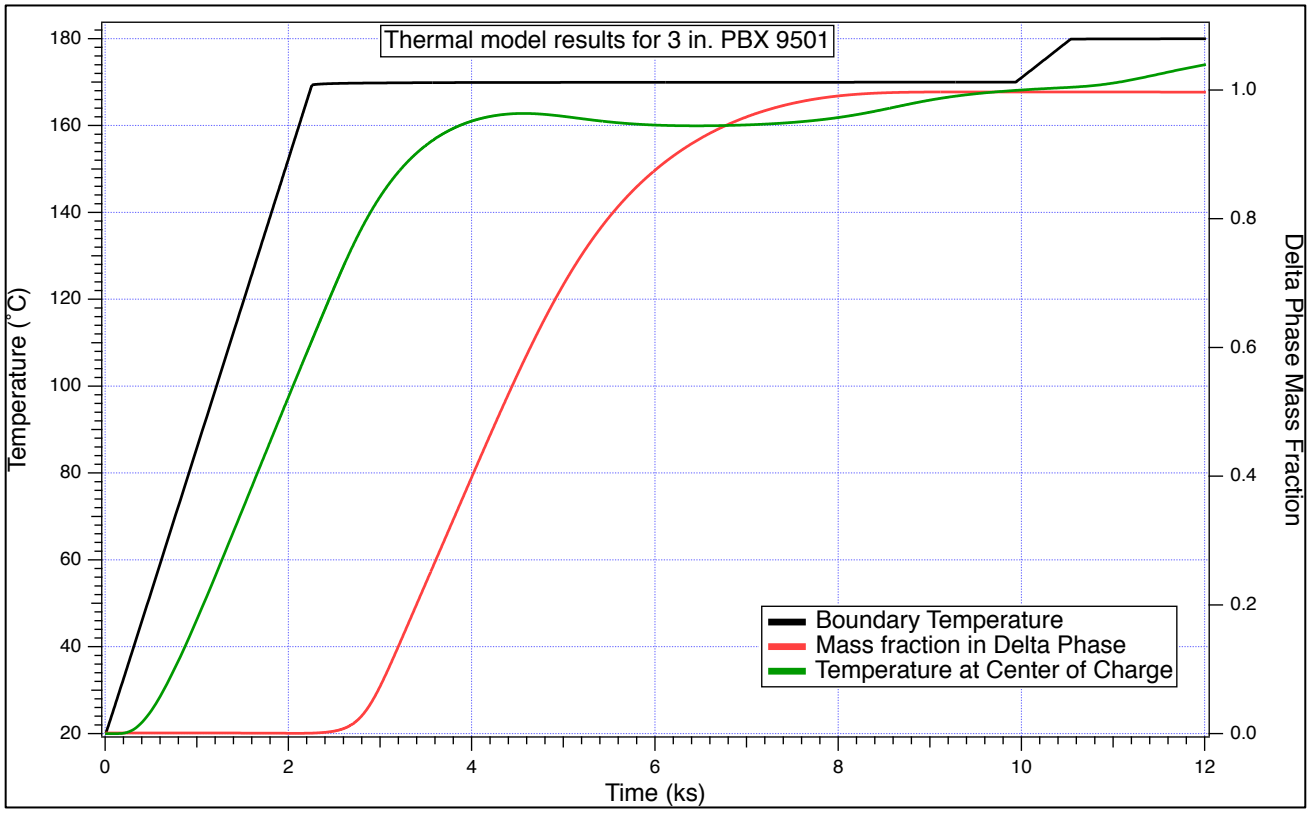

Figure 14. Thermal model results for the 3 inch HMX powder (Test 1) showing predicted mass fraction in delta phase for the chosen thermal profile. The modeling was employed to ensure that the thermal damage state at the time of ignition was conservative; in this case that means ensuring maximum conversion from beta- to delta-phase HMX.

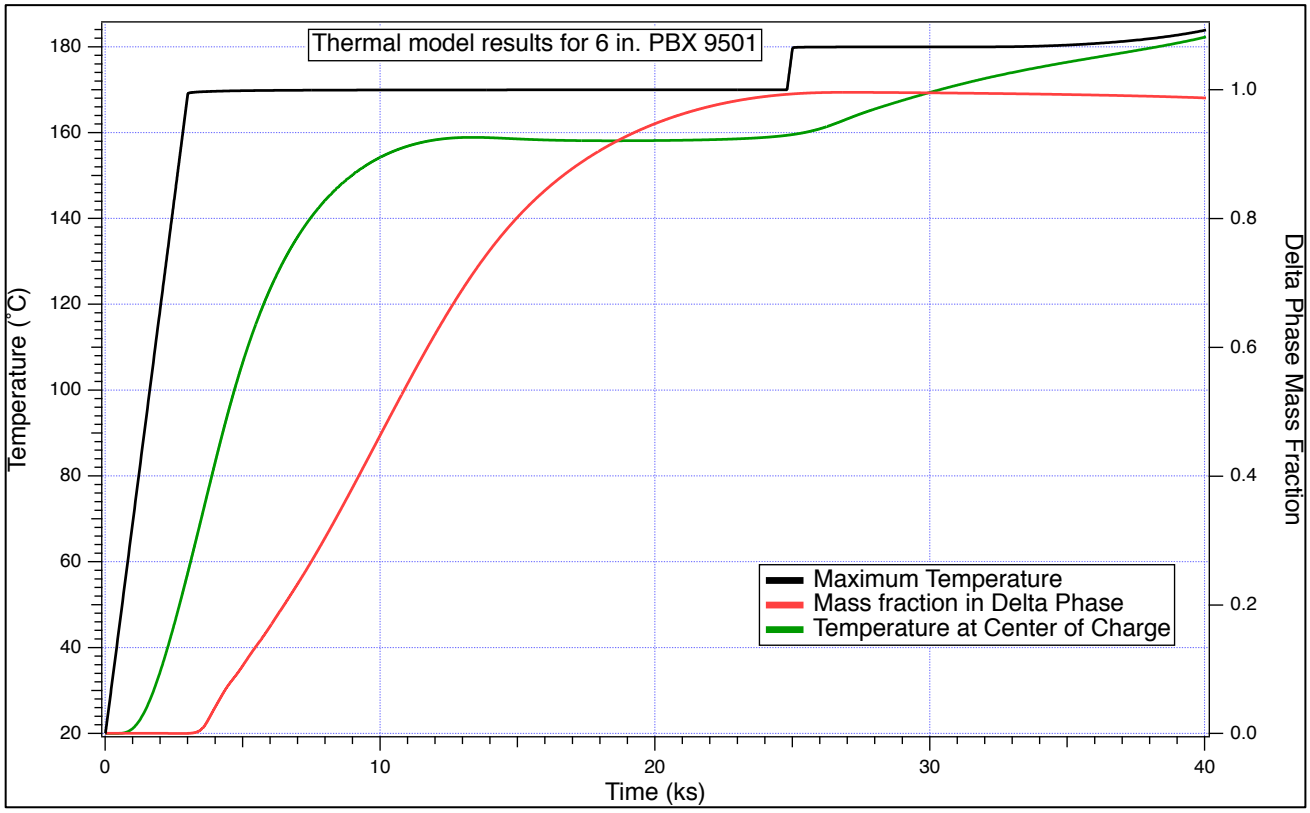

Figure 15. Thermal model results for the 6 inch PBX 9501 (Test 7) showing predicted mass fraction in the delta phase for the chosen thermal profile. The climbing temperature excursion at the end of the run is due to self-heating of the contained explosive charge.

2.4. Diagnostics

2.4.1. Pressure Gauges

Two 50 psi PCB® model 137B25 free-field pencil probe gauges, captured at a sampling rate of 400kS/s for duration 2.5 s were used for measuring the air blast pressure. The gauges were positioned approximately 90˚ apart from each other, at a distance of 30 ft and 25 ft with clear lines of sight to the shot. The gauges are visible in Figure 16 to the left and right sides of the image.

Figure 16. Photograph of site layout, Test 5. Blast gauges are mounted to metal tripod stands on far right ("south") and left ("east") of the image, circled in red. Metal blast shield in foreground serves as protection for the final optical coupler box. The wooden arch and sandbags are intended to catch the larger fragments that might form from the thicker flange portion of the metal shells, in the event of a violent reaction.

2.4.2. Velocimetry

Twelve PDV probes point at the outside surface of the charge, normal to the surface, and provide a diagnostic to quantify the explosiveness and also determine whether detonation occurs. The PDV probes are mounted in a polycarbonate frame; the frame is mounted to the base plate and also forms a mounting cage for the charge (see Figure 3). On the heated shots, small sections of stainless tubing were bonded directly to the surface of the sphere in order to provide an unobstructed window for the PDV probes, that might otherwise be blocked by heating wires or foil insulation (Figure 12). Note that the transit time for sonic waves from the charge to the PDV probe mounting locations, through the assembly, bounds the lowest meaningful velocity that can be measured by the system.

The PDV data are most useful for high case/fragment velocities, as would be the case of a detonation or HEVR, as the total record duration is only ~1 ms. Furthermore, the probes are positioned approximately 20 mm away from the charge surface and are destroyed when impacted by the charge.

2.4.3. High-speed Video

High-speed videography provides a redundant diagnostic for detonation, and also provides information on sub-detonative response. Two video cameras were used: a Phantom® V2512 camera with a pixel resolution of 384 px width by 288 px height at a frame rate of 150,000 fps with a 5.9 s duration, and a Shimadzu® HPV-X2 with a pixel resolution of 400 px width by 250 px height at a frame rate of 1,000,000 fps with 256 frames of buffer (total duration 10^{-4} s). The camera locations and view are shown in Figure 17.

Figure 17. Photograph from a viewpoint behind the shot for Test 5, looking back at the turning mirrors located above the portholes in the bunker. The Phantom camera observes through the porthole on the left of the image; the Shimadzu through the right. Also visible is the turning mirror situated directly above the shot, which provides a top-down view of the shot.

2.5. Triggering

The Phantom video record has sufficient buffer to be triggered from the firing signal, allowing it to be independent of the post-ignition response for reliable data capture. Generally, the 2.4 s duration record length for the pressure gauges would also be sufficient. On Tests 1 and 2, the pressure gauges were triggered with the laser, and captured data. However, on Tests 3 and 4 the arrival of the blast was so long after the laser trigger (~3-5 seconds) that the pressure record failed to capture the blast. To remedy this, the pressure data capture configuration was altered to be triggered by the piezoelectric contact pin for Tests 5-8.

The PDV and the Shimadzu have too short a buffer to capture the full duration of a slower sub-detonative deflagration event. A piezoelectric contact pin was used for triggering these two diagnostics at an appropriate time to provide a short window of data collection. The piezo pin was mounted on the mid-plane at a distance of 3 mm from the outside surface of the metal shell. The Shimadzu and PDV thus capture a short buffer which is approximately centered on the moment when the charge has traversed the 3 mm gap to impact the piezo pin.

All Phantom video timestamps are relative to the laser trigger. All Shimadzu video and PDV timestamps are relative to the piezo pin impact trigger. The interval between these triggers was captured on the oscilloscope unless the interval exceeded the record length. When the interval exceeded the record length, the time that light is first observed in the Phantom video can be used to approximate the interval between the triggers. These intervals are included in Table 8.

3. Results

Table 8. Summarized test conditions.

Test Number	Explosive	Charge Diameter	Heated?	Interval between laser trigger and piezo pin trigger (s)	Time of first reaction light on Phantom video (after laser trigger) (s)
1	HMX powder	3 inch	NO	>0.8s	0.909
2	HMX powder	1.5 inch	NO	0.27761	0.278
3	PBX 9501 prills	10 inch	NO	>0.8s	4.537
4	PBX 9501 prills	6 inch	NO	>0.8s	3.727
5	PBX 9501 prills	3 inch	NO	2.3726	2.372
6	PBX 9501 prills	1.5 inch	NO	3.5757	3.576
7	Solid PBX 9501	6 inch	YES	0.039865	0.040
8	Solid PBX 9501	3 inch	YES	Not recorded	0.078

3.1. High-speed video

In video records, observation of multiple independent sources of light breaking out of the surface of the charge provides evidence of case fragmentation. Significant case fragmentation is evidence for detonation: typically hydrodynamic yielding of the steel occurs only when subjected to shock pressures generated by detonations. The times at which first light is visible on the Phantom video record are tabulated in Table 8; this value quantifies the duration of the deflagration process.

In the following sequences, the Phantom video timestamps are relative to the laser trigger, while the Shimadzu timestamps are relative to the piezo pin impact trigger. The interval between these triggers was captured on the oscilloscope unless the interval exceeded the record length. When the interval exceeded the record length, the time that light is first observed in the Phantom video can be used to approximate the interval between the triggers. These intervals are included in Table 8. All images depict a “straight-on” view at the bottom, and a top-down view through a turning mirror at the top of the frame (see Figure 43 for clarification on the arrangement).

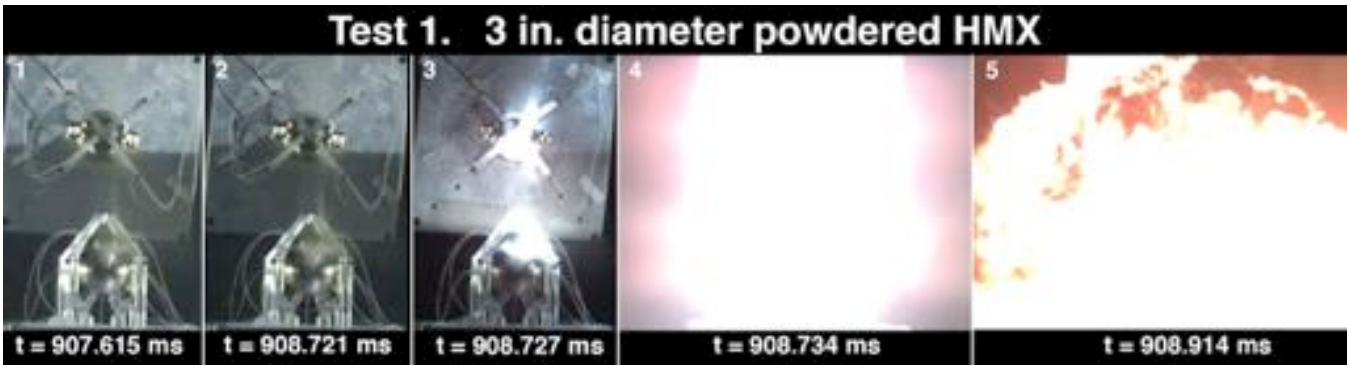

Figure 18. Test 1, Phantom video. 3 inch powdered HMX. Frame 1 and 2 show smoke escaping from between the shells. Frame three is the first frame with light. Frame 4 is the next captured image, ≈6 µs later. Frame 5 shows the late-time fireball.

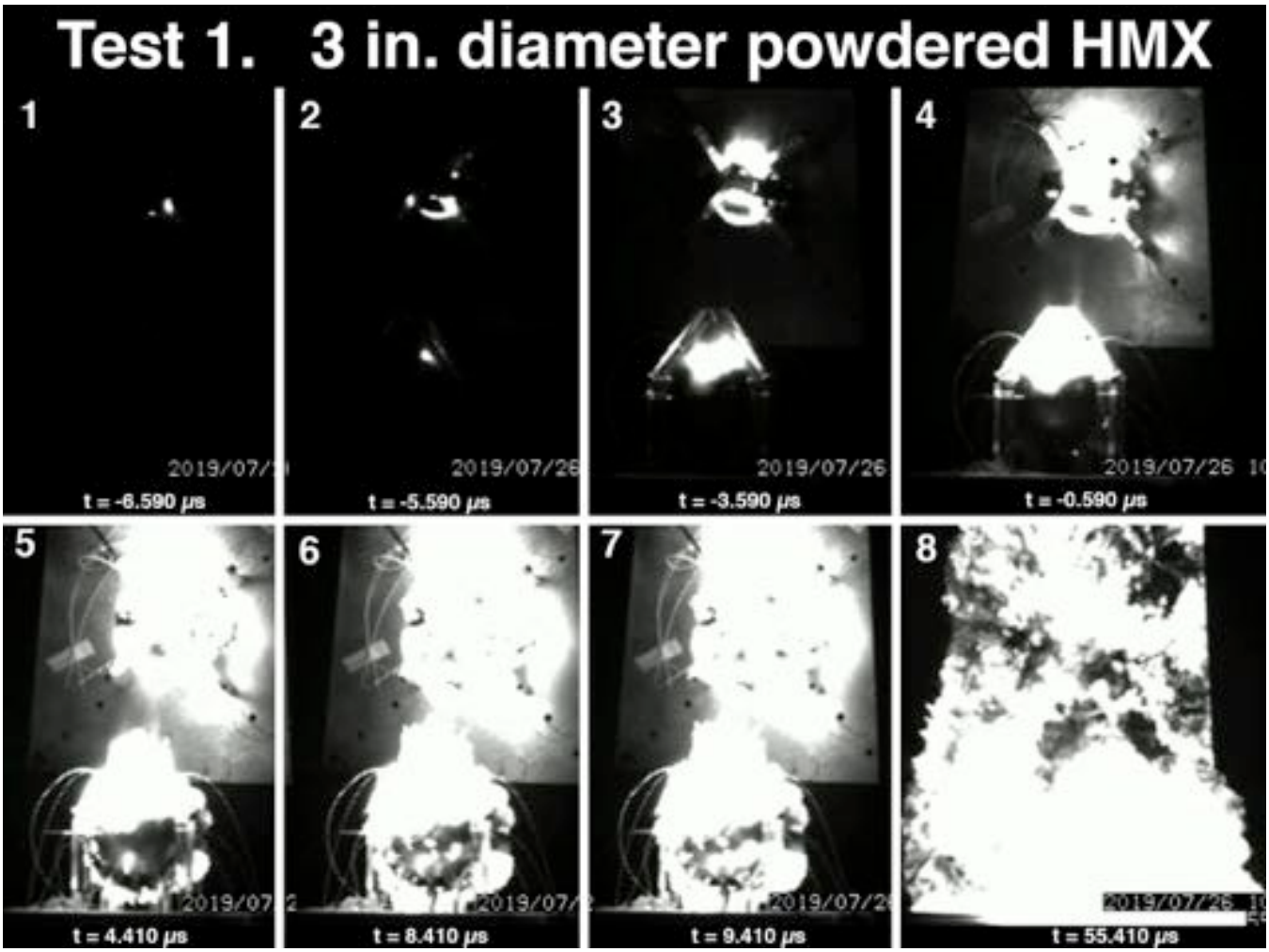

Figure 19. Test 1, Shimadzu video. 3 inch powdered HMX.

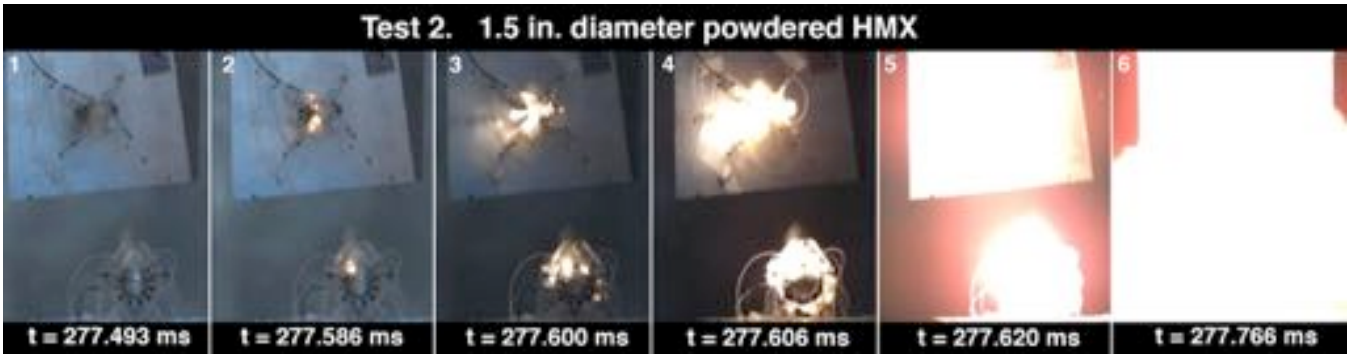

Figure 20. Test 2, Phantom video. 1.5 inch powdered HMX.

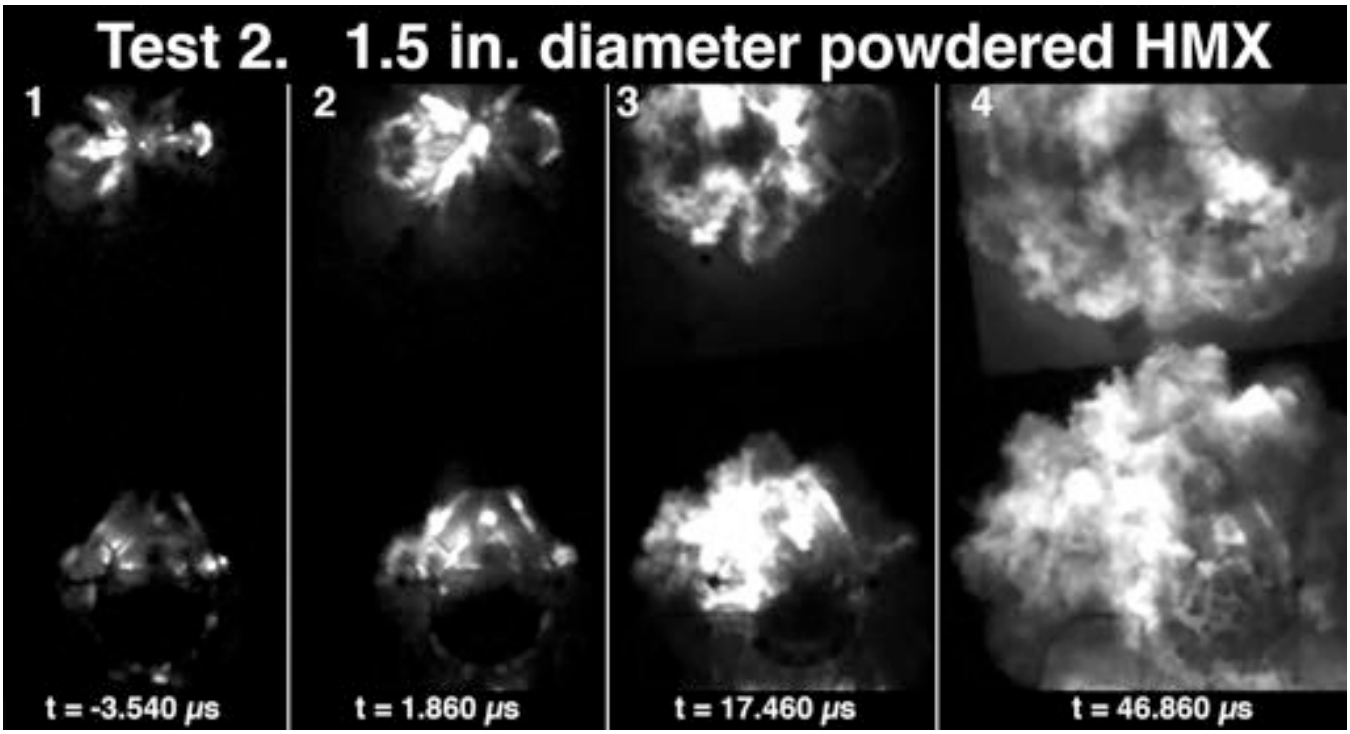

Figure 21. Test 2, Shimadzu video. 1.5 inch diameter powdered HMX. Fragmentation of the case is evident in frame 4.

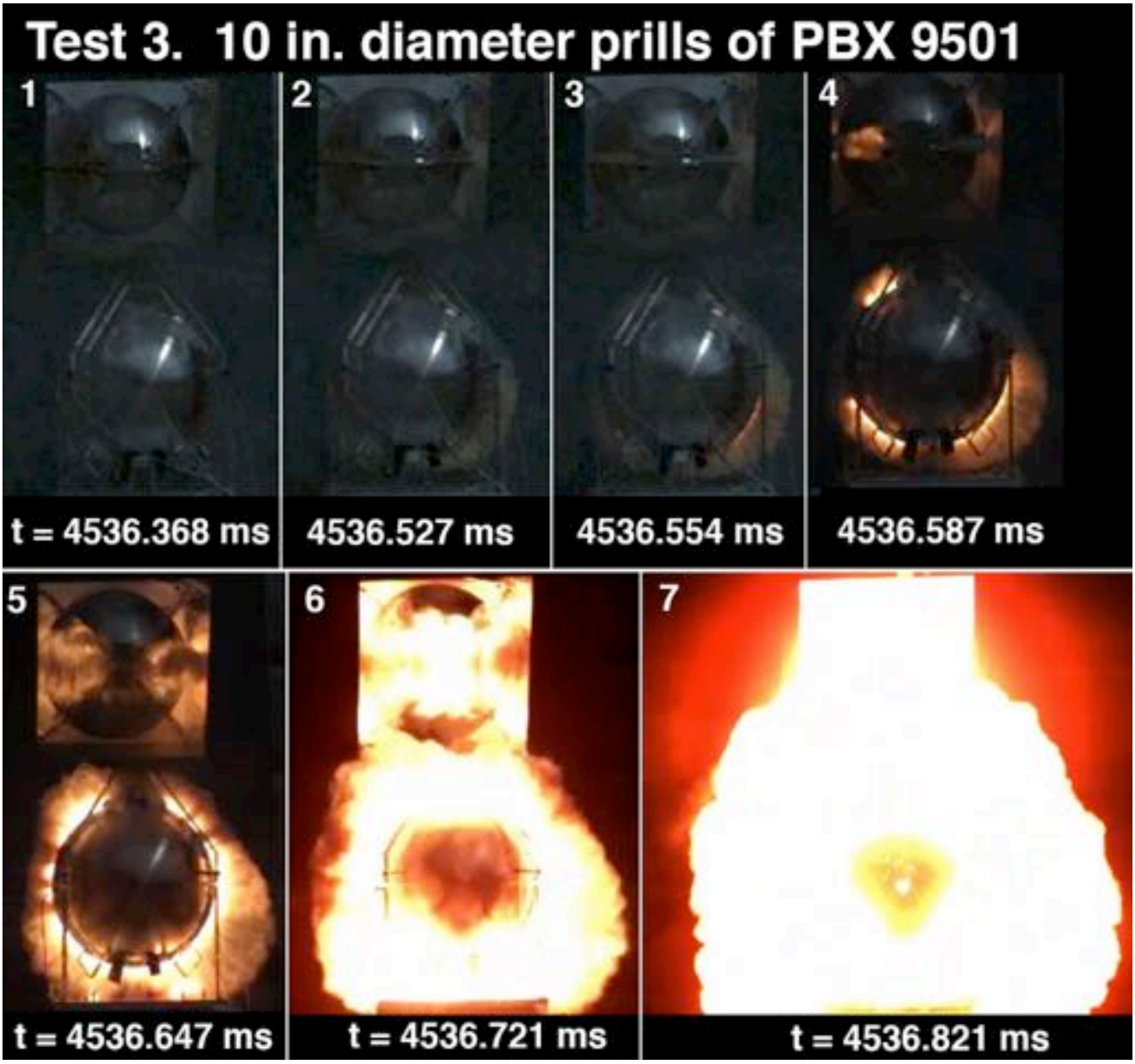

Figure 22. Test 3, Phantom video. 10-inch diameter PBX 9501 prills.

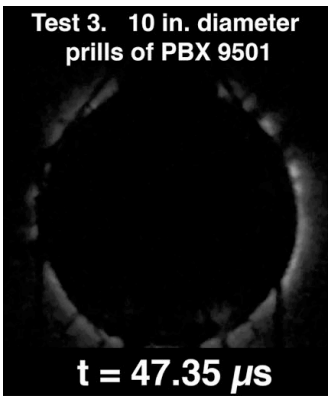

Figure 23. Test 3, Shimadzu video. 10-inch diameter PBX 9501 prills. This was the final frame captured on the Shimadzu; reaction is just becoming visible.

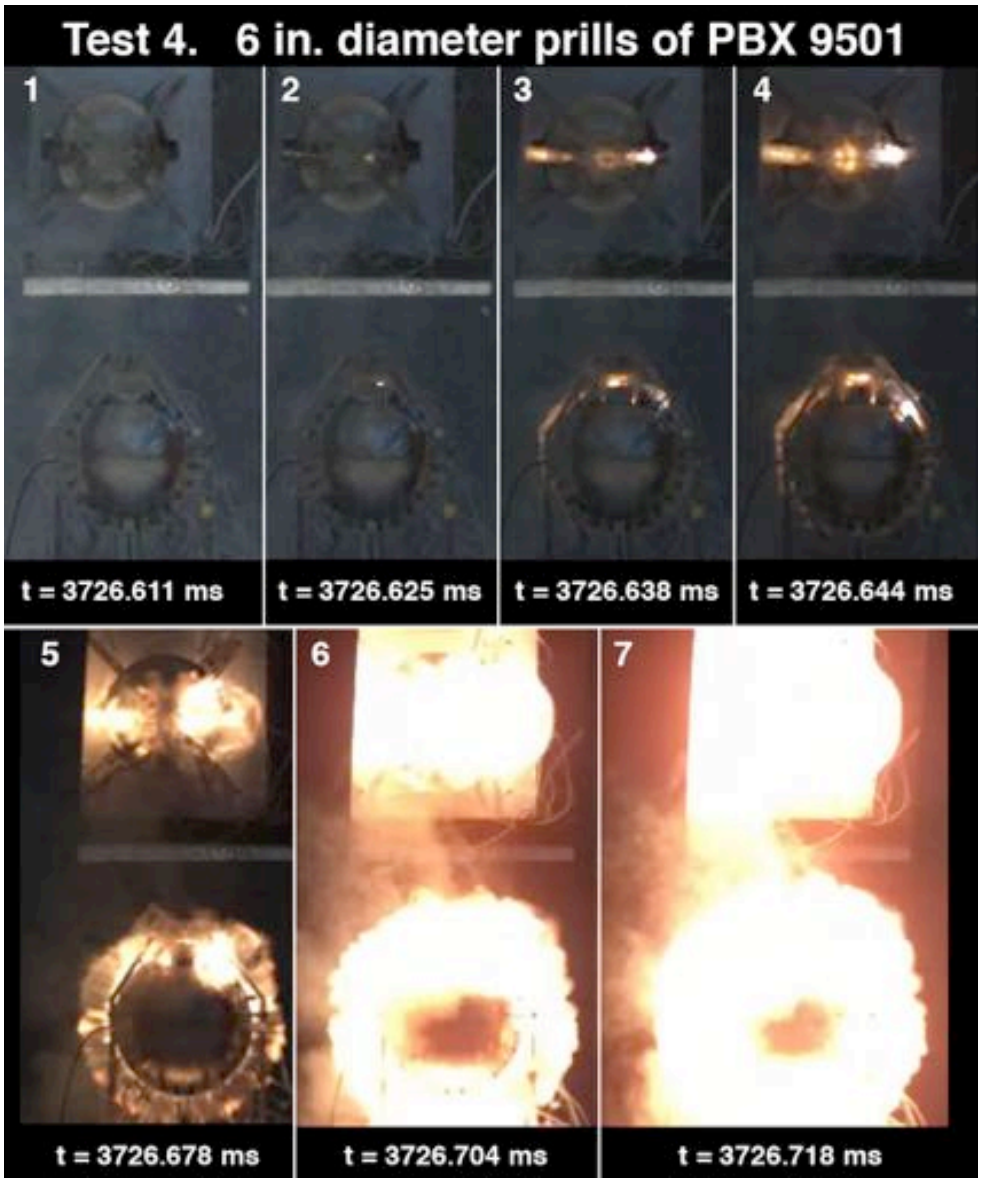

Figure 24. Test 4, Phantom video. 6-inch diameter PBX 9501 prills.

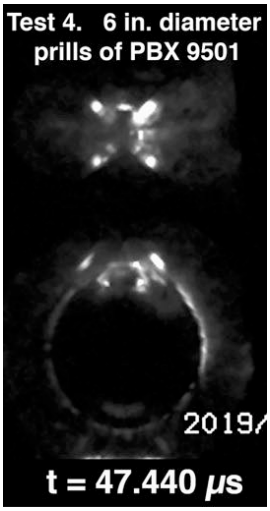

Figure 25. Test 4, Shimadzu video. 6-inch diameter PBX 9501 prills. This was the final frame captured; reaction is just becoming visible.

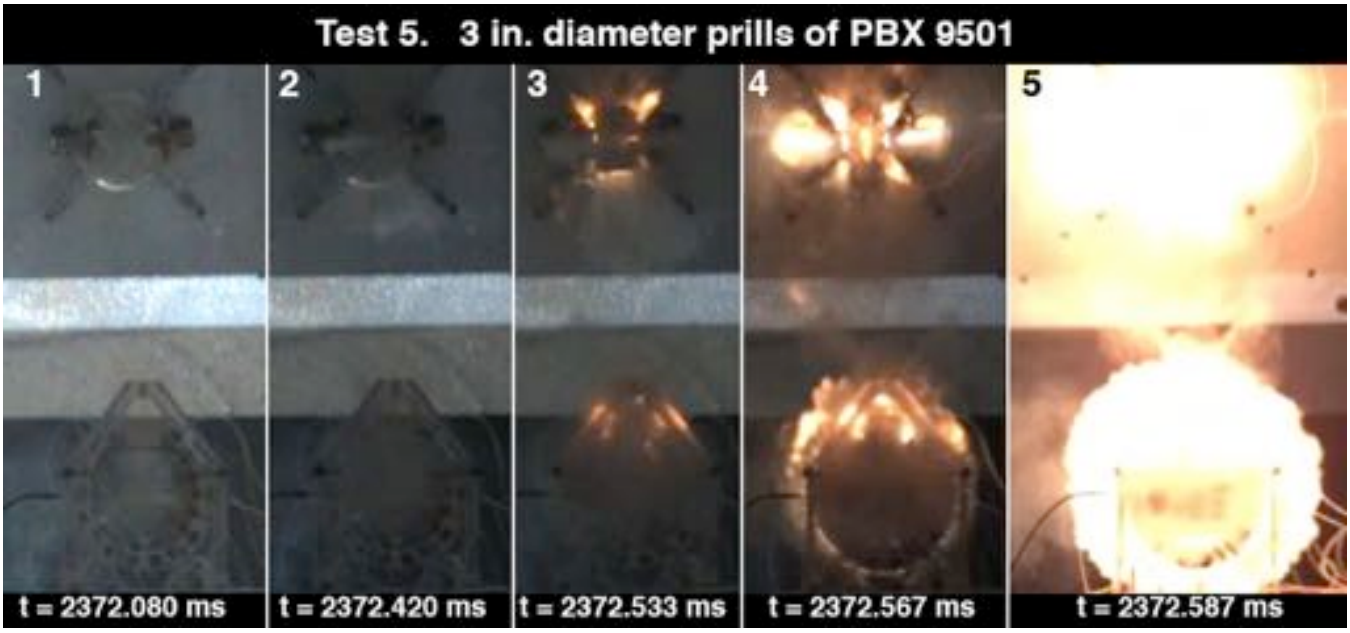

Figure 26. Test 5, Phantom video. 3-inch diameter PBX 9501 prills.

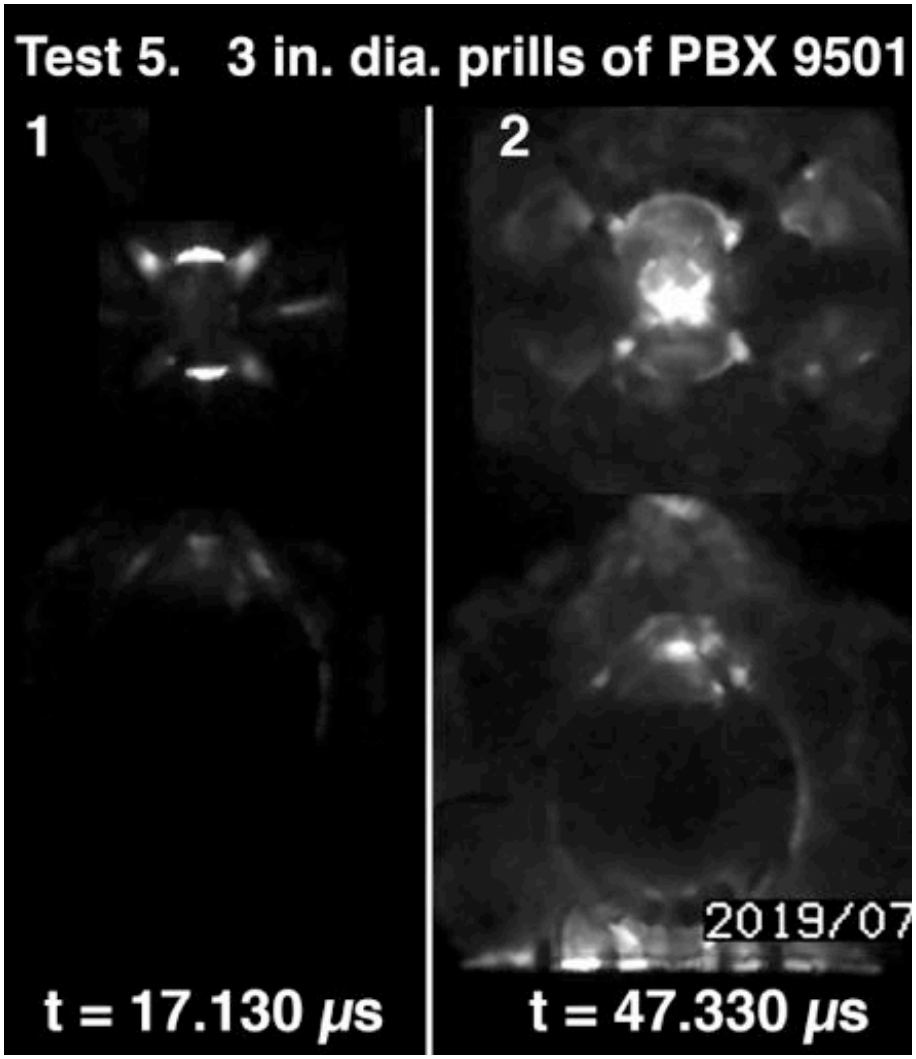

Figure 27. Test 5, Shimadzu video. 3-inch diameter PBX 9501 prills.

Figure 28. Test 6, Phantom video. 1.5-inch diameter PBX 9501 prills. In frames 7 and 8 a mostly intact hemisphere is visible.

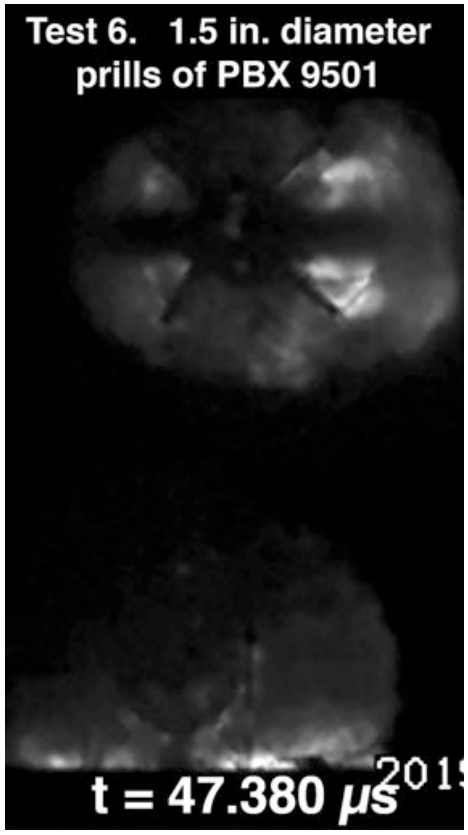

Figure 29. Test 6, Shimadzu video. 1.5-inch diameter PBX 9501 prills. This was the final frame captured.

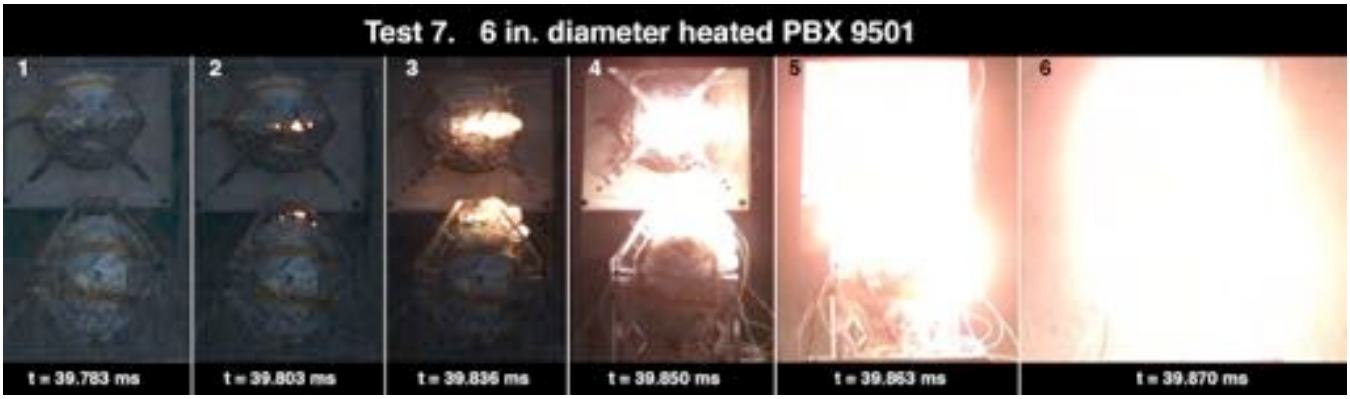

Figure 30. Test 7, Phantom video. 6-inch diameter heated PBX 9501. First sign of reaction is flames escaping the seam at the top.

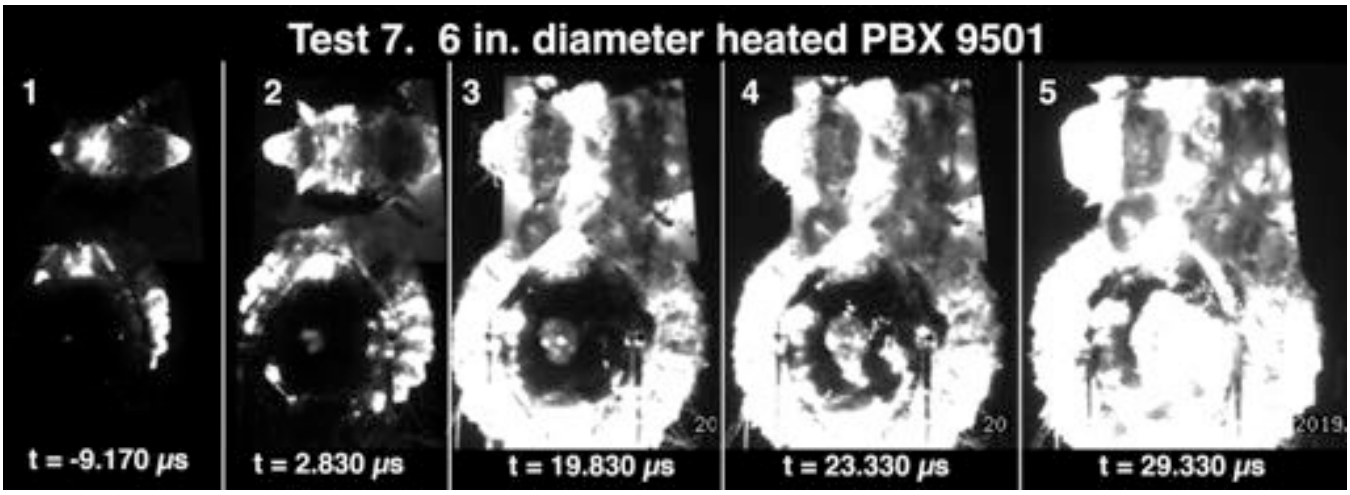

Figure 31. Test 7, Shimadzu video. 6-inch diameter heated PBX 9501. Breakout of reaction is visible at numerous independent points in frames 3 and 4.

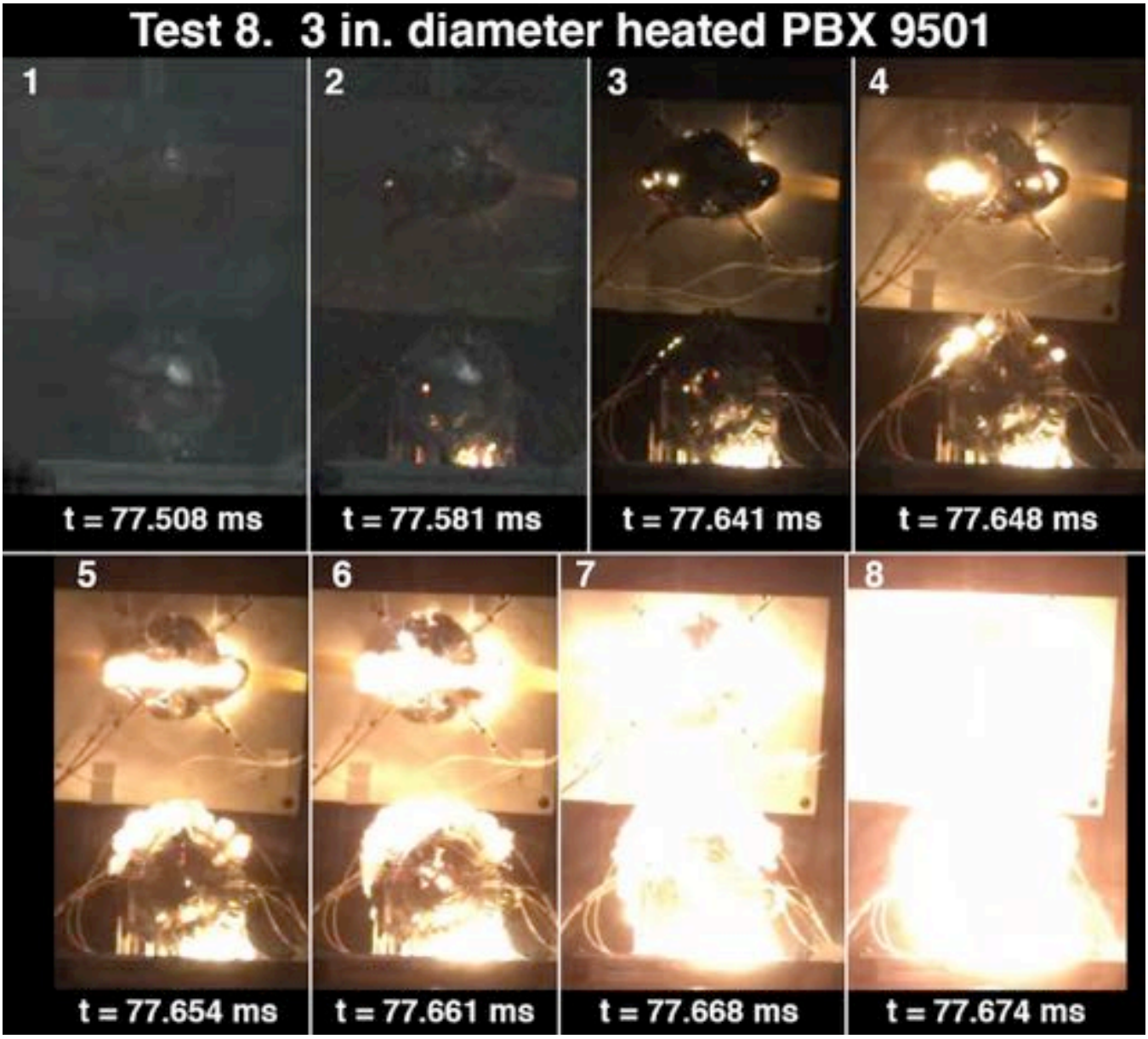

Figure 32. Test 8, Phantom video. 3-inch diameter heated PBX 9501. Frames 4, 5, and 6 show light emitted from multiple independent locations.

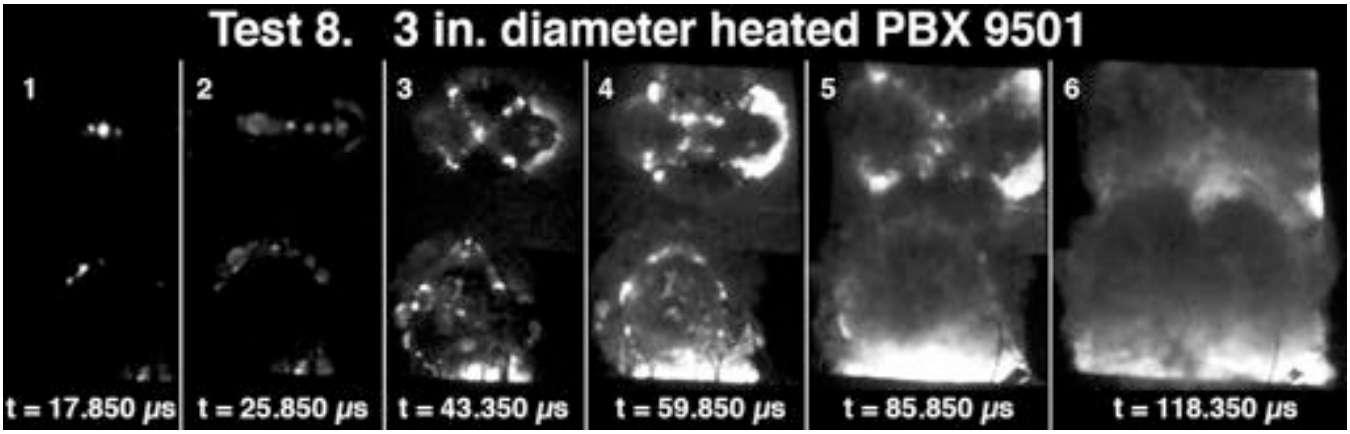

Figure 33. Test 8, Shimadzu video. 3-inch diameter heated PBX 9501. Fragmentation of the case is evident in frame 4.

3.2. Blast Pressure

Attributes of the measured blast pressure can be compared the known shape of an ideal blast pulse that would be expected in the case of a full detonation of a bare charge. Recorded blast pressure traces are shown in Table 10. The peak blast pressure and arrival time that would be anticipated for detonation of each test was calculated using the method outlined in Kinney & Graham[29] and is documented alongside the measured value in Table 9[2]. The following fixed parameters were used in the calculations: ambient pressure 11.6 psi, ambient temp 85˚F, height-of-burst 1.25 ft, reflection factor 2.00, weight and density from Table 2.

Of the blast wave characteristics that might diagnose reaction violence, the peak blast pressure is the most useful. Physically, the peak pressure is a stronger function of detonated explosive mass than is the arrival time. More importantly, in our experiment the arrival time of the measured shock is a summation of the transit time of the shock through the air with the duration of the sub-detonative deflagration that occurs before the air shock is produced. If the measured delay is close to the expected delay, it indicates that DDT occurred promptly after ignition. For tests in which the delay between laser ignition and impact of the piezo pin was not captured on the oscilloscope (due to the extremely long delay), the arrival time of the blast provides a useful measure of the deflagration duration to corroborate the Phantom video record. Note that the pressure data for heated shots (Test 7 and 8) is less useful because the shot was surrounded with physical barriers to mitigate fragments that might start a brush fire, which distort and attenuate the air blast in complicated ways.

Peak pressure is most usefully employed to estimate the percentage of the original explosive mass that ultimately participates in the reaction. Whether the reaction is a detonation or a very rapid deflagration, if the quantity of explosive consumed is the same, the resultant air blast will be very similar.

Table 9. Comparison between measured and anticipated peak blast pressure and delays for each shot. On Tests 7 and 8 (heated tests), additional fragment mitigation was added, which also mitigated the blast characteristics.

Charge Configuration	Sensor ID	Measured peak blast pressure (psi)	Anticipated peak blast pressure for full reaction (psi)	ratio PEAK PRESSURE Measured/ Expected	Measured blast delay (from onset of violent reaction) (ms)	Anticipated blast delay (ms)	BLAST DELAY measured/ expected
3 inch powdered HMX	Test 1 South	1.18	1.49	79%	17	15.99	106%
	Test 1 East	0.97	1.16	83%	21	20.15	104%
1.5 inch powdered HMX	Test 2 South	0.46	0.62	74%	19.39	18.62	104%
	Test 2 East	0.43	0.51	85%	24.39	22.9	107%
10 inch prills	Test 3 South	no data	13.88	no data	no data	8.49	no data
	Test 3 East	no data	9.19	no data	no data	11.7	no data
6 inch prills	Test 4 South	no data	4.76	no data	no data	11.95	no data
	Test 4 East	no data	3.35	no data	no data	15.79	no data
3 inch prills	Test 5 South	0.93	1.45	64%	20.1	16.07	125%
	Test 5 East	0.81	1.14	71%	24.4	20.24	121%
1.5 inch prills	Test 6 South	0.26	0.62	42%	22	18.6	118%
	Test 6 East	0.24	0.51	48%	26.9	22.88	118%
6 inch heated 9501	Test 7 South	3.95	6.90	57%	15.845	10.82	146%
	Test 7 East	4.14	4.77	87%	19.57	14.48	135%
3 inch heated 9501	Test 8 South	1.14	1.93	59%	20.802	15.2	137%
	Test 8 East	0.64	1.47	44%	26.572	19.32	138%

[2] The blast pressure calculations are done using a spreadsheet written by Philip Rae (LANL M-6) which implements the Kinney & Graham method. We thank him for this useful tool.

Table 10. Blast pressure traces for Tests 1, 2, 5-7. Note the early signals evident prior to the shock on tests 1, 2, and 5. Pressure data was missed on Tests 3 and 4, as the blast arrived too late (triggering was modified for subsequent tests). Times on the horizontal axis have been adjusted to be uniformly referenced (the laser pulse occurs at t=0).

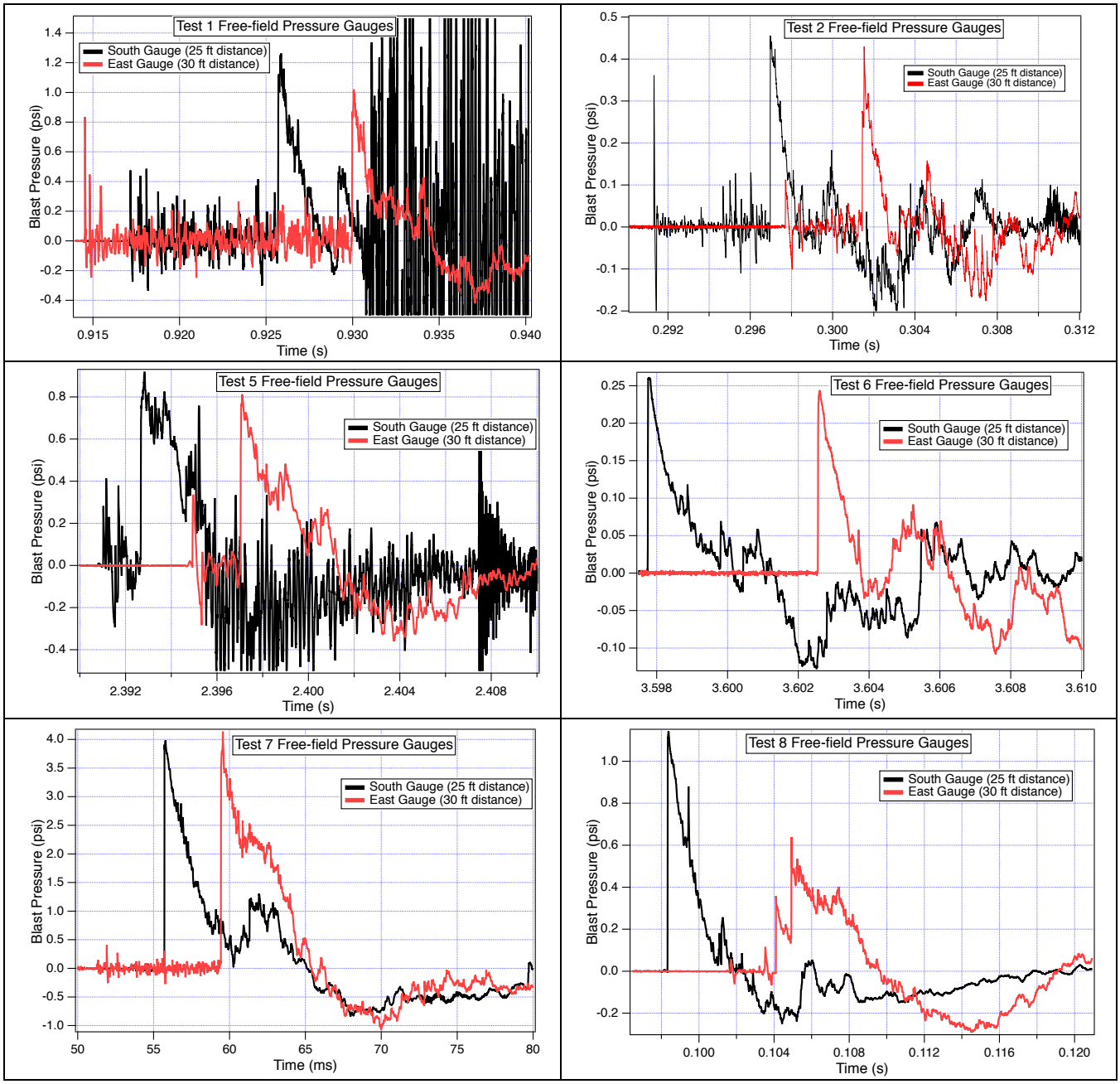

3.3. Pre- and Post-test Images

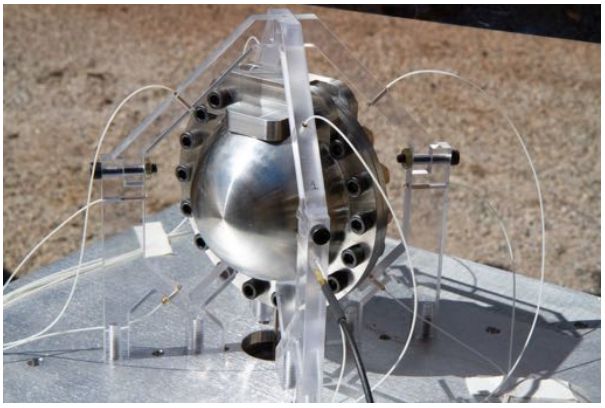

Figure 34. Test 1, 3 inch HMX powder, pre-shot.

Figure 35. Test 1 post-shot.

Figure 36. Test 1 post-shot, showing fragment penetrations through 3/4 inch plywood.

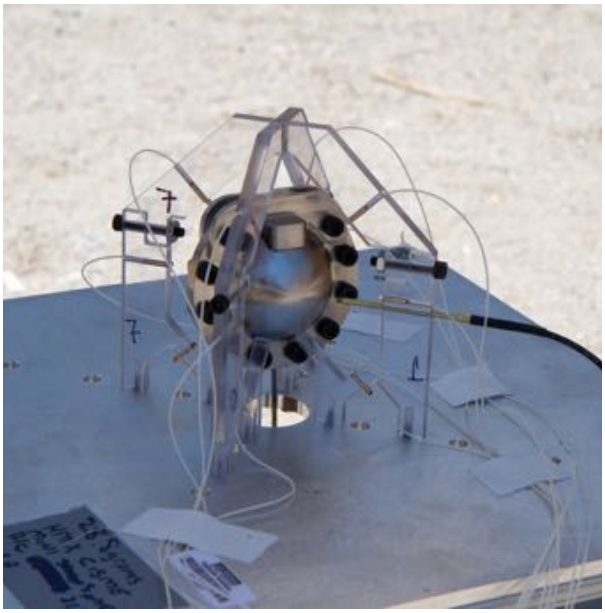

Figure 37. Test 2, 1.5 inch HMX powder, pre-shot.

Figure 38. Test 3, 10 inch prills, pre-shot.

Figure 39. Test 3, 10 inch prills, post-shot. Shot stand obliterated (original location was at middle pile of sandbag garbage).

Figure 40. Test 4, 6 inch prills, pre-shot.

Figure 41. Test 4, 6 inch prills, post-shot.

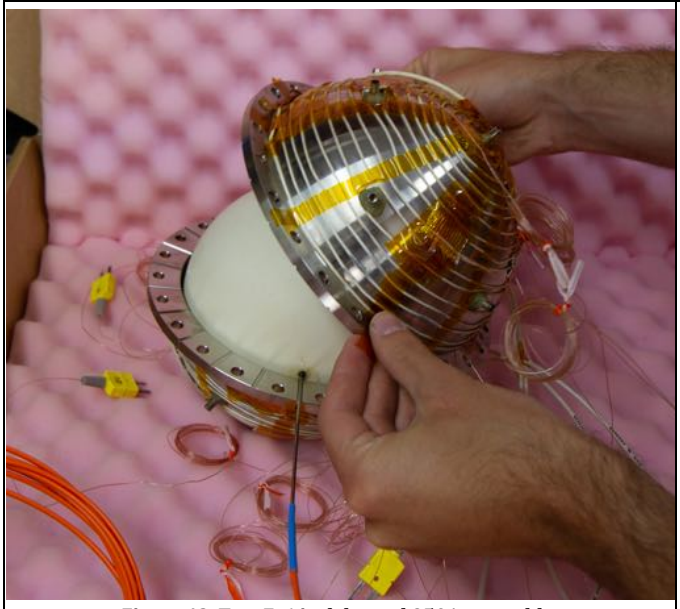

Figure 42. Test 7, 6 inch heated 9501, assembly.

Figure 43. Test 7, pre-shot.

Figure 44. Test 7, pre-shot. Additional mitigation for fragment fire prevention is shown. A 1-inch thick polycarbonate sheet is leaned against the front of the stand. Note that mitigation blocks blast gauge line-of-sight to the shot.

Figure 45. Test 7, post-shot. All parts of mitigation (excepting blocks) were obliterated.

Figure 46. Test 7, post-shot. Pitting of concrete block was caused by stainless fragments from the case.

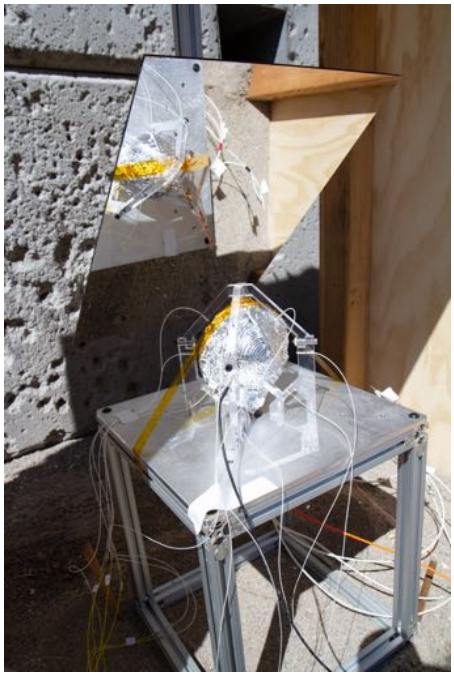

Figure 47. Test 8, 3-inch heated PBX 9501, pre-shot.

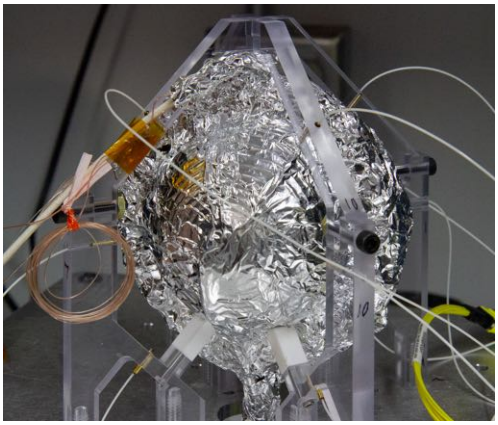

Figure 48. Test 7, pre-shot.

Figure 49. Test 7, post-shot. Shot stand damaged but not completely obliterated.

3.4. Thermal Data from Heated Tests

3.4.1. Test 7

This heated shot was started on 7/31/19 and stopped after ~6 hours due to fire concerns. Shot was allowed to cool overnight. The thermocouple data for this first day is shown in Figure 50. On the following morning (8/1/19) additional fragment mitigation was added to the shot, and then the test was restarted. There were no internal thermocouples used on this shot. The control thermocouple for Test 7 was located on the exterior surface of the stainless shell, at the north pole (labelled "TC01" in the figure). The thermocouple data for this day is shown in Figure 51.

The nominal profile used for Test 7 was:

1. Ramp rate 3˚C/min to a control setpoint of 170˚C
2. Soak at 170˚C for 6 hours
3. Ramp at 3˚C/min to a control setpoint of 180 ˚C.
4. Soak at 180 ˚C until center temperature reaches ≈165˚C
5. Fire laser to ignite shot

Duration of the ramp until setpoint of 170˚C was reached was 3.08 ks. Shot was soaked at 170˚C for 2.16 ks until 24.7 ks. Bumped setpoint of 180˚C was reached at 25.0 ks. Shot was fired at 32.46 ks (9.0 hours after the start of the test). The center temperature was 165.7 ˚C when the shot was fired.

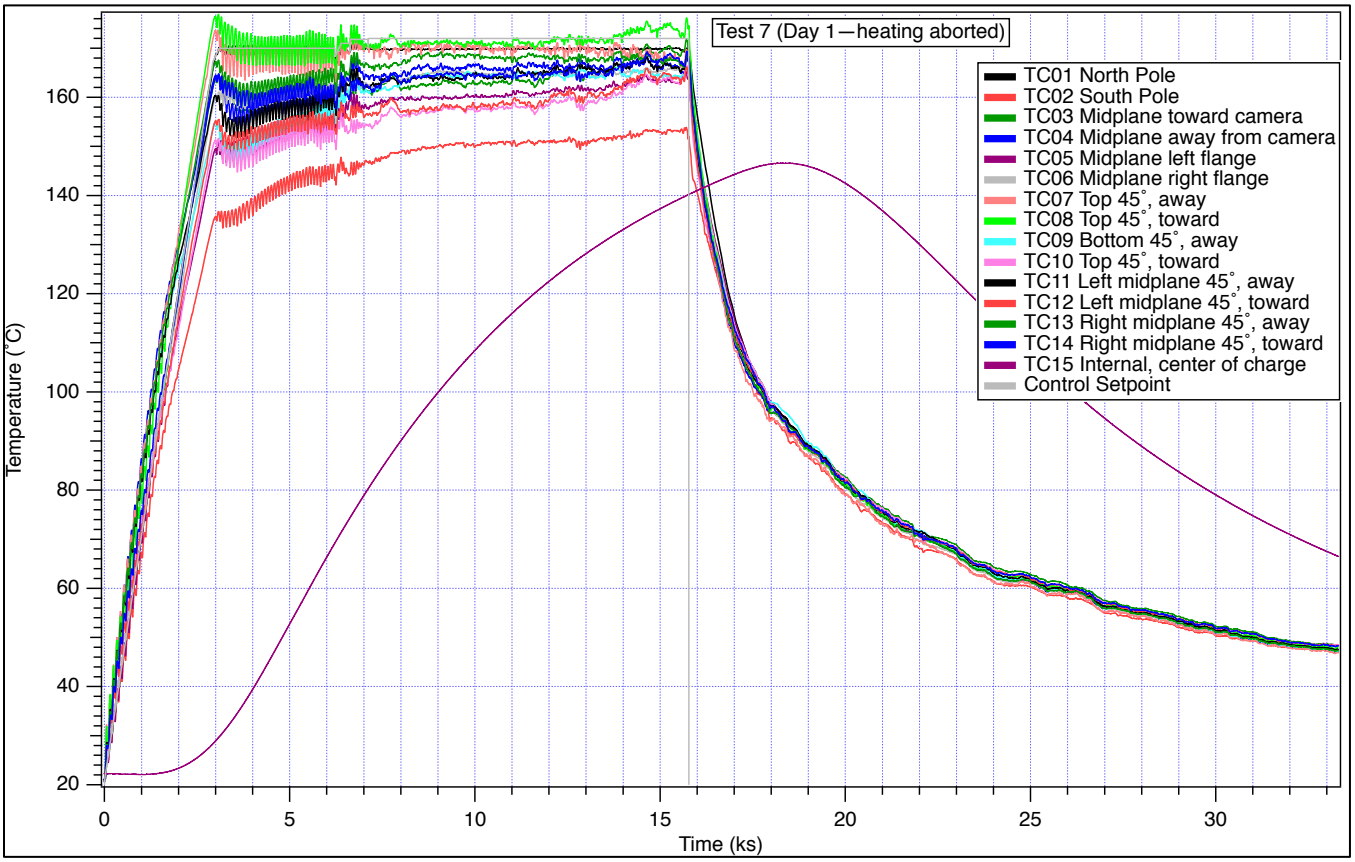

Figure 50. Thermocouple traces for Test 7, day 1, when heating was aborted.

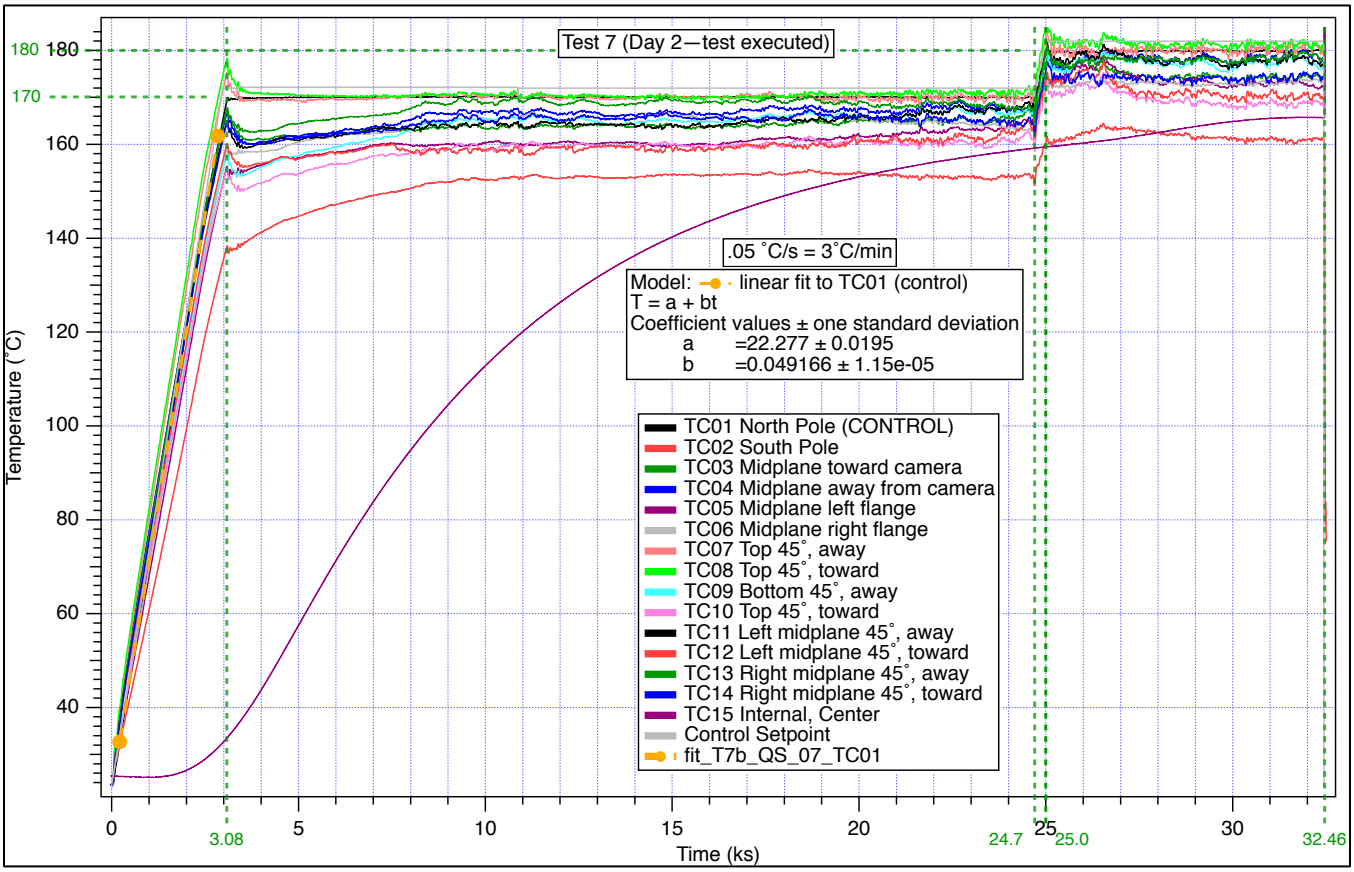

Figure 51. Thermocouple traces for Test 7, day 2, when test was executed.

3.4.2. Test 8

For Test 8, the control thermocouple location was located on the interior midplane of the hemisphere, 90˚ from the flange, on the side facing the camera (labelled TC01 in the plot). The nominal profile used for Test 8 was:

1. Ramp rate 4˚C/min to a control setpoint of 170˚C
2. Soak at 170˚C until center temperature exceeds 160˚C
3. When center temperature exceeds 160˚C, ramp at 1˚C/min to a control setpoint of 180˚C
4. Soak at 180˚C until center temperature reaches ≈165˚C.
5. Fire laser to ignite shot.

Duration of the ramp until setpoint of 170˚C was reached was at 2.10 ks. Shot was soaked at 170˚C for 7.83 ks until 9.93 ks. Bumped setpoint of 180˚C was reached at 10.81 ks. Shot was fired at 12.75 ks (3.5 hours after the start of the test). The center temperature was 165.7 ˚C when shot was fired.

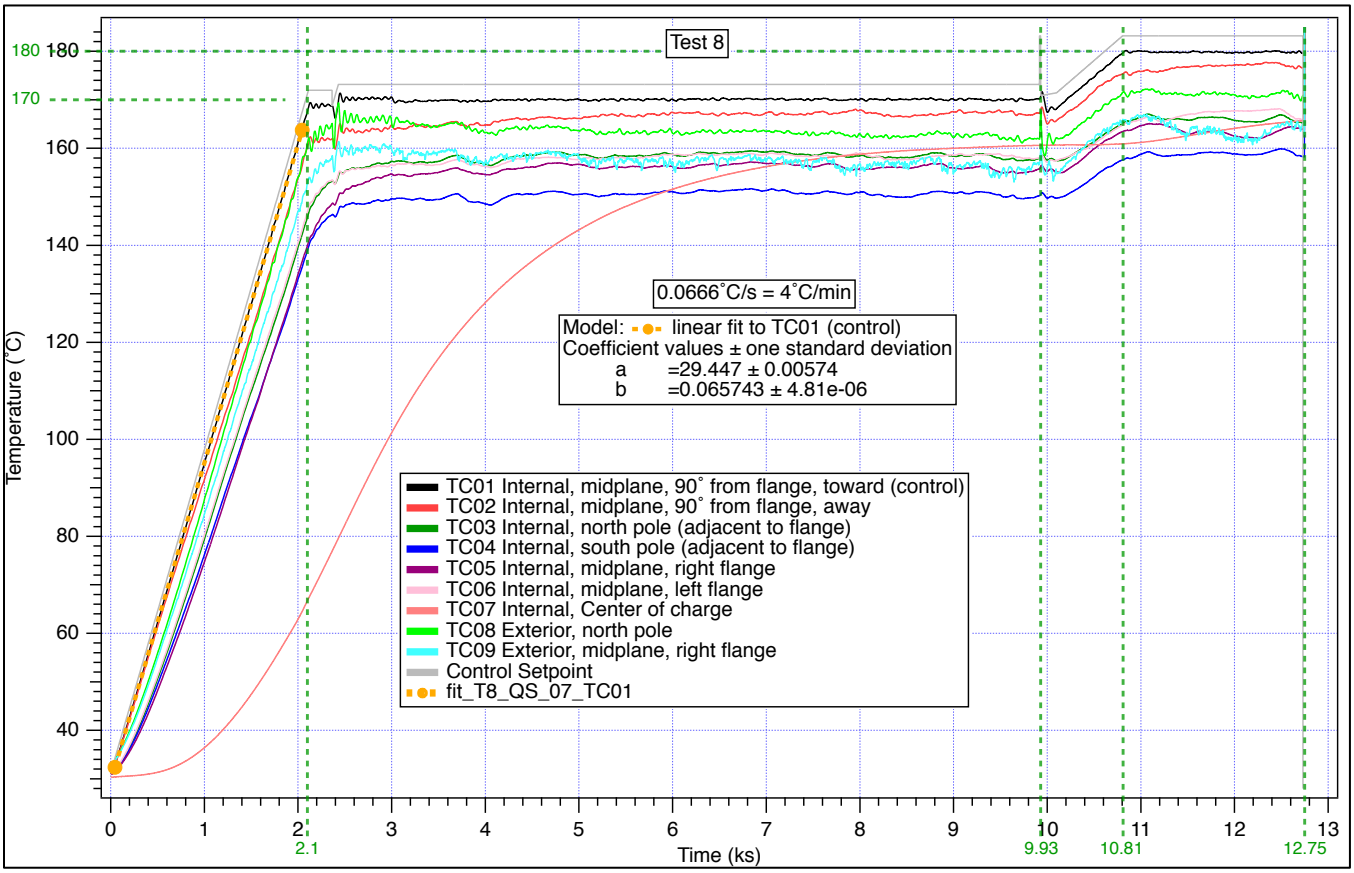

Figure 52. Thermocouple traces for Test 8. Note the small anomaly at the beginning of the first soak: the initial software setpoint of 170˚C resulted in an actual control TC setpoint of 167˚ C, so the software setpoint was increased to 173˚C and an actual control TC setpoint of 170˚ C was attained. On the second soak, a software setpoint of 183˚C was used to reach an actual setpoint of 180˚ C.

3.5. PDV Spectrograms

In the following spectrograms, the time shown on the horizontal axis is relative to the piezo pin impact trigger (3 mm from initial surface). Pin locations are depicted in Figure 57.

Each spectrogram provides a time resolved trace of free surface velocity located within the probes beam path. For spectrograms recorded on a heterodyne system, laser mixing produces a constant beat frequency at the difference between the reference and signal light. This appears in the heterodyne spectrograms below as a constant zero baseline near 0.9 km/s. As the target surface moves towards the probe, the baseline velocity must be subtracted from the recorded to produce the actual velocity. For all the spectrograms presented, strong return light intensity is shown as a dark red trace. As the intensity drops the color map cools to yellow, green, and finally blue.

Table 11. Test 1 (3-inch diameter HMX powder) PDV spectrograms

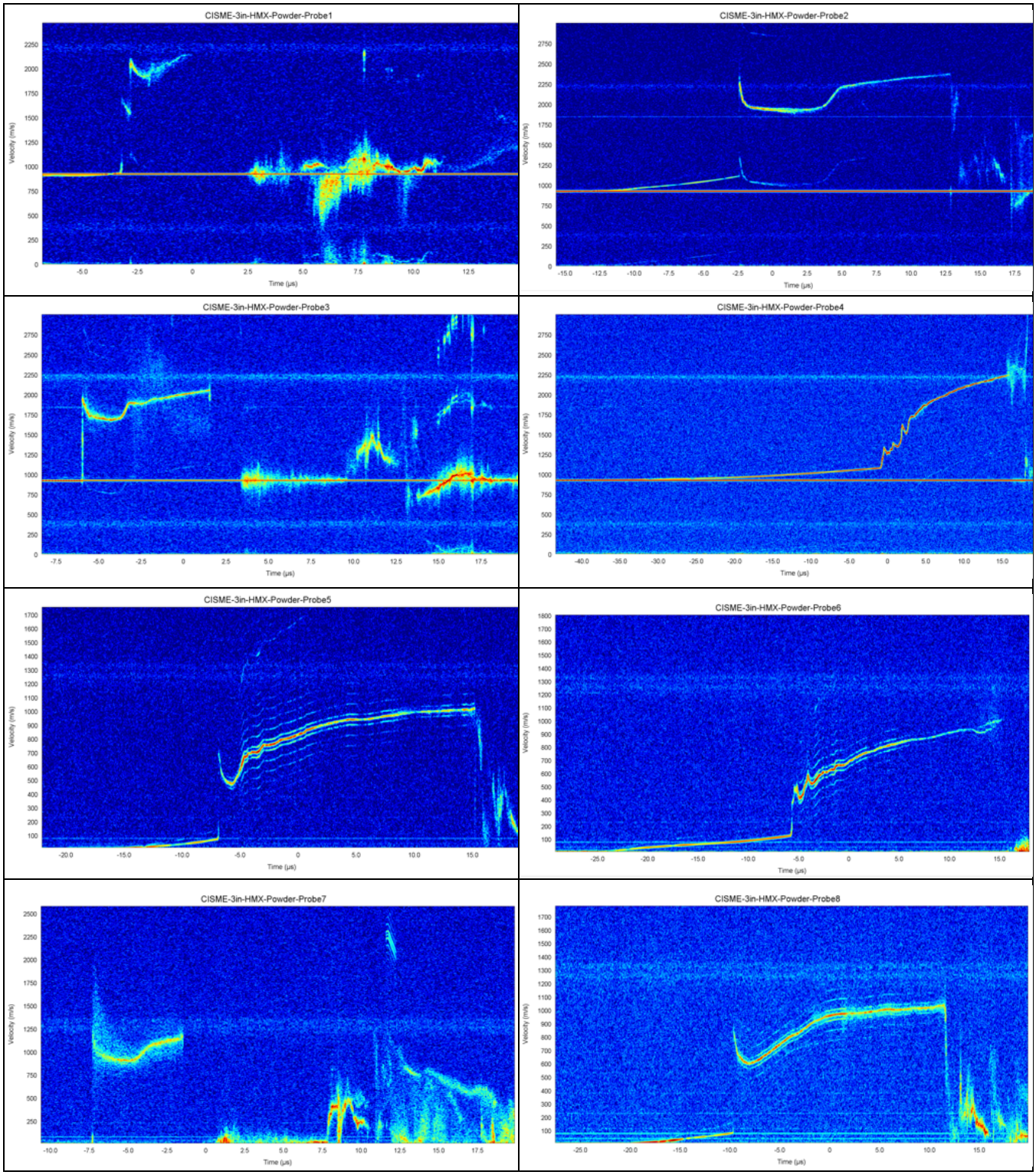

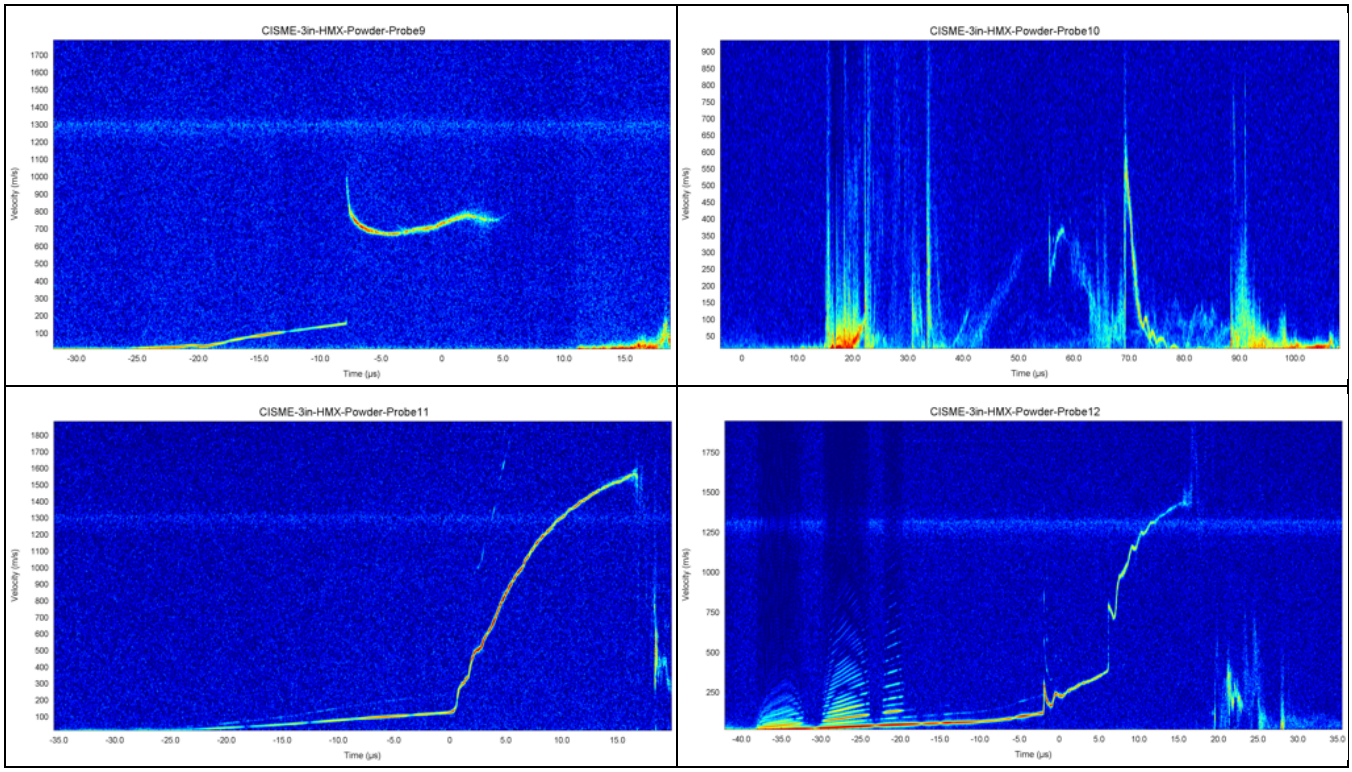
CISME-3in-HMX-Powder-Probe9
CISME-3in-HMX-Powder-Probe10
CISME-3in-HMX-Powder-Probe11
CISME-3in-HMX-Powder-Probe12
Velocity (m/s)
Time (µs)

Table 12. Test 2 (1.5-inch diameter HMX powder) PDV spectrograms

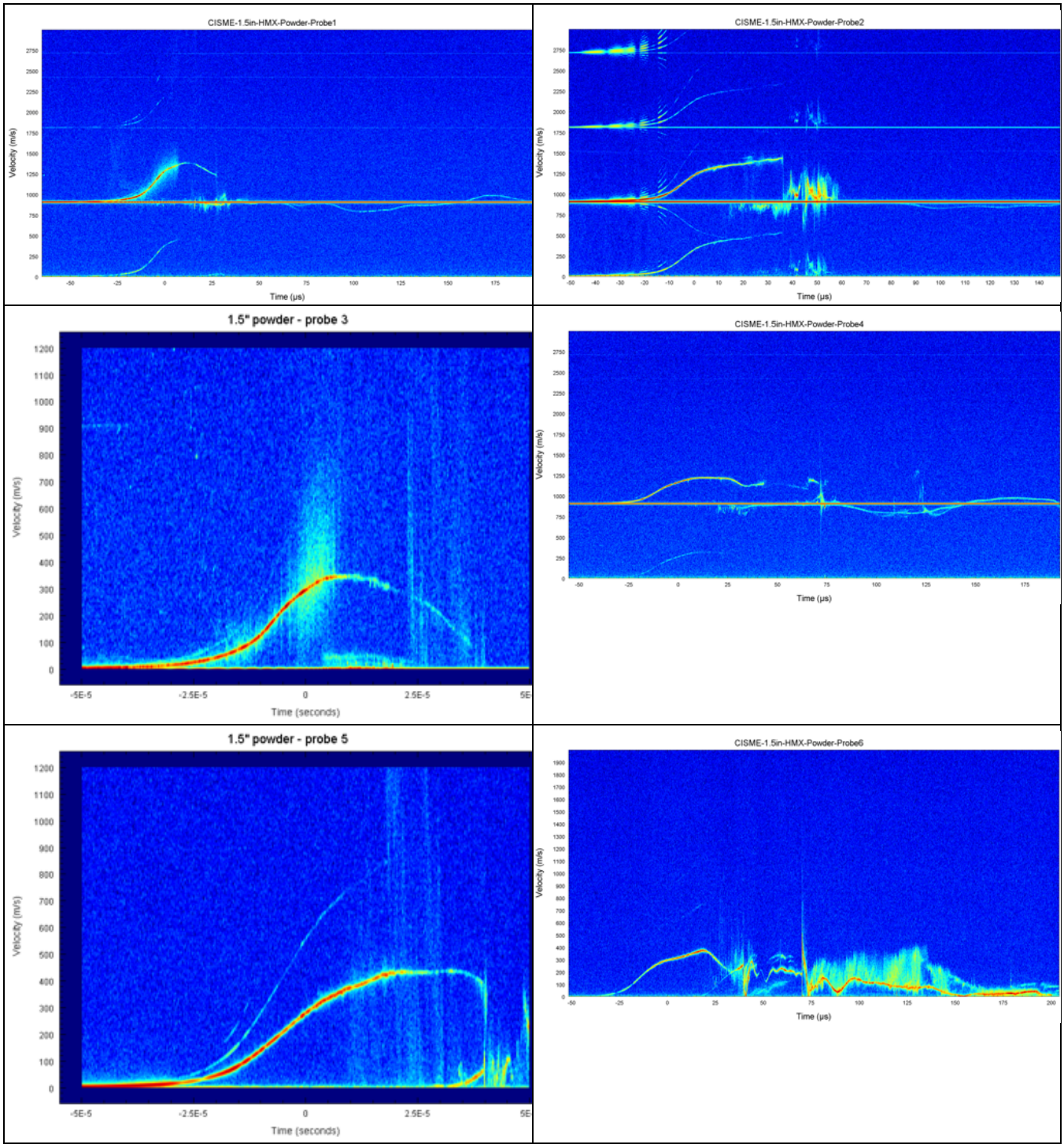

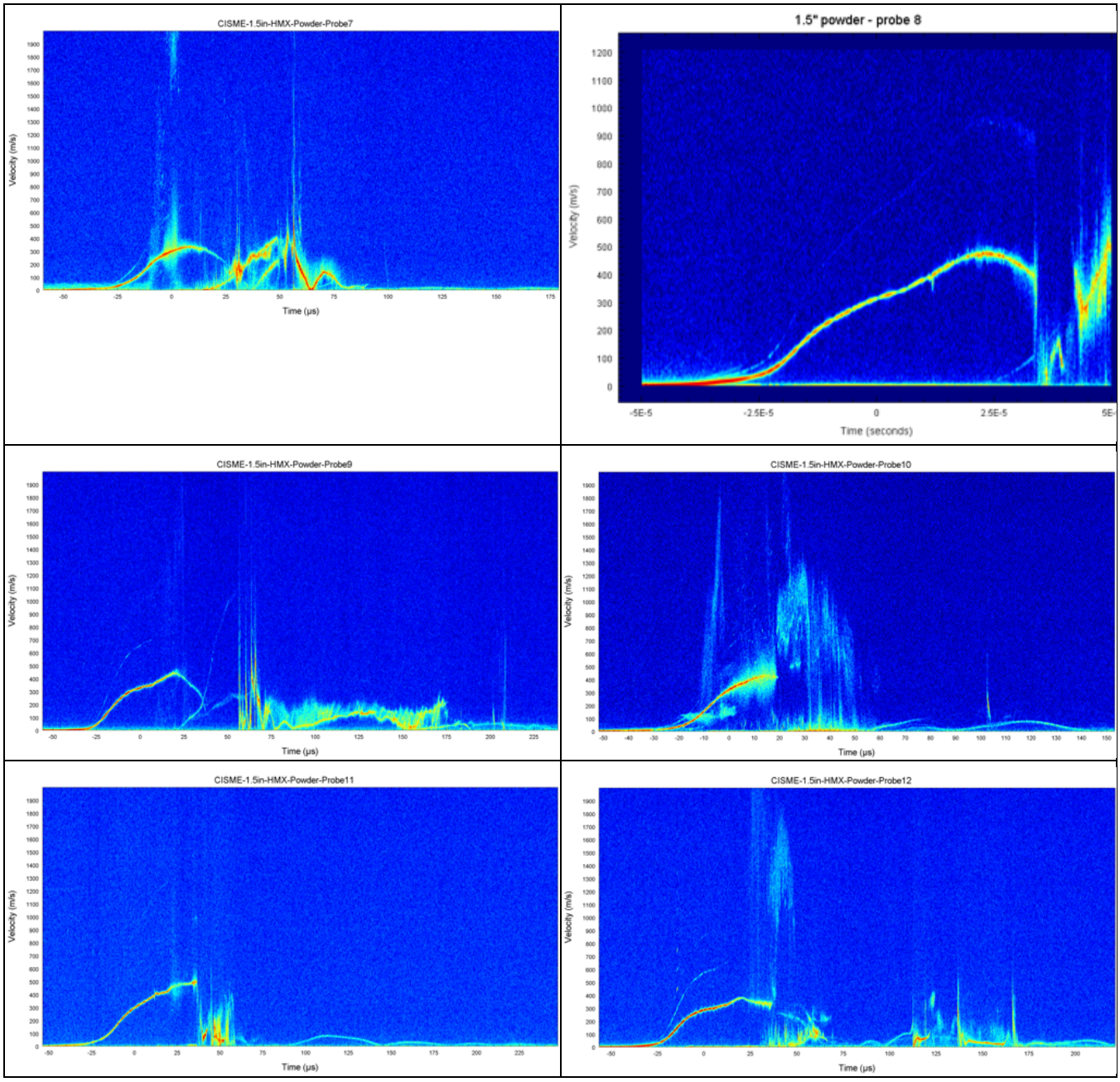
CISME-1.5in-HMX-Powder-Probe7
Velocity (m/s)
Time (µs)
1.5" powder - probe 8
Velocity (m/s)
Time (seconds)
CISME-1.5in-HMX-Powder-Probe9
Velocity (m/s)
Time (µs)
CISME-1.5in-HMX-Powder-Probe10
Velocity (m/s)
Time (µs)
CISME-1.5in-HMX-Powder-Probe11
Velocity (m/s)
Time (µs)
CISME-1.5in-HMX-Powder-Probe12
Velocity (m/s)
Time (µs)

Table 13. Test 3 (10-inch diameter prills) PDV spectrograms

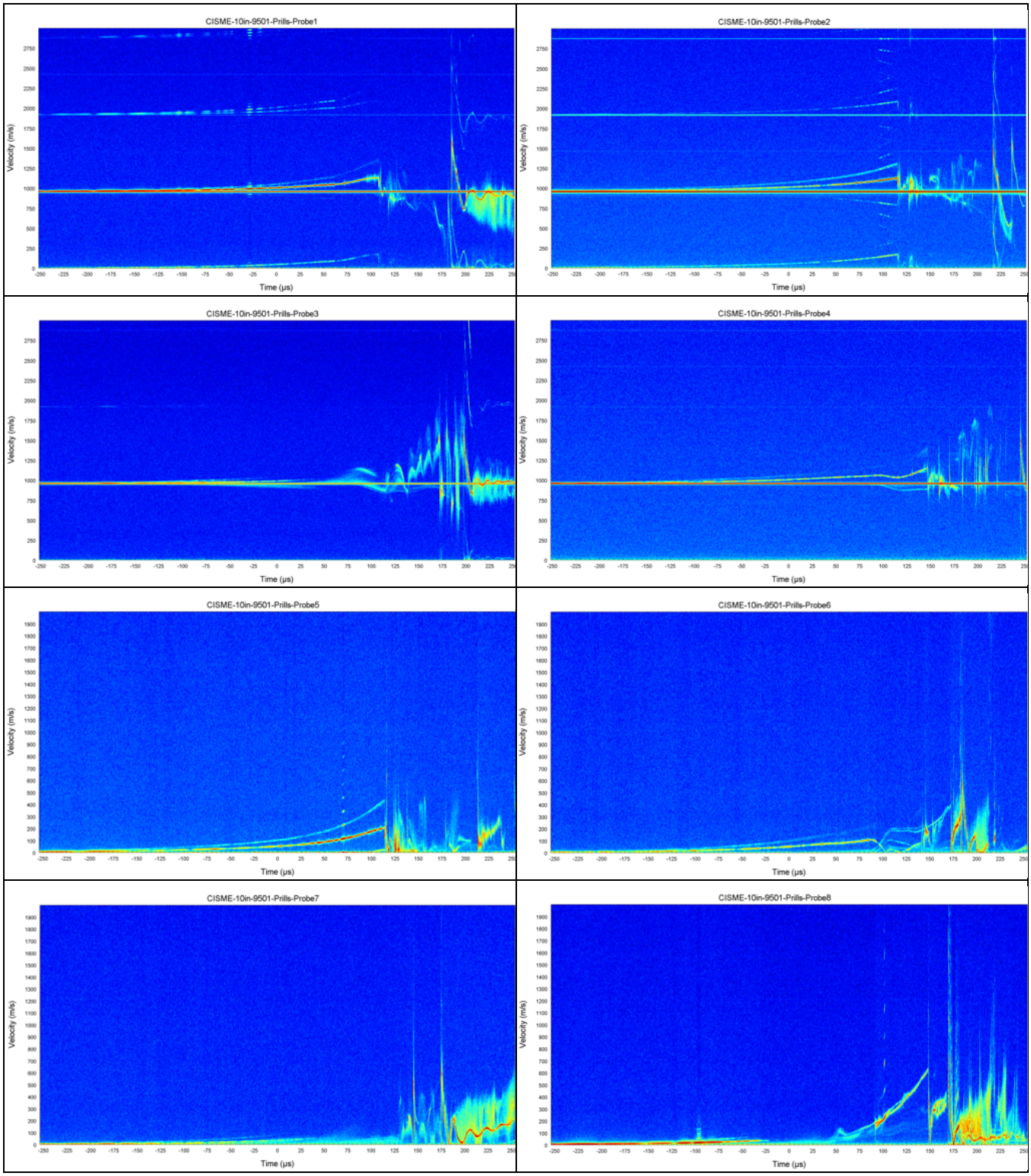

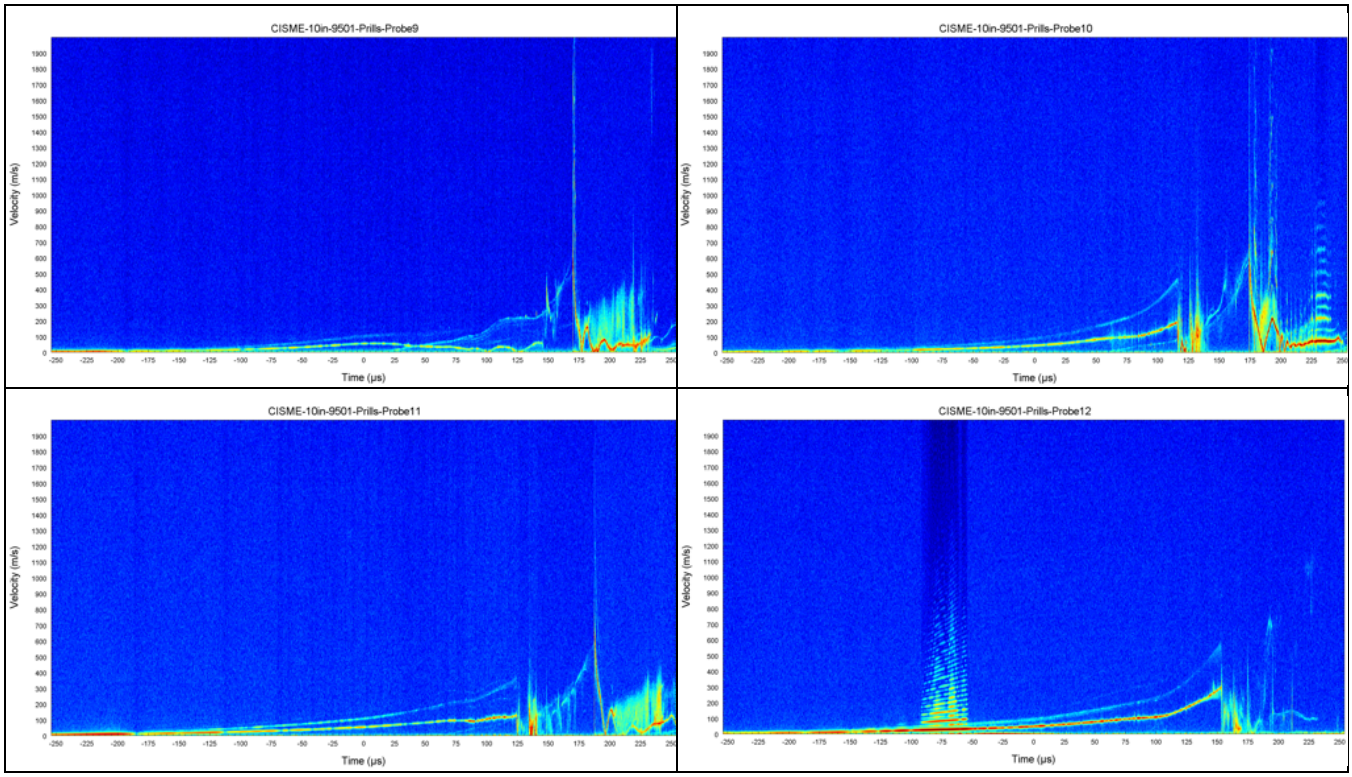
CISME-10in-9501-Prills-Probe9
CISME-10in-9501-Prills-Probe10
CISME-10in-9501-Prills-Probe11
CISME-10in-9501-Prills-Probe12
Velocity (m/s)
Time (µs)

Table 14. Test 4 (6-inch diameter prills) PDV spectrograms

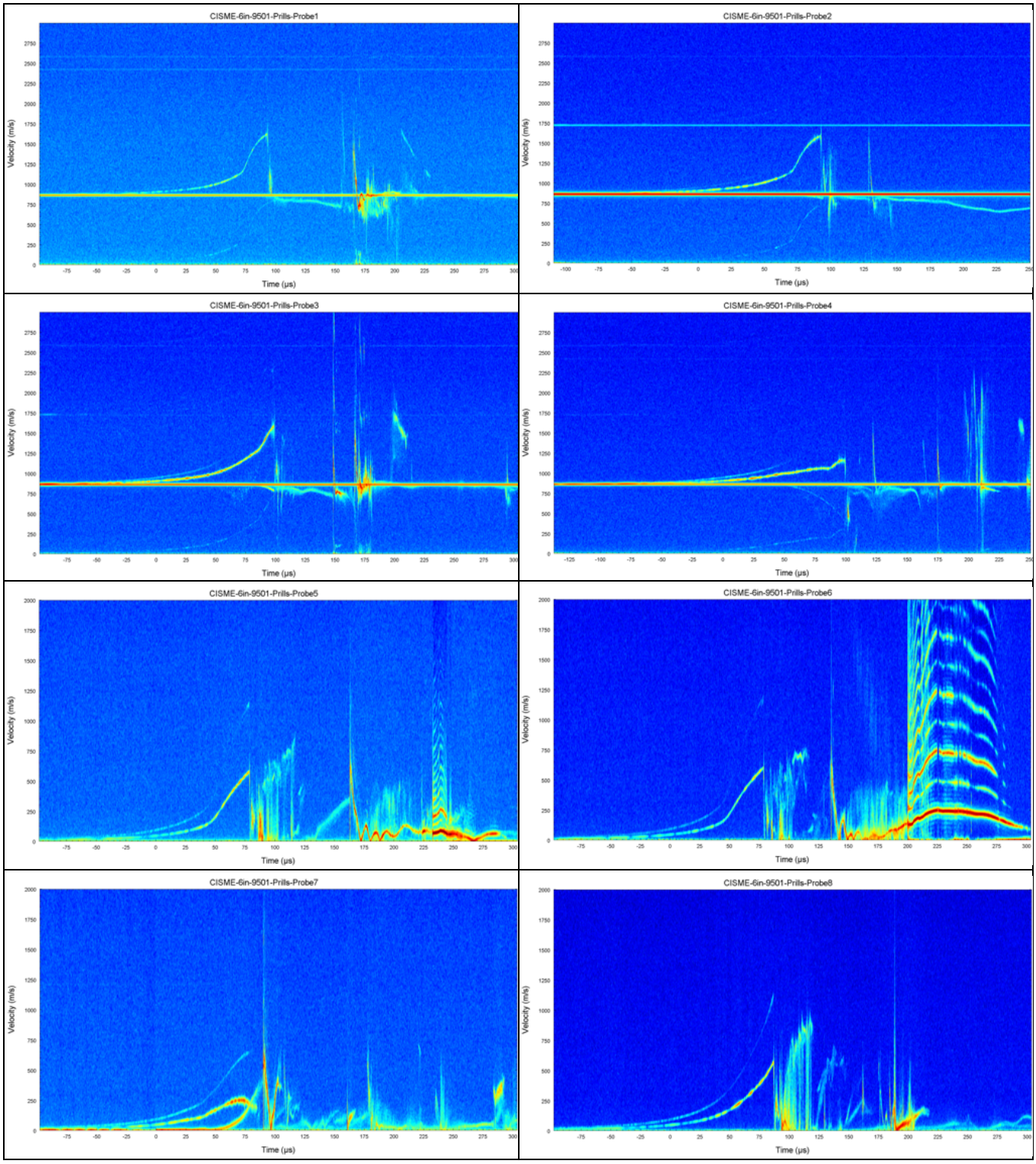

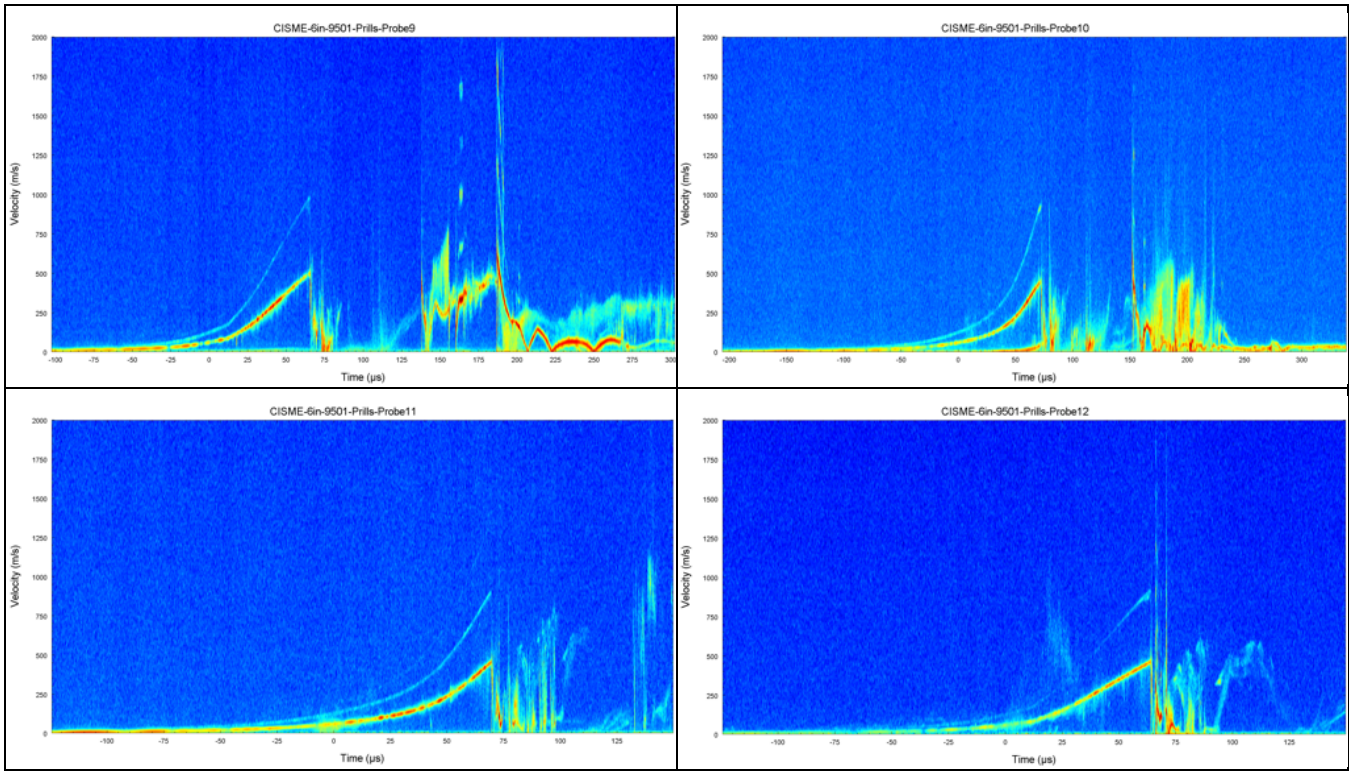
CISME-6in-9501-Prills-Probe9
Velocity (m/s)
Time (µs)
CISME-6in-9501-Prills-Probe10
Velocity (m/s)
Time (µs)
CISME-6in-9501-Prills-Probe11
Velocity (m/s)
Time (µs)
CISME-6in-9501-Prills-Probe12
Velocity (m/s)
Time (µs)

Table 15. Test 5 (3-inch diameter prills) PDV spectrograms

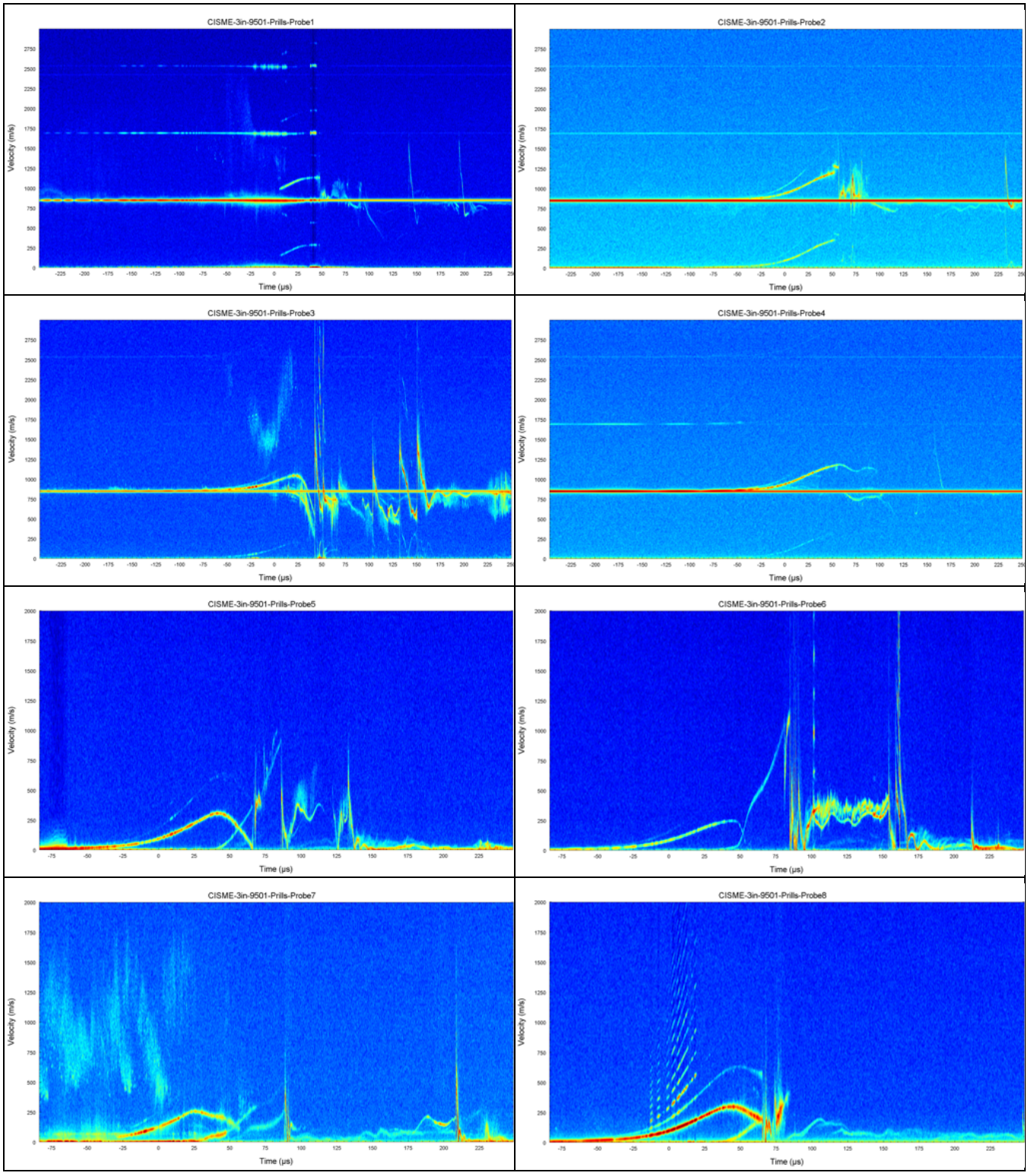

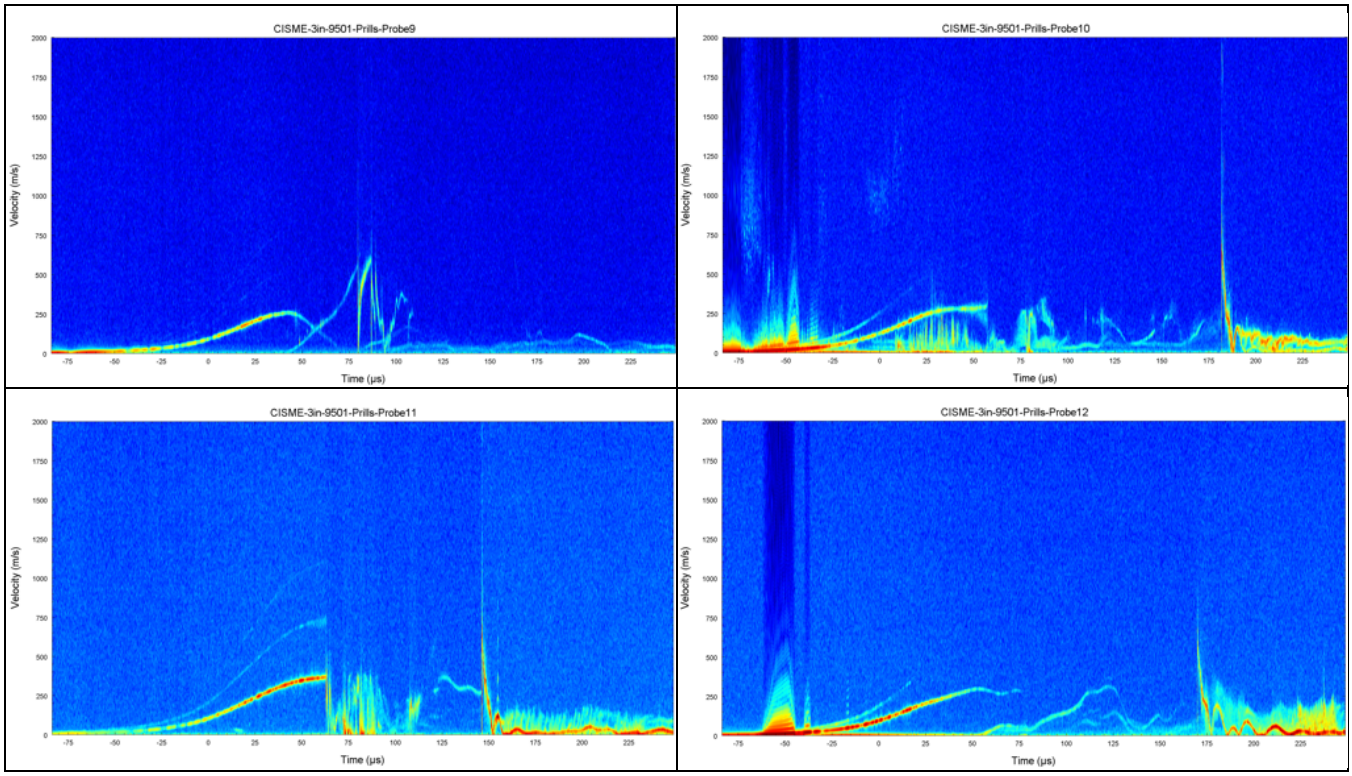
CISME-3in-9501-Prills-Probe9
CISME-3in-9501-Prills-Probe10
CISME-3in-9501-Prills-Probe11
CISME-3in-9501-Prills-Probe12
Velocity (m/s)
Time (µs)

Table 16. Test 6 (1.5-inch diameter prills) PDV spectrograms

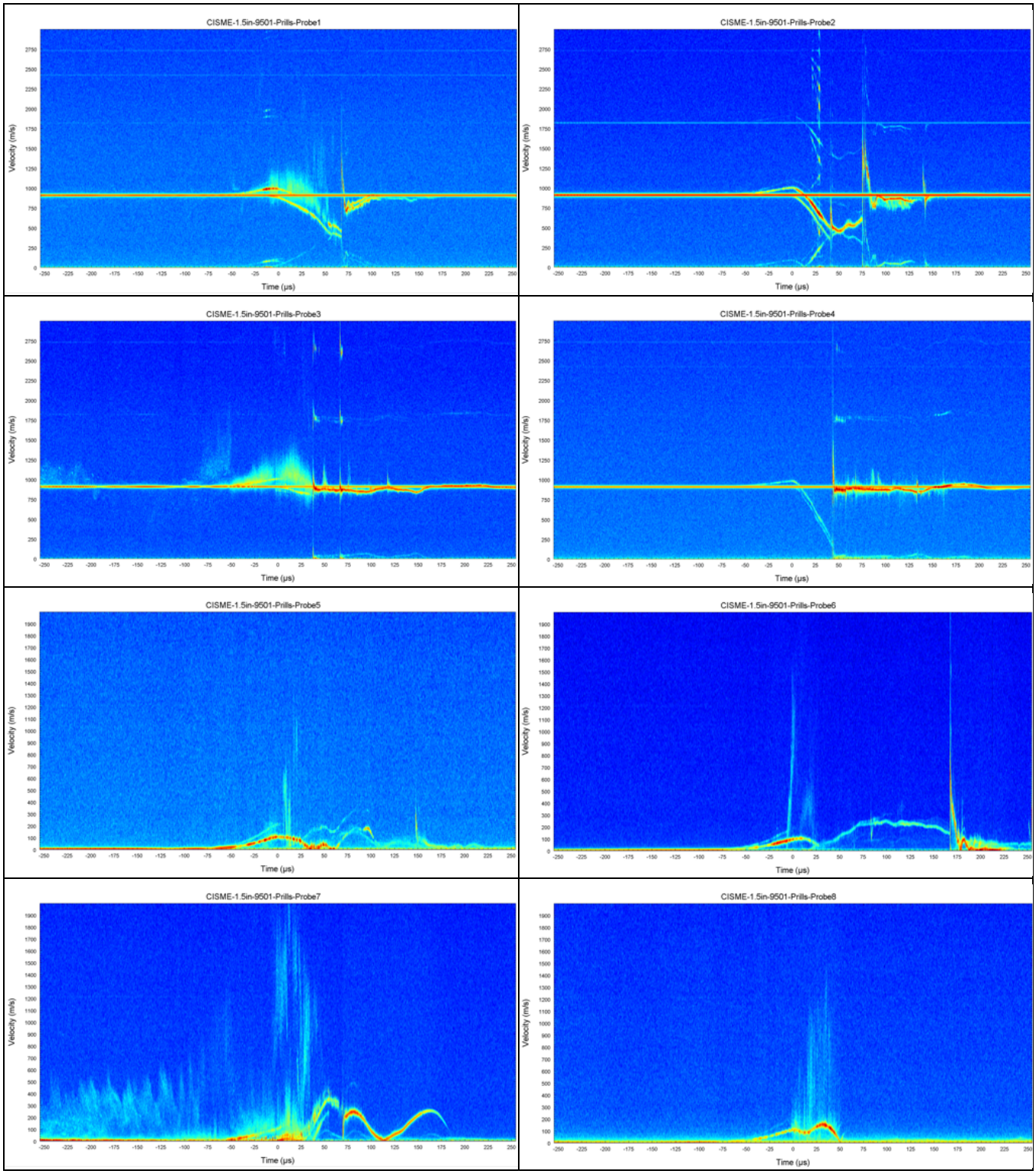

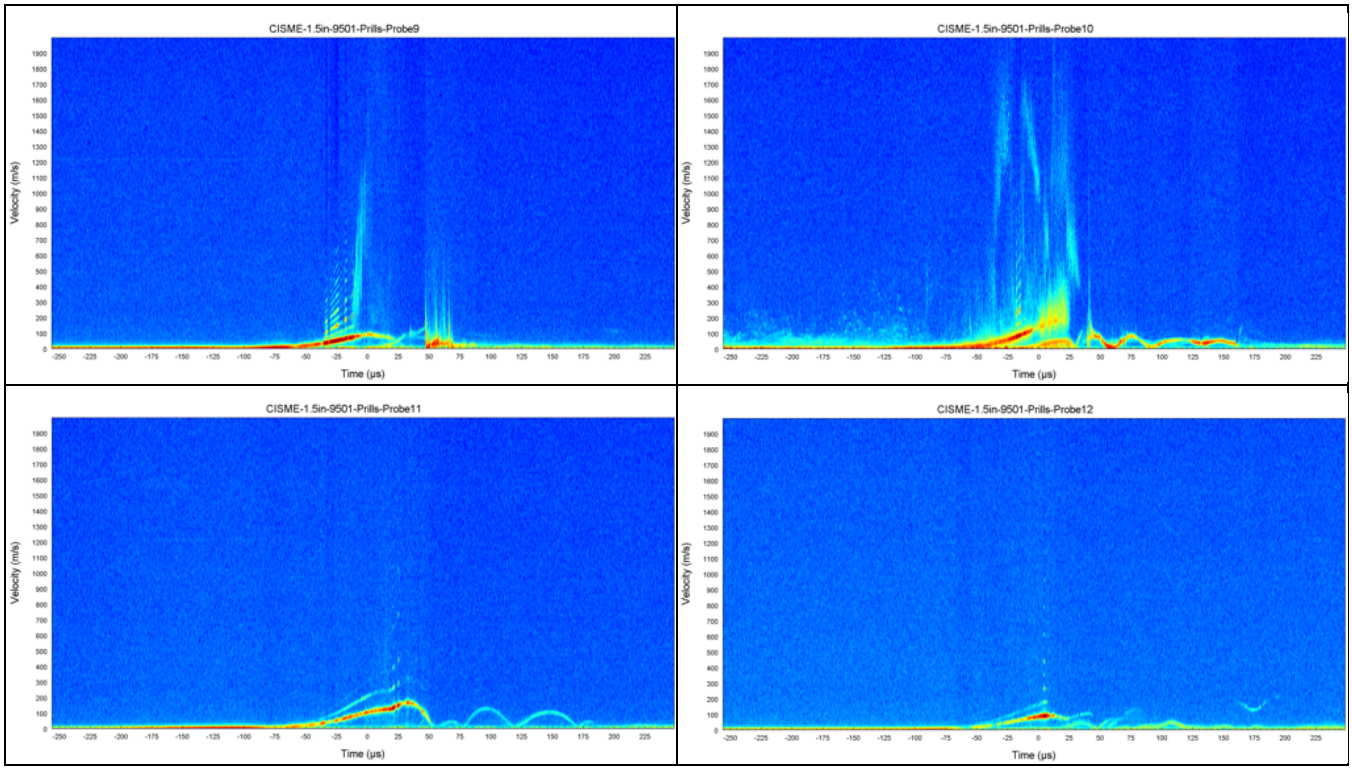
CISME-1.5in-9501-Prills-Probe9
CISME-1.5in-9501-Prills-Probe10
CISME-1.5in-9501-Prills-Probe11
CISME-1.5in-9501-Prills-Probe12
Velocity (m/s)
Time (µs)

Table 17. Test 7 (6-inch diameter heated PBX 9501) PDV spectrograms

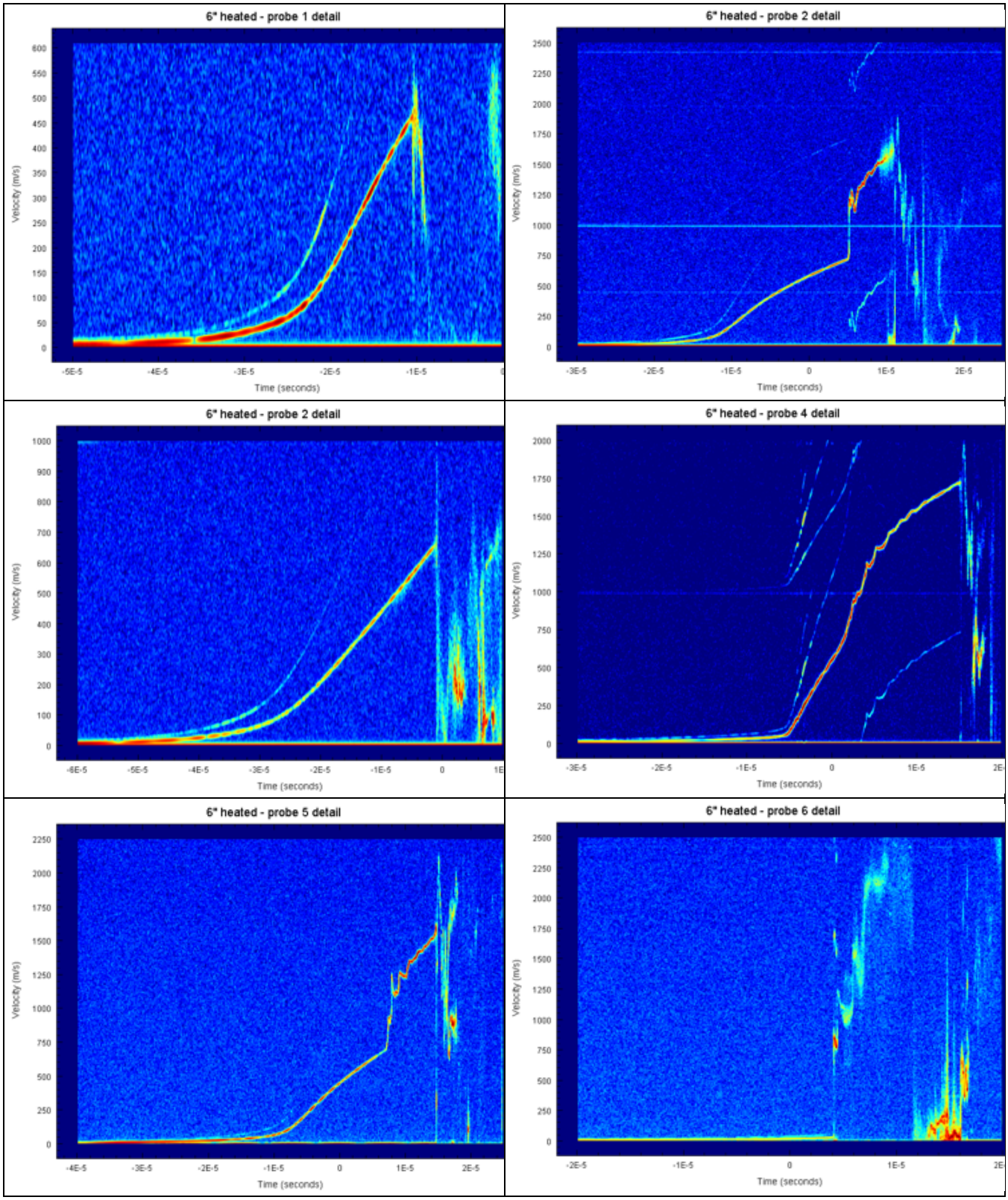

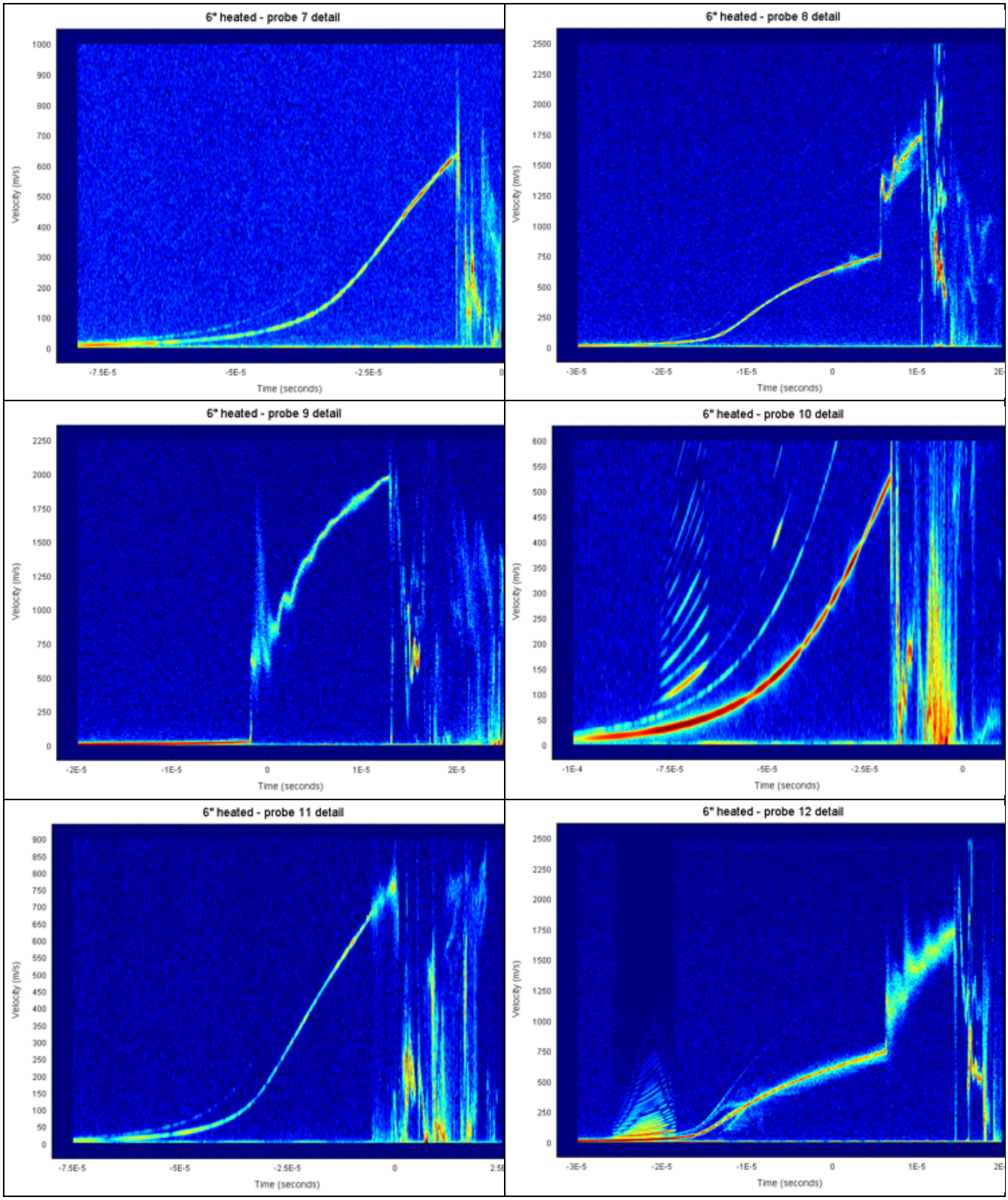
6" heated - probe 7 detail
Velocity (m/s)
Time (seconds)
6" heated - probe 8 detail
Velocity (m/s)
Time (seconds)
6" heated - probe 9 detail
Velocity (m/s)
Time (seconds)
6" heated - probe 10 detail
Velocity (m/s)
Time (seconds)
6" heated - probe 11 detail
Velocity (m/s)
Time (seconds)
6" heated - probe 12 detail
Velocity (m/s)
Time (seconds)

Table 18. Test 8 (3-inch diameter heated PBX 9501) PDV spectrograms

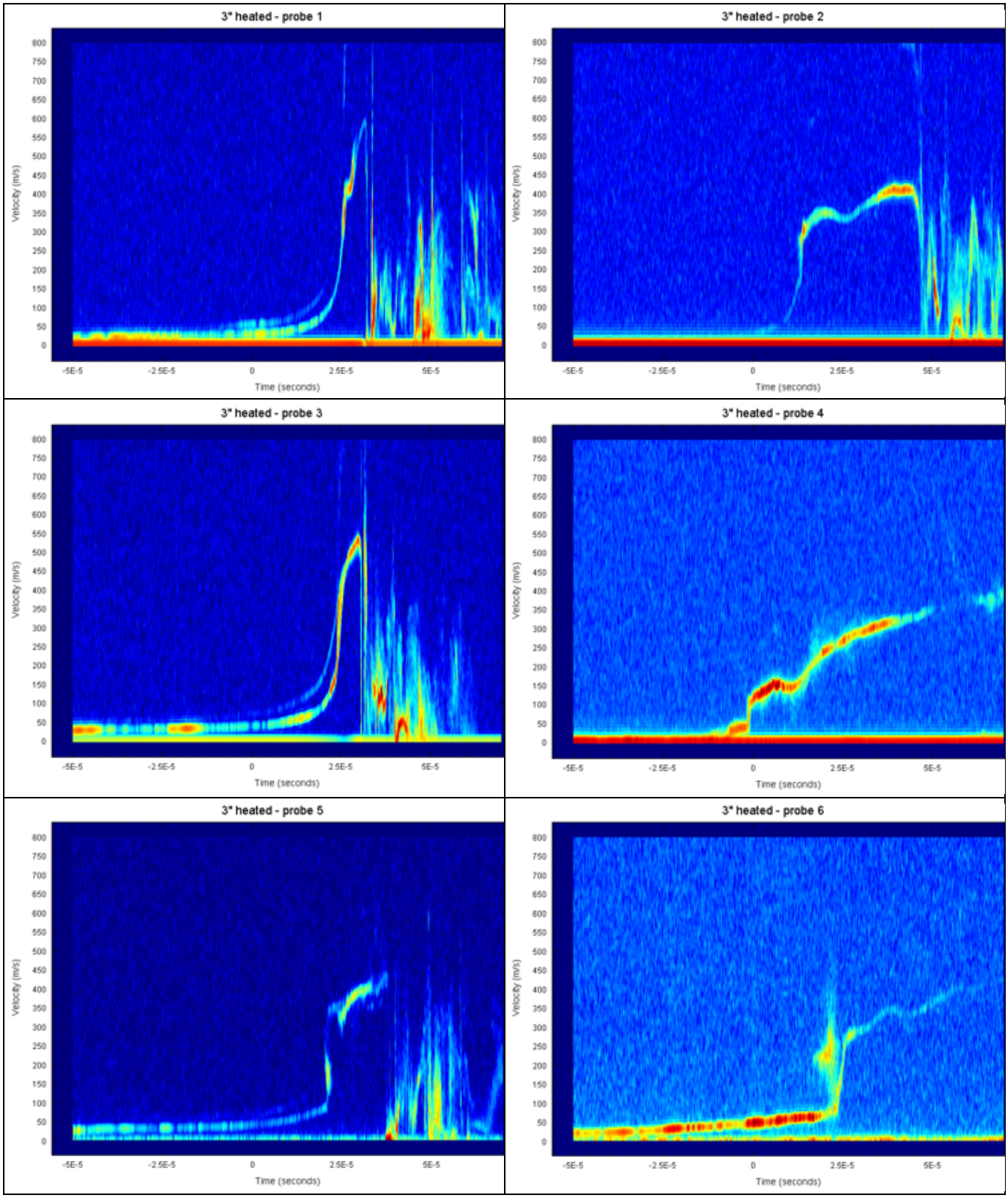

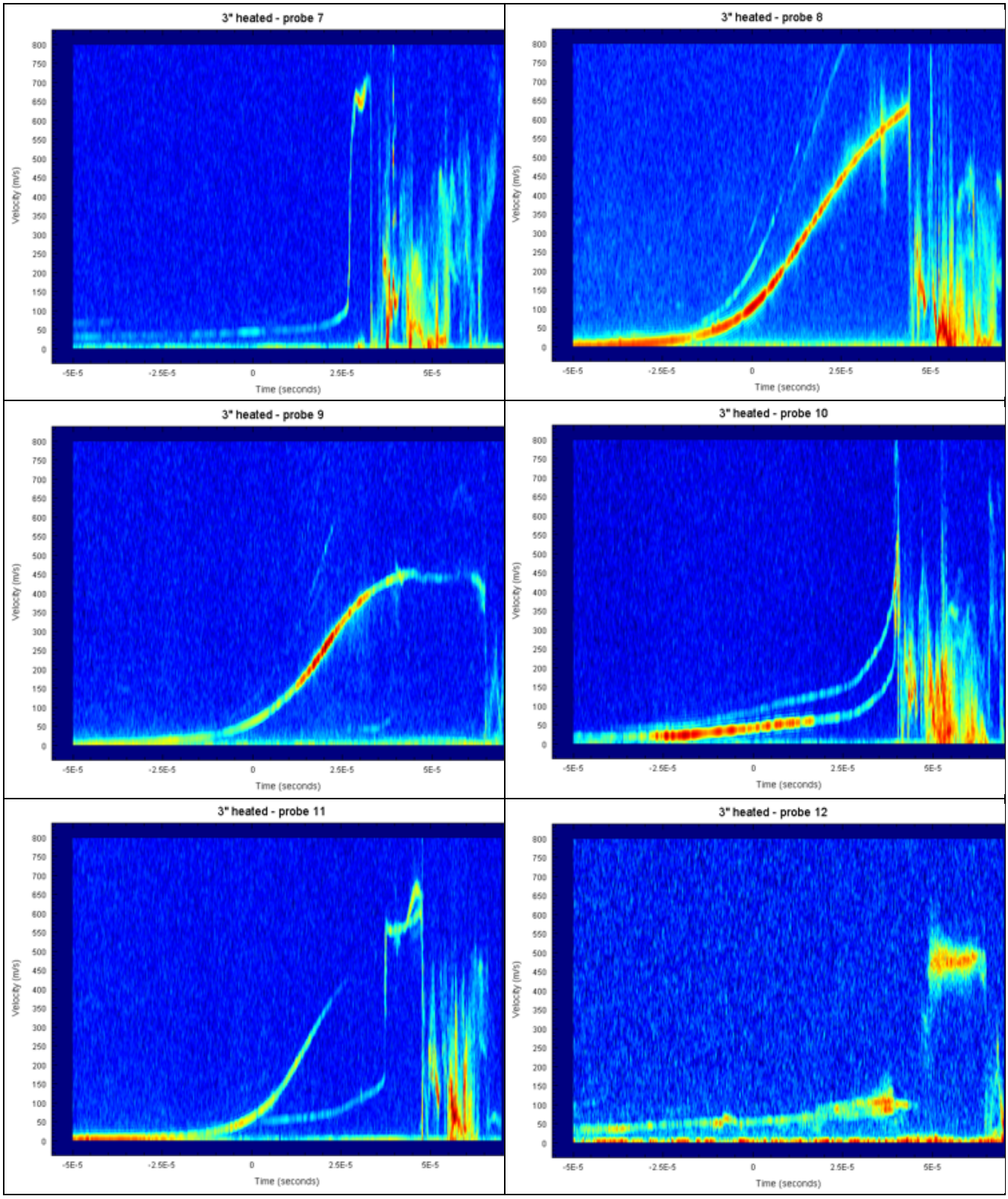
3" heated - probe 7
3" heated - probe 8
3" heated - probe 9
3" heated - probe 10
3" heated - probe 11
3" heated - probe 12
Velocity (m/s)
Time (seconds)
-5E-5
-2.5E-5
0
2.5E-5
5E-5

4. Discussion

4.1. Idealized Shock Analysis

To obtain a theoretical upper limit for the anticipated jump-off velocity, we calculate the anticipated jump-off velocity in the idealized scenario of pristine PBX 9501, center initiated (e.g. with a detonator), generating a CJ detonation that travels radially outward to transit the steel shell. When the detonation wave reaches the explosive-steel interface, we will have a forward-going shock into the pristine stainless and a reflected shock of equal pressure into the reaction products of the PBX 9501. We will equate expressions for pressure, obtained by generating "P-u" (pressure-particle velocity) Hugoniots for the steel and the explosive detonation products, to obtain the particle velocity in the outgoing shock in the steel. Using the free-surface approximation, the jump-off velocity at the exterior of the stainless is twice the calculated particle velocity (the jump-off velocity is the quantity measured using PDV).

We construct the Hugoniot for the stainless using the form,

$$P = \rho_0 C_0 u + \rho_0 s u^2 \tag{1}$$

Where P is shock pressure, ρ_0 is nominal 304 stainless steel density, C_0 and s are the empirically-derived Hugoniot parameters, and u is the shock particle velocity. Values for these parameter are taken from [2], p. 189 and listed in Table 19.

Table 19. Hugoniot constants for 304 stainless steel, from [2] page 189.

	c (km/s)	s (unitless)	ρ_0 (g/cc)
304 Stainless Steel	4.569	1.490	7.896

The resulting Hugoniot is,

$$P = 36.08\,u + 11.77\,u^2 \qquad (\mathrm{GPa}) \tag{2}$$

Where u is particle velocity (not jump-off velocity). We construct the Hugoniot for PBX 9501 reaction products using an empirically-derived approximation ([2], p. 267),

$$P = \left(2.414 - 1.7315\frac{u}{u_{CJ}} + 0.3195\frac{u^2}{u_{CJ}^2}\right) P_{CJ} \tag{3}$$

Where u_{CJ} is the particle velocity of the CJ detonation and P_{CJ} is the CJ pressure. We obtain $P_{CJ} = 37.54\,\mathrm{GPa}$ (for explosive with a pre-reaction density of $\rho_0 = 1.834\,\mathrm{g\ cc^{-1}}$) from the JWL equation of state [30], and the detonation velocity $D = 8.792\,\mathrm{km\ s^{-1}}$ from reference [31], p.114. We use these values to calculate u_{CJ} from the jump equations:

$$u_{CJ} = \frac{P_{CJ}}{\rho_0 D} = 2.328\,\mathrm{km\ s^{-1}} \tag{4}$$

The jump condition for the steel-explosive shock interaction requires that both pressure and particle velocity at the interface are equal. Setting equal the pressure of the forward-going shock in the steel and the reflected shock into the reacted PBX 9501, eliminating unknowns, and solving the resulting quadratic we obtain $u = 1.20\,\mathrm{km\ s^{-1}}$. The jump-off velocity u_j at the surface of the steel is therefore predicted to be $u_j = 2u = 2.40\,\mathrm{km\ s^{-1}}$. Substituting this back into (1), we obtain a shock pressure of 60 GPa. This Hugoniot shock match is shown graphically in Figure 53.

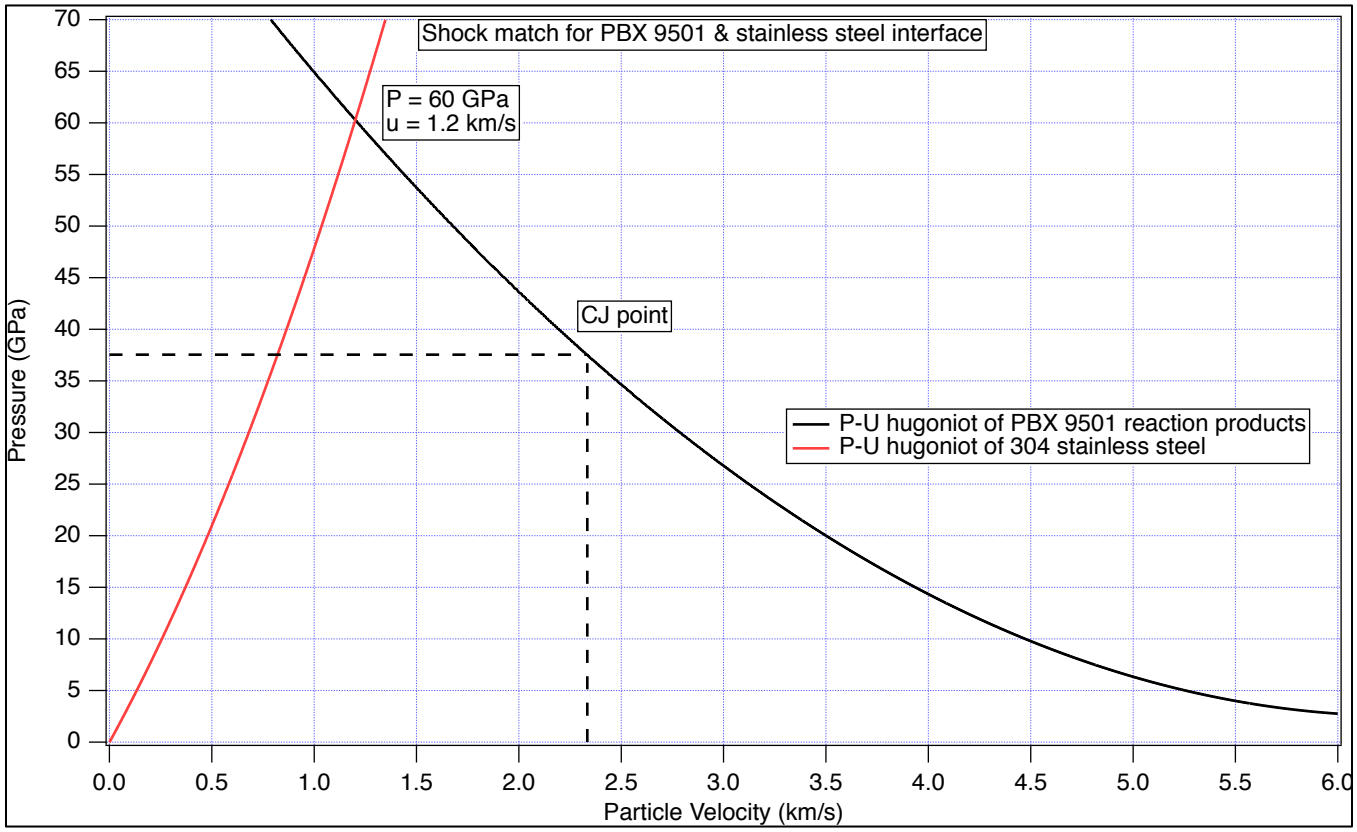

Figure 53. Graphical solution for P-u hugoniot intersection for stainless steel with PBX 9501 detonation products.

This analysis does not account for attenuation of the shock through the thickness of the steel from the release wave behind the detonation. The shock produced by the CJ detonation at the inner surface of the steel would be 60 GPa; the shock will be less than 60 GPa by the time it reaches the outer surface, depending on the thickness of the steel and the shape of the rarefaction wave behind the detonation front (refer to Davis in reference [32]). The rarefaction wave behind the detonation front will depend on the mass of explosive in the shot; larger explosive mass will produce a flatter relief wave behind the shock front, minimizing attenuation.

The analysis above provides us with a "worst-case" benchmark calculation of the expected steel shock pressure and observed jump-off velocity for the idealized scenario of pristine PBX 9501 at nominal density undergoing a nominal CJ detonation. This is not the detonation behavior that we would anticipate from thermally and physically damaged inhomogeneous PBX 9501 at potentially reduced density and energy content which may be pre-stressed and partially reacted. In section 4.5 we use the observed jump-off velocities to calculate the actual shock pressures attained in the experiments.

4.2. Divergent flow and the effect of shock curvature on observed jump-off velocity in the idealized perfect detonation scenario

In the idealized scenario of a center-initiated detonation, the detonation wave propagates outward on a curved surface. Divergent flow may play a role and we briefly address that here. We separately consider the effect of divergence on the detonation in the explosive and the shock through the inert stainless-steel shell.

The effect that curvature has on detonation properties of PBX 9501 has been investigated. Detonation Shock Dynamics (DSD) theory captures the effect of curvature on detonation properties as a reduction in detonation velocity. Figure 54 is reproduced from reference [33], and shows the variation in detonation velocity of PBX 9501 as a function of inverse radius of curvature.

We have placed the dotted line on the figure at a curvature radius of 19 mm, which is the radius of our smallest 1.5-inch diameter charge. The figure shows that, at this curvature, detonation velocity is reduced approximately 1%

(from 8.8 to 8.8 km/s). This is therefore a small effect even in our smallest charge, and the assumption of nominal CJ detonation velocity and pressure at the explosive-steel interface is valid.

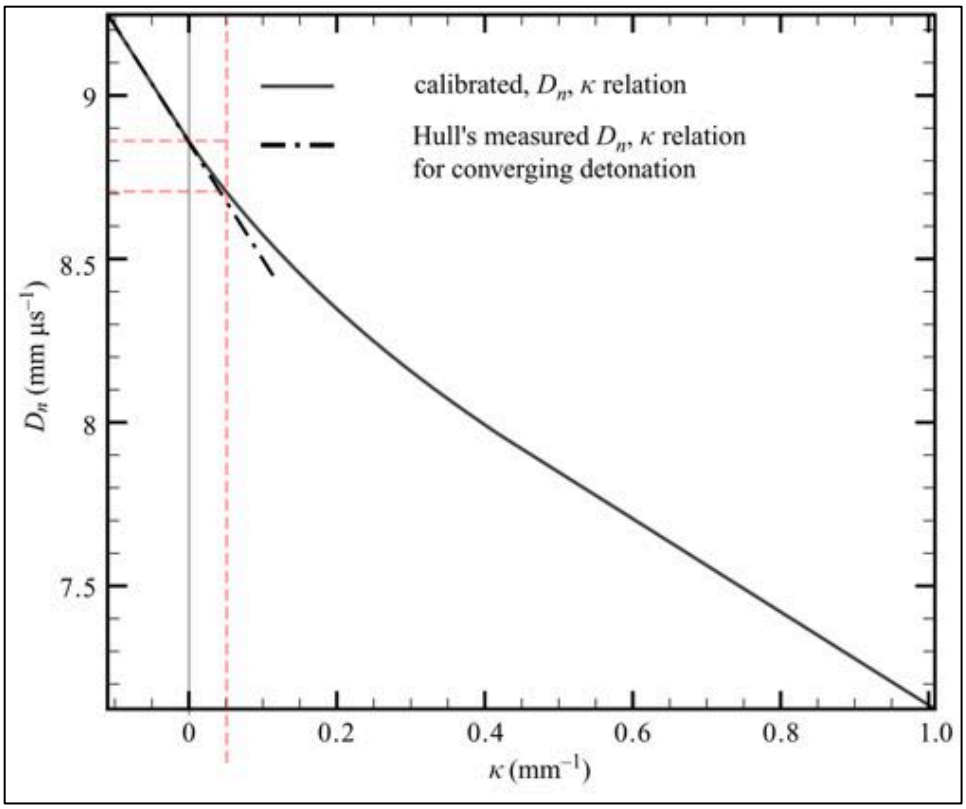

Figure 54. Detonation-front curvature-effect curve for PBX 9501 from DSD theory, reproduced from reference [33]. D_n is detonation velocity normal to shock direction and κ is shock curvature. Hashed red lines were added to identify the curvature of the 1.5-inch diameter experiment (r = 19 mm, 1/r = 0.05 mm^{-1}). Detonation velocity is decreased from 8.8 km/s to 8.7 km/s, a 1% decrease.

4.3. Hydrocode simulations of idealized detonation to illustrate shock attenuation

Conditions at the leading edge of the shock determine the initial shock pressure delivered to the stainless-steel, and in the idealized detonation the leading edge of the shock is expected to exhibit nominal CJ pressure. However, the shape of the rarefaction wave behind the leading shock will be affected by charge size (larger charge will have a flatter pressure pulse), and the rarefaction wave will overtake and attenuate the inert shock as it passes through the steel. Our analytical "idealized shock analysis" calculated shock pressure in the steel at the explosive-steel interface, but neglects shock attenuation as it transits the 4 mm thickness of the steel.

To address the attenuation that is anticipated in the idealized scenario, we performed simple hydrocode simulations using CTH [34]. Again, these simulations consider only pristine PBX 9501 undergoing a nominal CJ detonation to obtain a "worse-case" benchmark for maximum jump-off velocity that could be achieved. The simulation assumes zero air gap between the explosive and the stainless shell. The explosive is initiated at a center point using the steady-state detonation characteristics for pristine PBX 9501.

Figure 56 shows the attenuation of shock pressure, in the simulations, from the explosive-steel interface to the external jump-off surface at which velocity is measured. Note that initial shock pressure is identical for all diameters, at ≈43 GPa. This pressure is not the 60 GPa predicted using the previous analytical approach. However, it is known (and was observed) that the peak shock pressure reported in the CTH simulations is mesh-size dependent. The results presented in the figures originated from simulations which used a 2D cylindrical mesh with a resolution of 25 μm. Limited mesh resolution studies were conducted, sufficient to observe that peak pressure in the simulation continues to rise as the mesh resolution is reduced. Efforts to establish an asymptotic peak pressure were abandoned when computing times became prohibitive. Regardless, the point of the simulations was to characterize the attenuation through the thickness of the steel, and for that purpose they were successful.

We see from Figure 55 that attenuation is greatest for the smallest charge size, as anticipated, and that for all four charge sizes the pressure at the steel-air interface is considerably attenuated. The predicted wall jump-off velocities that would be observed using PDV are shown in Figure 56. Again, we would caution the reader about trusting the initial jump-off peak from these hydrocode simulations, as it demonstrates mesh resolution dependence. Nevertheless, the qualitative trends as a function of charge diameter are valid. Additionally, we will see that the predicted terminal velocity of fragments approximately agrees with the Gurney analysis presented in the next section.

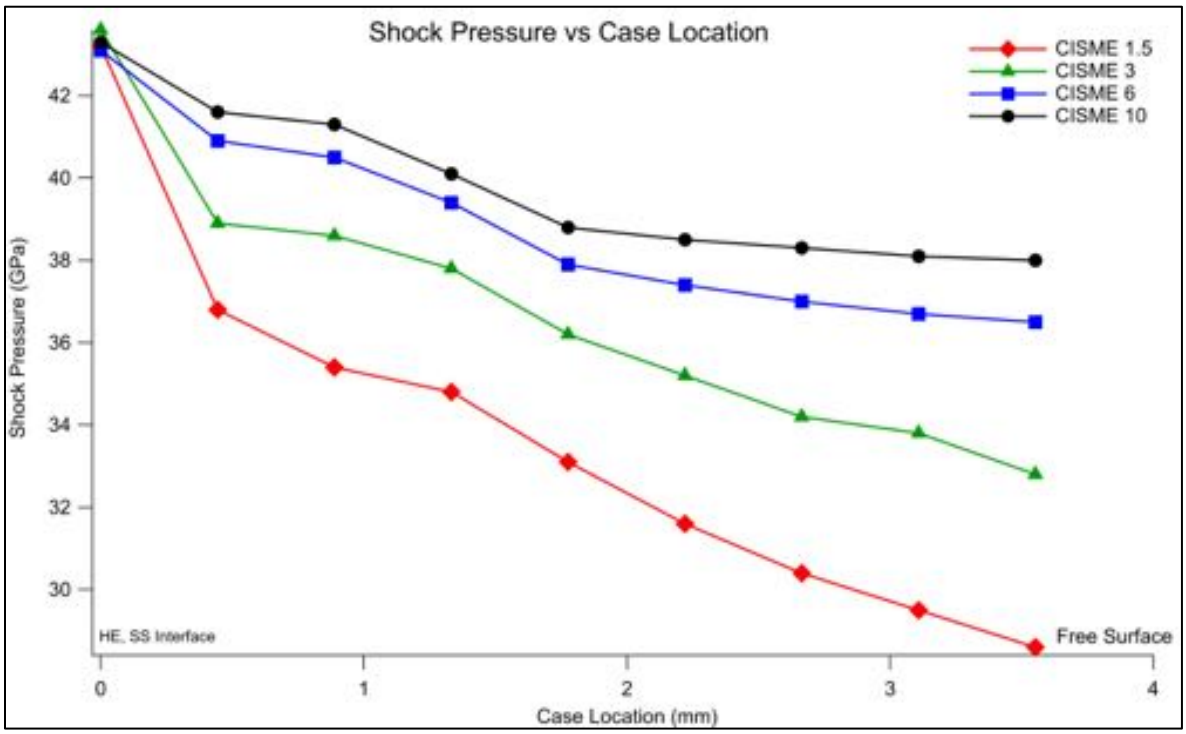

Figure 55. CTH shock pressure attenuation through the thickness of the stainless shell.

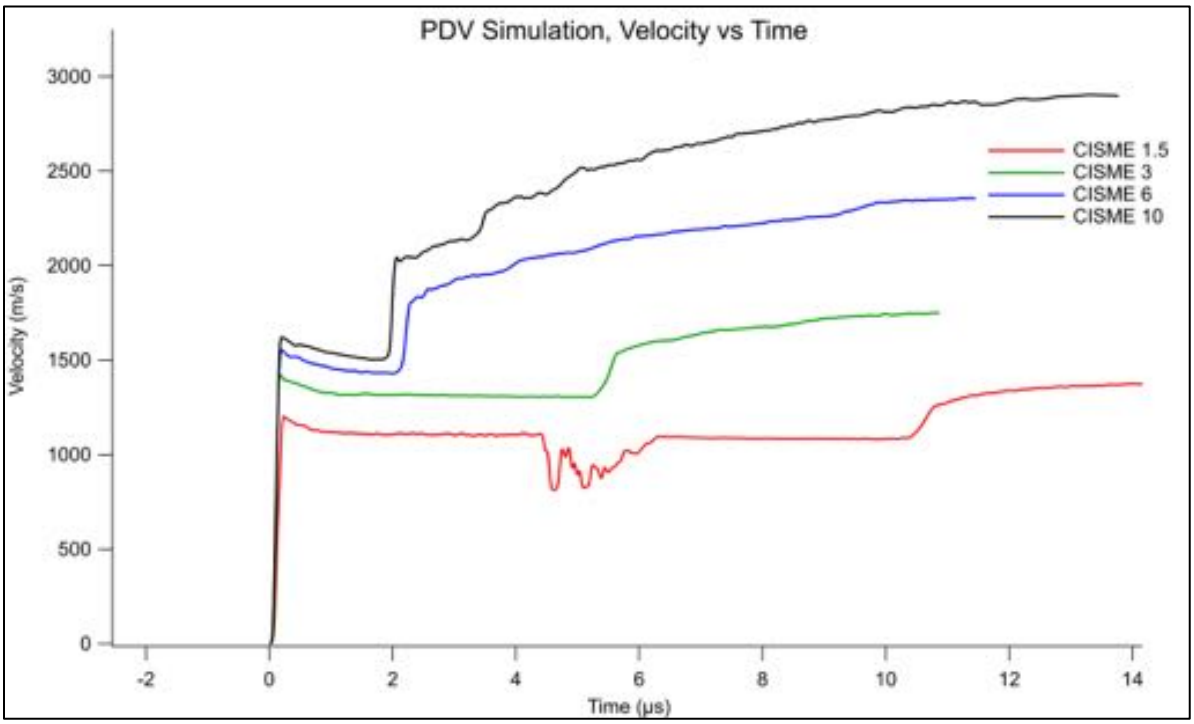

Figure 56. CTH baseline predictions for steel jump off velocity, pristine PBX 9501 only, as a function of diameter.

4.4. Gurney Analysis for pristine PBX 9501 CJ detonation

We consider again the idealized scenario in which each of our sphere diameters experiences a nominal detonation in pristine PBX 9501, as would occur for instance if the experiment was center-initiated with a detonator. The jump-off velocity of the external surface of the steel is the same for all charge diameters; it is a function of the shock interactions only. However, the terminal velocity to which the metal is accelerated *is* a function of charge diameter, and provides an estimate for the total energy released in the dynamic event for comparison with experiment results. It may be the case that an experiment exhibits no shock at all, yet manages to eventually accelerate fragments to high velocity at later times. Depending on the application, the terminal velocity of fragments may prove more important than the rate of acceleration. For example, when assessing the possibility for an event to cause a sympathetic detonation in another charge via fragment impact, the terminal velocity is important; the initial shock jump-off velocity is not.

We use the Gurney approximation [32] to calculate the anticipated terminal velocities for a perfect detonation of pristine PBX 9501. The terminal velocity for a spherical casing accelerated by a spherical charge is given by:

$$v_m = \sqrt{2E_G}\left(\frac{m}{c}+\frac{1}{2}\right)^{-\frac{1}{2}} \tag{5}$$

Where v_m is the terminal velocity of the metal casing, m is the mass of the metal fragments, c is the explosive charge mass, $\sqrt{2E_G}$ is the Gurney velocity, and E_G is the Gurney Energy. For each experiment size, the mass of the sphere is taken as an idealized shell with thickness 4 mm and internal diameter equal to the nominal charge diameter. For the Gurney velocity of PBX 9501, we use we use the assumption [32] that generally the Gurney velocity is ~D_v/2.97 where D_v is the detonation velocity of an explosive charge—in this case 8.9 km/s—yielding the Gurney velocity of 3.0 km/s. The terminal velocity for each diameter is shown in Table 20.

Table 20. Terminal velocity prediction from Gurney analysis.

Diameter (inch)	m = mass of steel shell (g)	c = mass of explosive (g)	Terminal velocity from Gurney analysis (km/s)
1.5	176.4	53.1	1.53
3	638.7	425	2.12
6	2427.6	3400	2.72
10	6605.3	15740	3.13

4.5. PDV evidence for DDT from Experiment

Each shot was diagnosed with 12 PDV probes. The probe locations are illustrated in figure Figure 57. The PDV diagnostics captures the particle velocity of the exterior surface of the metal shell. In the following analysis, we assume that we have sufficient spatial coverage of the outer surface to capture the range of behavior for the purposes of determining whether DDT did or did not occur.

We use the presence and magnitude of a shock appearing in the PDV data—identified as a discontinuous rise in velocity—as evidence whether a DDT event has occurred in the explosive. A detonation in the explosive *will* produce a shock in the stainless shell—lack of a shock is definitive evidence that that no DDT has occurred. However, a sub-detonative deflagration could possibly produce a shock in the steel. To establish whether the observed steel shock originated from a DDT event, we analyze the magnitude of the velocity jump of the shock features (if they are present) in the PDV records[3].

[3] While the discontinuous shock features in the PDV record can provide evidence for DDT, the terminal velocity of fragments cannot. A sub-detonative reaction is capable of accelerating fragments to the same terminal velocity as would a detonation; the terminal velocity is a function of total energy release, and is not sensitive to the rate of release. Therefore, for the purposes of distinguishing between deflagration and detonation, the highest velocity observed at late times with PDV is not helpful; the case for DDT must be based on a velocity jump associated with a shock feature.

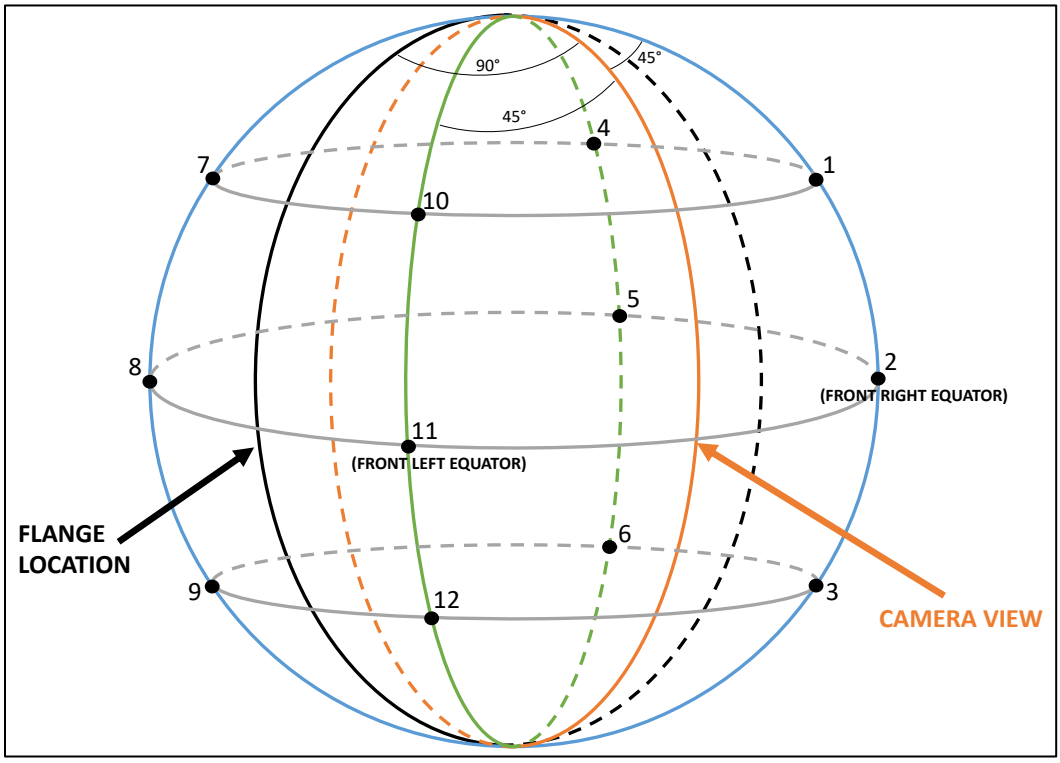

Figure 57. Diagram indicating locations of the PDV probes.

We first identify shock events in the PDV record and extract a jump-off velocity u_j for those shocks. In some records we observe that the steel is smoothly accelerated prior to a shock event; in these cases, the jump off velocity is taken to be the peak shock velocity u_f minus the existing velocity immediately prior to shock arrival, u_i. Refer to Figure 58 for an annotated example of a spectrogram with an initial acceleration followed by shock arrival.

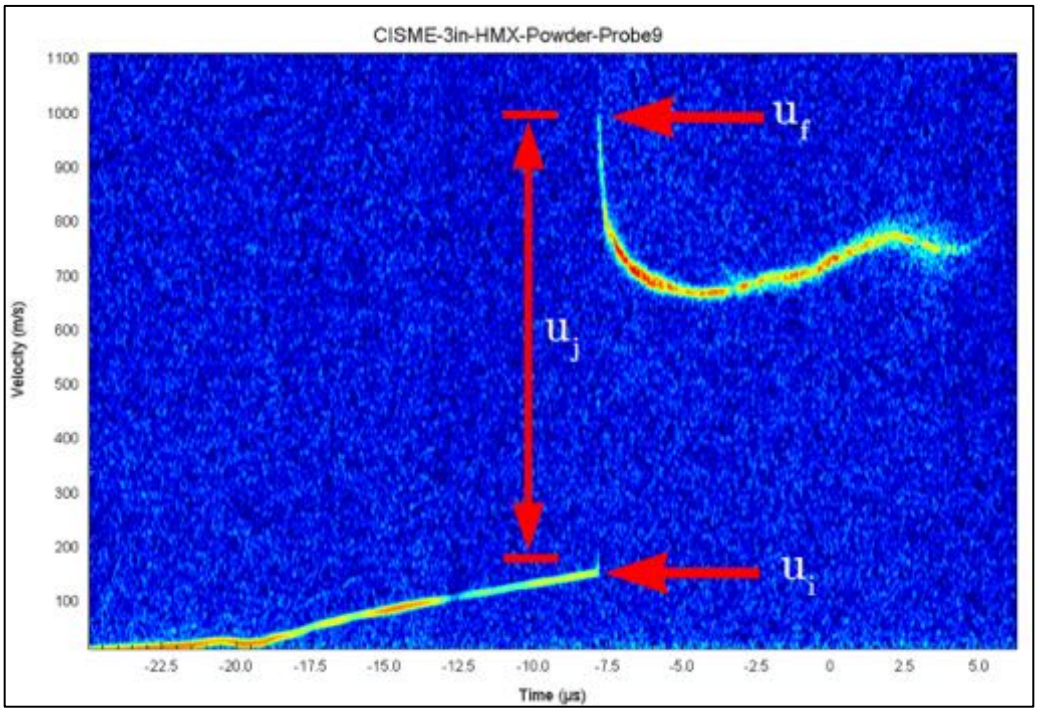

Figure 58. Example spectrogram with annotations identifying features used in the analysis. This spectrogram is from Test 1 (3-inch diameter HMX powder), probe 9.

Let us present a notional sequence of events: there exists an original, outgoing pressure wave in the explosive, of unknown pressure. This outgoing pressure wave encounters the explosive-steel interface. At the interface we get a forward-going, inert shock in the steel, and a reflected shock back into the explosive. The outgoing shock in the steel transits the thickness of the shell to cause a jump-off velocity on the surface that is twice the particle velocity in the steel. Using the jump-off velocity, we can calculate the shock pressure in the steel which produced the observed surface velocity. This is the shock pressure within the steel after it transited the 4 mm thickness. We know that attenuation within the steel reduced the shock pressure from the initial explosive-steel interaction (but not how much). However, neglecting attenuation, the shock that would have been reflected back into the explosive at the explosive-steel shock interaction is equal to steel shock calculated from PDV data.

We use this reflected shock pressure calculation to demonstrate that the reflected shock pressure into the explosive was high-enough to promptly initiate PBX 9501, even if it were not already detonating. Any attenuation of the shock in the steel, which we neglect, would only serve to underestimate the magnitude of the reflected shock into the explosive, and strengthen the argument. Note that it is unnecessary to make any assumptions about the explosive for this calculation.

We compare the calculated pressure of the reflected wave which passed back into the explosive to the known shock initiation sensitivity for pristine PBX 9501[4]. If the pressure of this reflected wave is sufficiently high—such that it would cause a prompt detonation were it to pass into unreacted material upon reflection—then it is immaterial whether the explosive was *already* detonating or *would* initiate upon wave reflection. The advantage of this approach is that the threshold shock pressure to initiate a detonation (≈2-3 GPa [35]) is an order of magnitude lower than the CJ detonation shock pressure in PBX 9501 (≈35 GPa). It is difficult to conclusively establish whether there existed a detonation front shock pressure of that magnitude in the explosive that led to the observed shock in the steel, because neither EOS nor Hugoniot for the damaged explosive is known. It is considerably easier to identify whether the shock reflection from the explosive-steel interface exceeded the much lower ≈2-3 GPa pressure threshold required to initiate PBX 9501.

We substitute $u_j = 2u$ into the Hugoniot for the steel (2) to obtain an expression for the reflected shock pressure in terms of jump-off velocity:

$$P_{\text{reflected shock}} = 18.04\, u_j + 2.94\, u_j^{\,2} \tag{6}$$

The "Pop-plot" for PBX 9501 plots the run distance-to-detonation x^* as a function of the input pressure P. It is most commonly plotted on a Log–Log scale. It is an empirical fit to experimental data. We will use the empirical fit shown in Equation (7), where the units of x^* are mm and P has units of GPa. This fit was obtained from reference [35] for a PBX 9501 density of 1.833 g/cc, and uses data originally from Gibbs and Popolato [31].

$$\log x^* = 1.74 - 1.46 \log P \tag{7}$$

We plot equation (6) as the blue trace in Figure 59 to show the jump off velocity as a function of shock pressure. We add to this figure the Pop-plot for PBX 9501 from Equation (7) (red trace). This figure summarizes our approach. For PBX 9501, any jump-off velocity exceeding ≈125 m/s indicates a reflected shock pressure into the PBX 9501 sufficient to cause initiation, and when jump-off velocities exceed ≈400 m/s, the reflected shock is of sufficient magnitude to cause initiation in a negligibly short run-length.

[4] We readily admit that the explosive into which the reflected wave travels is not pristine. Depending on the test, the material has been subjected to numerous phenomena, including but not limited to: outgoing pressure waves; expansion due to acceleration; macro- and micro- fracture; air gaps between cracked pieces of explosive; gaps between the explosive and the shell; partially reacted material; β → δ phase transition and thermal expansion. However, the general trend for these changes would be to increase the shock sensitivity (up to a point). The analysis based on shock initiation sensitivity of pristine PBX 9501 is therefore conservative.

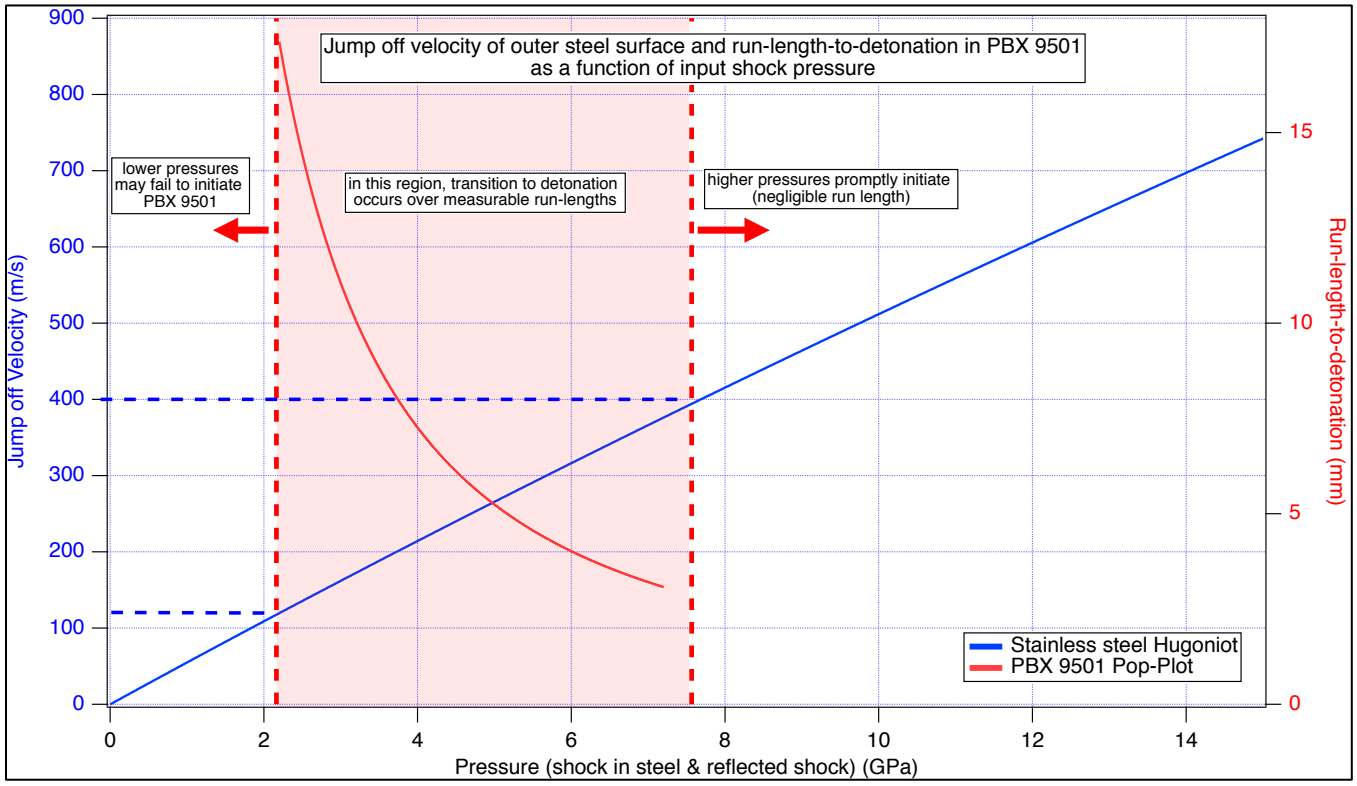

Figure 59. Shock pressure in steel shell as a function of observed jump-off velocity (blue, eq. (6)), Pop-plot fit for PBX 9501 (red, eq. (7)).

4.6. Heated PBX 9501

Two heated PBX 9501 shots were executed: Test 7 was 6-inch diameter and Test 8 was 3-inch diameter. No shock features are observed in any of the 12 PDV records for Test 8 (see spectrograms in Table 18). We conclude that DDT did not occur in the 3-inch diameter heated PBX 9501 test.

In the spectrograms for Test 7 (6-inch heated) we observe discontinuous jumps in the velocity records for probes 2, 6, 8, 9, and 12 (Table 17). For probes 2 and 9, these discontinuities occur only after a relatively long duration of smooth acceleration, indicating case expansion due to sub-detonative combustion followed by a shock front transit—hallmark features of a DDT event. The jump-off velocities were extracted from the spectrograms and are shown in Table 21 together with the calculated pressure of the shock that was reflected back into the interior explosive. The lowest jump-off velocity of these five probes was 361 m/s (Probe 12), implying a shock pressure in the steel and reflected shock pressure back into the PBX 9501 of 6.9 GPa. A 6.9 GPa inert shock into PBX 9501 will cause initiation in less than 4 mm distance, and this was the smallest shock observed. The propensity for the calculated reflected shock pressure to readily initiate PBX 9501 implies that a DDT event occurred within the explosive.

It should be noted that, as calculated in section 4.1, a CJ detonation through pristine PBX 9501 would have caused a shock pressure in the steel of 60 GPa and jump-off velocity of 2.4 km/s. Our measured jump-off velocities and calculated shock pressures are nearly an order of magnitude smaller. If the explosive was detonating, why did we observe such low jump-off velocities? Clearly, the detonation was extremely weak compared to a nominal PBX 9501 detonation. It is likely that the internal material was extremely inhomogeneous, with macro- and micro-cracking throughout. It is also likely that stress waves have passed through the material before the detonation wave transits, inciting chemistry and prematurely releasing some fraction of the energy. There may have been air gaps attenuating the shock before it passed into the steel. If the locus for the DDT event is off-center, then the resulting detonation wave can impact the steel shell at an oblique angle, reducing the observed jump-off velocity which is measured normal to the surface. We have no equation of state for hot, thermally damaged, δ phase PBX 9501, and we do not know the density of the material when DDT occurs. It is reasonable to conclude that some combination of these processes (and perhaps others unidentified) resulted in a DDT event that caused a detonation that was considerably weakened, leading to the low shock pressures and jump-off velocities that were observed relative to a CJ detonation in pristine material.

Table 21. Summary of the PDV probe data for Test 7 (6-inch thermally damaged PBX 9501) with estimated density and detonation velocity.

Probe	u_i (m/s)	u_f (m/s)	u_j (m/s)	P (GPa)	Run-length-to-detonation pristine PBX 9501
2	784	1194	410	7.9	<4 mm
6	0	842	842	17.3	<4 mm
8	755	1296	541	10.6	<4 mm
9	60	622	562	11.1	<4 mm
12	801	1162	361	6.9	<4 mm

4.7. HMX Powder

Two HMX powder shots were executed: Test 1 was 3-inch diameter and Test 2 was 1.5-inch diameter. No shock features are observed in any of the 12 PDV records for Test 2 (see spectrograms in Table 12). We conclude that DDT did not occur in the 1.5-inch diameter HMX shot.

In the 3-inch diameter HMX experiment (Test 1) at least 8 of the 12 probes (probes 1, 2, 3, 5, 6, 7, 8, 9) show a clear discontinuous velocity jump of 600-1200 m/s depicting a shock arrival(see spectrograms in Table 11). The jump off velocities for these records were extracted and are given in Table 22, together with the reflected shock pressure that is predicted from those velocities.

Table 22. Summary of the PDV probe data for Test 2 (3-inch diameter HMX) with the calculated steel shock pressure.

Probe	u_i (m/s)	u_f (m/s)	u_j (m/s)	P (GPa)	Run-length-to-detonation in HMX powder with $\rho = 1.26\,\mathrm{g/cc}$ (from [36])
1	0	740	740	14.95	<4 mm
2	187	406	219	4.09	<4 mm
3	0	1018	1018	21.4	<4 mm
5	78	673	595	11.8	<4 mm
7	0	1142	1142	24.4	<4 mm
8	75	821	746	15.1	<4 mm
9	153	949	796	16.2	<4 mm
12	388	780	392	7.52	<4 mm

In comparison with PBX 9501, low-density HMX powder is more shock sensitive than PBX 9501 (see for the Pop-plot comparisons), so the same comparison of reflected shock pressure with initiation sensitivity that was used in the previous section for PBX 9501 can be employed. Observed jump-off velocities ranged from 219 m/s to 1018 m/s. At any of these velocities, reflected shock pressure into the HMX powder would be expected to initiate a detonation in less than 4 mm of run-length. This supports the claim that DDT occurred in the 3-inch diameter HMX experiment.

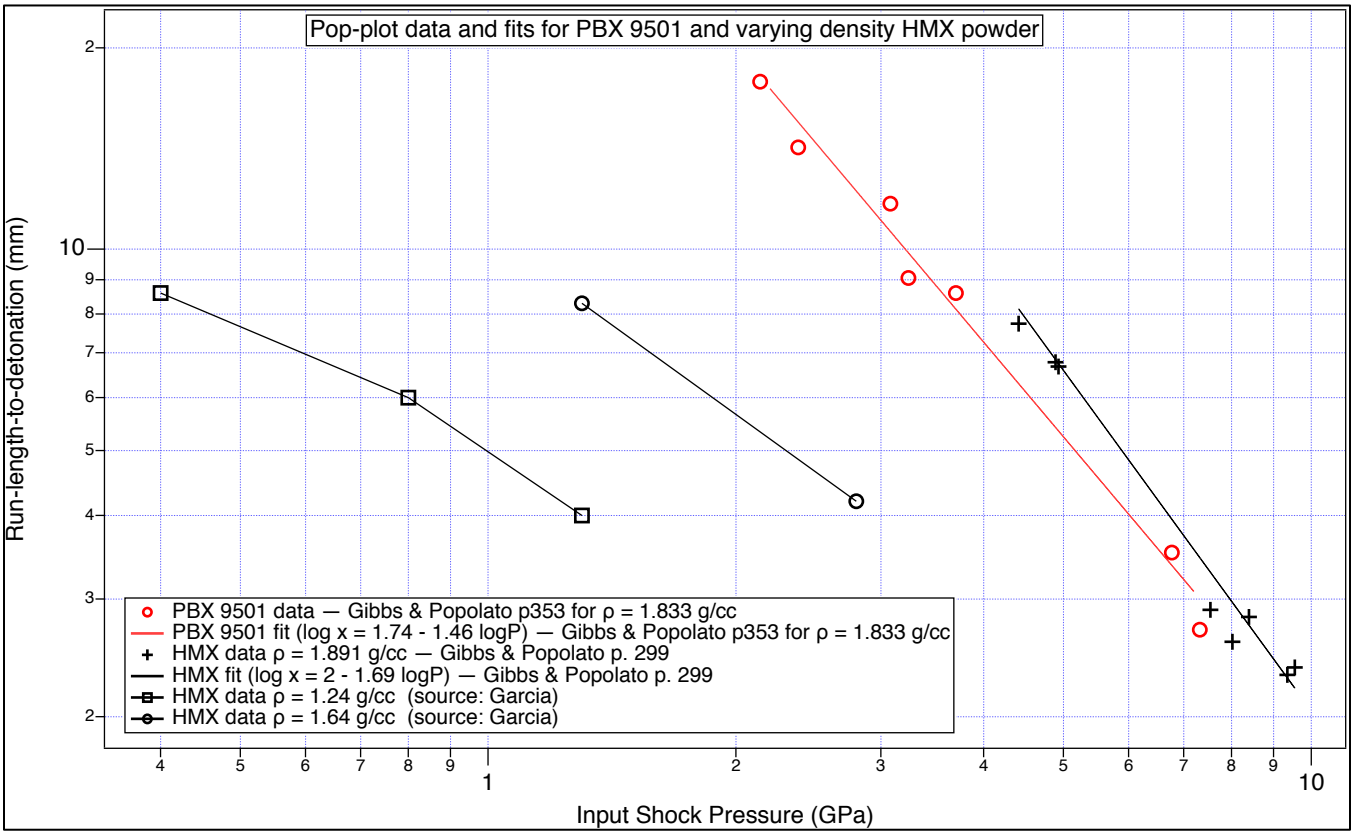

Figure 60. Pop-plots for varying densities of HMX powder, compared to PBX 9501. Data from references [31,36].

4.8. PBX 9501 Prills

No shock features are observed in any of the PDV records for any of the prills experiments, up to and including the 10-inch diameter (see spectrograms Table 13). We conclude that DDT did occur in any of the prills experiments.

5. Conclusions

Table 23. Summary matrix of test violence.

	PBX 9501 prills	Heated PBX 9501	HMX powder
1.5 inch	Sub-detonative (test 6)	Not tested	VIOLENT, unlikely DDT (test 2)
3 inch	Sub-detonative (test 5)	VIOLENT, unlikely DDT (test 8)	DDT probable (test 1)
6 inch	Sub-detonative (test 4)	DDT probable (test 7)	Not tested
10 inch	VIOLENT, unlikely DDT (test 3)	Not tested	Not tested

In the first round of CISME experiments performed in 2018, **no DDT was observed** in pristine, unheated, cased and bare PBX 9501 in any of the four sizes tested, up to and including 10-inch diameter.

Here we present the results from a second round of CISME experiments, eight tests in total, performed in 2019. In the cased testing reported here, DDT was observed with a 3-inch diameter sphere of powdered HMX but not the 1.5-inch diameter. Prills of PBX 9501 were less violent than the HMX powder, and the evidence supports a sub-detonative

reaction even at the largest diameter of 10 inches. There is evidence that heated PBX 9501 was observed to DDT at a diameter of 6 inches but not at 3 inches.

Even in the tests that DDT'd, comparison of the anticipated jump-off detonation velocity with the observed jump-off velocities implies that the detonation wave accelerating the stainless-steel shell was extremely weak compared to a nominal CJ detonation wave in pristine PBX 9501.

These results are consistent with previous DDT research. As in 1D-DDT tubes, DDT was observed with thermally damaged PBX 9501 as well as HMX powder. The run-length to detonation in quasi-1D tubes for ambient temperature HMX powder has previously been reported to range from ≈30-90 mm as a function of porosity, and the run-length for heated PBX 9501 tubes has been reported to range from ≈20-90 mm[3]. The 1.5-inch diameter HMX CISME has a radius of 19.05 mm and did not detonate; the 3-inch diameter has a radius of 38.1 mm and did detonate. The 6-inch diameter heated PBX 9501 had a radius of 76 mm and did detonate; the 3-inch diameter with a radius of 38.1 mm does not appear to have detonated. The CISME length scales are therefore consistent with previous 1D observations of the length over which DDT transpires. Comparing the radius of the charge to the run-length is a simplification; it must be noted that evolution of reaction in a spherical charge will involve complicated wave interactions, reflections, and pressure amplifications that might play a crucial role in the observed response.

The spherical geometry in CISME is the simplest possible geometry for a fully 3D experiment, making it suitable for future model validation efforts. This CISME shot series provided a successful proof of concept which can inform future investigations of higher-fidelity weapon-relevant geometries.

6. Acknowledgments

We gratefully acknowledge funding from Dan Borovina through the LANL "CHE Grand Challenge" Project. We would also like to acknowledge Darren Hanson and his team of explosive machinists for providing large, perfect spheres with small diameter blind holes drilled into explosive.

7. Data Requests

Videos of the tests as well as various other raw data can be made available on request. Please contact Matt Holmes at mholmes@lanl.gov or 505-665-4107.

8. References

[1] Holmes, M. D., Parker, G. R., Heatwole, E. M., Feagin, T. A., Broilo, R. M., et al., "Center-Ignited Spherical-Mass Explosion (CISME); FY 2018 Report" *Los Alamos National Laboratory Report: LA-UR-18-29651*, 2018.
[2] Cooper, P. W., *Explosives Engineering*, Wiley-VCH, 1996.
[3] Parker, G. R., Heatwole, E. M., Holmes, M. D., Asay, B. W., Dickson, P. M., et al., "Deflagration-to-detonation transition in hot HMX and HMX-based polymer-bonded explosives" *Combustion and Flame,* Vol. 215, pp. 295-308, https://doi.org/10.1016/j.combustflame.2020.01.040, 2020.
[4] McAfee, J. M., "The Deflagration-to-Detonation Transition" in *Non-Shock Initiation of Explosives*, *Shock Wave Science and Technology Reference Library*, edited by B. W. Asay, pp. 483-535, Vol. 5, Springer-Verlag, 2010.
[5] Asay, B. W., Parker, G. R., Dickson, P., Henson, B. F. and Smilowitz, L. B., "Dynamic Measurement of the Permeability of an Explosive Undergoing Thermal Damage" *Energetic Materials,* Vol. 21, pp. 35-39, 2004.
[6] Parker, G. R., Dickson, P. M., Asay, B. W., Smilowitz, L. B., Henson, B. F., et al., "Understanding the Mechanisms Leading to Gas Permeation in Thermally Damaged PBX 9501" *Proceedings of the Shock Compression of Condensed Matter*, pp. 1101-1104, 10.1063/1.2263515, 2005.
[7] Sullivan, G. K., "Plastic Bonded Explosive (PBX) Particle Side Distribution (PSD) Measurements Using an Image Analysis System", Type of Work, Report 2003
[8] Holmes, M. D., Parker, G. R., Broilo, R. M., Heatwole, E. M., Feagin, T. A., et al., "Fracture Effects on Explosive Response (FEER); FY2018 Report" *Los Alamos National Laboratory Report: LA-UR-18-29694*, 2018.
[9] Dickson, P. M., Asay, B. W., Henson, B. F. and Fugard, C. S., "Observation of the behaviour of confined PBX 9501 following a simulated cookoff ignition" *11th International Detonation Symposium*, Vol. 606-611, 1998.

[10] Parker, G. R., Holmes, M. D., Heatwole, E., Rae, P. and Dickson, P., "Cookoff Violence of PBX 9501 in a Quasi-2-dimensional Configuration: The Effects of Ignition Location and Confinement Strength" *Proceedings of the 15th International Detonation Symposium*, pp. 136-146, San Francisco, CA, 2014.
[11] Asay, B., "Thermal Evolution in the Large-Scale Annular Cookoff", 2003
[12] Asay, B., Dickson, P., Henson, B., Smilowitz, L. B., Tellier, L. L., et al., "Large Scale Annular Cookoff Experiment (LASC)" *JANNAF*, Vol. 1999.
[13] Zerkle, D. K. and Luck, L. B., "Modeling Cook-off of PBX 9501 with Porous Flow and Contact Resistance" *Los Alamos National Laboratory Report: LA-UR-03-8077*.
[14] Dickson, P. M., Asay, B. W., Henson, B. F., Fugard, C. S. and Wong, J., "Measurement of phase change and thermal decomposition kinetics using the Los Alamos Radial Cookoff Test" *Los Alamos National Laboratory Report: LA-UR-99-3272*, 1999.
[15] Olinger, B., "Compacting Plastic-Bonded Explosive Molding Powders to Dense Solids" *Los Alamos National Laboratory Report: LA-14173*, 2005.
[16] "MIL-DTL-45444C",
[17] Skidmore, C. B., Phillips, D. S., Son, S. F. and Asay, B. W., "Characterization of HMX Particles in PBX 9501" *Proceedings of the Shock Compression of Condensed Matter*, 10.1063/1.55666, 1997.
[18] Dobratz, B. M. and Crawford, P. C., "LLNL Explosives Handbook", 1985
[19] Type of Work: "Thorlabs FT400EMT optical fiber datasheet", ArcelorMittal.
[20] Holmes, M. D., Parker, G. R., Heatwole, E. M., Feagin, T., Vaughan, L. D., et al., "Fracture Effects on Explosive Response (FEER): FY2018 Report" *Los Alamos National Laboratory* 2018.
[21] Cady, H. H. and Smith, L. C., "Studies on the polymorphs of HMX" *Los Alamos Scientific Laboratory Report: LAMS-2652*, 1961.
[22] Parker, G. R. and Rae, P. J., "Mechanical and Thermal Damage" in *Non-Shock Initiation of Explosives*, *Shock Wave Science and Technology Reference Library*, edited by B. W. Asay, pp. 293-401, Vol. 4, Springer-Verlag, 2010.
[23] Smilowitz, L. B., Henson, B. F., Asay, B. W. and Dickson, P. M., "A Model of the b-d Phase Transition in PBX 9501" *Proceedings of the 12th International Detonation Symposium*, pp. 103-110, San Diego, CA, 2002.
[24] Dickson, P., Asay, B. W., Henson, B. F., Fugard, C. S. and Wong, J., "Measurement of phase change and thermal decomposition kinetics during cookoff of PBX 9501" *Proceedings of the AIP, Shock Compression of Condensed Matter*, p. 837, 1999.
[25] Henson, B. F., Asay, B. W., Sander, R. K., Son, S. F., Robinson, J. M., et al., "Dynamic Measurement of the HMX b-d Phase Transition by Second Harmonic Generation" *Physical Review Letters,* Vol. 82, pp. 1213-1216, 1999.
[26] Landers, A. G. and Brill, T. B., "Pressure–Temperature Dependence of the ß- ∂ Polymorph Interconversion in Octahydro-1,3,5,7-tetranitro-1,3,5,7-tetrazocine" *J. Phys. Chem.,* Vol. 84, pp. 3573-3577, 1980.
[27] Karpowicz, R. J. and Brill, T. B., "The ?-? Transformation of HMX: Its Thermal Analysis and Relationship to Propellan" *AIAA Journal,* Vol. 20, pp. 1586-1591, 1982.
[28] Parker, G. R., Dickson, P., Asay, B. W. and McAfee, J. M., "DDT of Hot, Thermally Damaged PBX 9501 in Heavy Confinement" *Proceedings of the 14th International Detonation Symposium*, pp. 941-951, Coeur d'Alene, ID, 2010.
[29] Kinney, G. F. and Graham, K. J., *Explosive Shocks in Air*, 2nd edition, Springer-Verlag, 1985.
[30] Wooten, H. O., Aslam, T. D. and Whitley, V. H., "iVCJ: A tool for Interactive Visualization of high explosives CJ states" *Los Alamos National Laboratory Report: LA-UR-16-29341*, 2016.
[31] Gibbs, T. R. and Popolato, A., *LASL Explosive Property Data*, *Los Alamos Series on Dynamic Material Properties*, edited by T. R. Gibbs and A. Popolato, University of California Press, 1980.
[32] Zukas, J. A. and Walters, W. P., *Explosive Effects and Applications*, Springer, 1998.
[33] Lambert, D. E., Stewart, D. S., Yoo, S. and Wescott, B. L., "Experimental validation of detonation shock dynamics in condensed explosives" *J. Fluid Mech.,* Vol. 546, pp. 227-253, 10.1017/S0022112005007160, 2006.
[34] CTH Hydrocode, Sandia National Laboratory, https://www.sandia.gov/CTH/.
[35] Gustavsen, R. L., Sheffield, S. A., Alcon, R. R. and Hill, L. G., "Shock Initiation of New and Aged PBX 9501 Measured with Embedded Electromagnetic Particle Velocity Gauges" *Los Alamos National Laboratory Report: LA-13634-MS*, 1999.
[36] Garcia, F., Vandersall, K. and Tarver, C. M., "Shock initiation experiments with ignition and growth modeling on low density HMX" *Journal of Physics: Conference Series,* Vol. 500, 10.1088/1742-6596/500/5/052048, 2014.

Appendix A Engineering Drawings

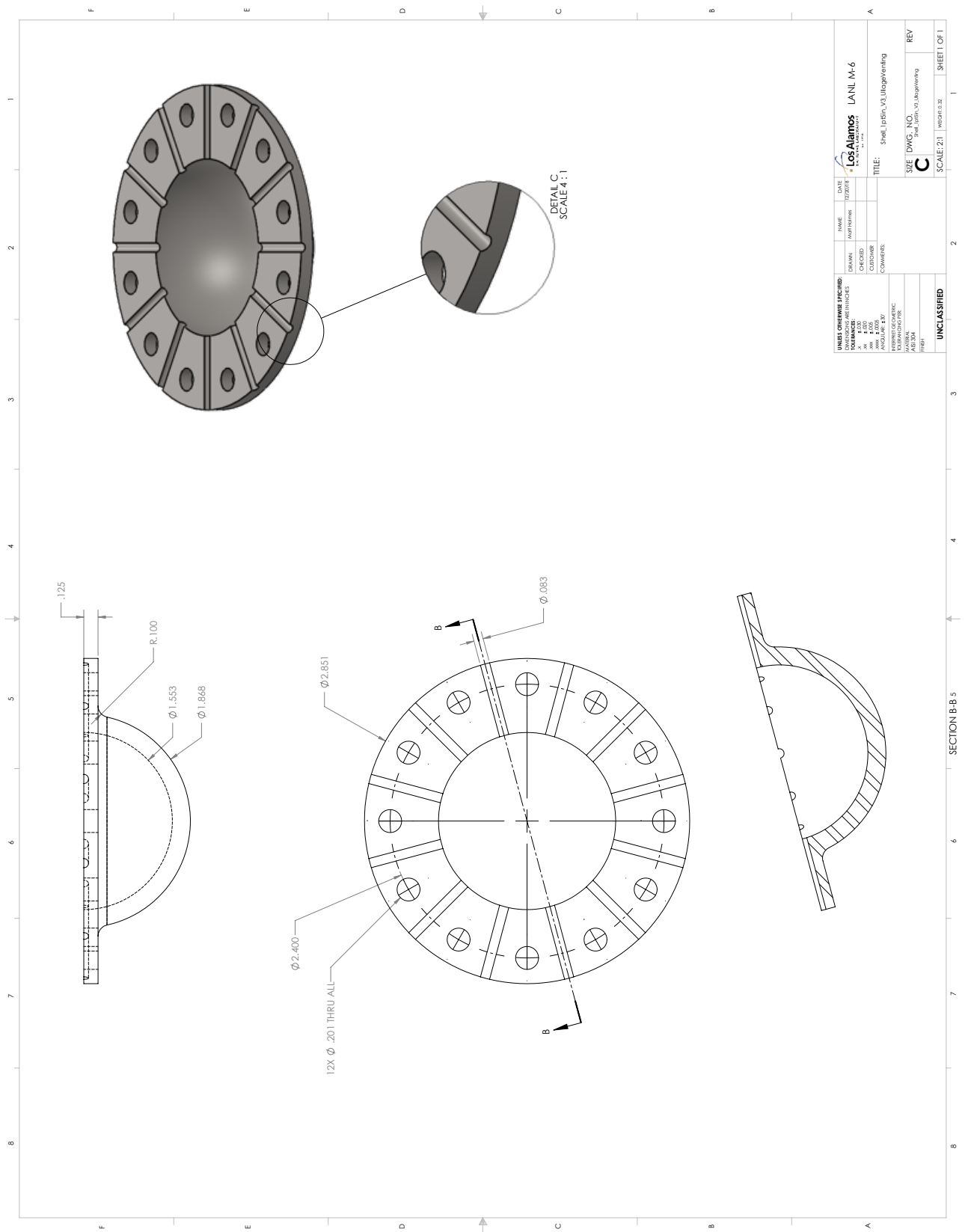

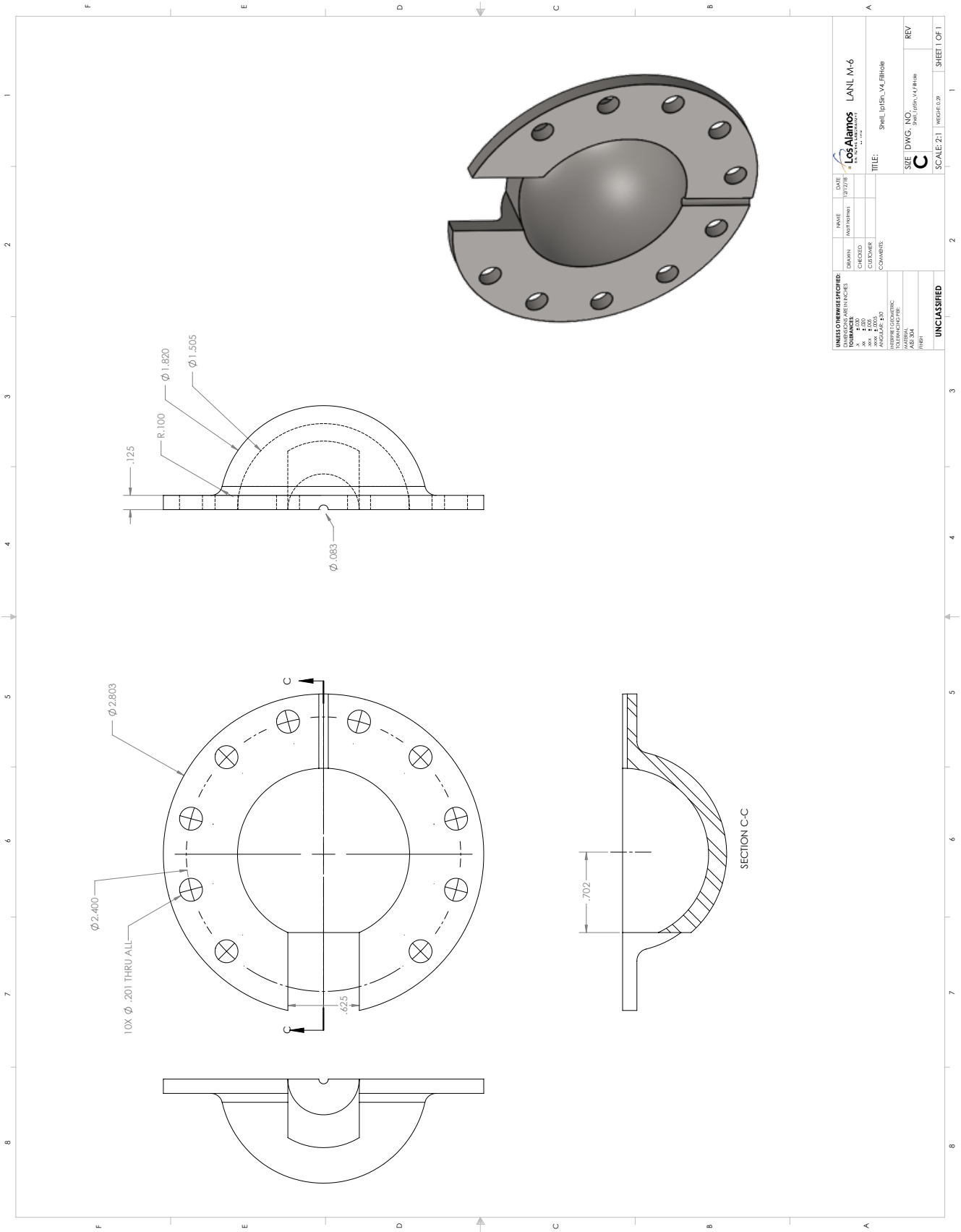
Ø1.820
Ø1.505
R.100
.125
Ø.083
Ø2.803
Ø2.400
10X Ø .201 THRU ALL
C
.625
.702
SECTION C-C
LANL M-6
Shell_lp15in_V4_FillHole
SIZE C
DWG. NO. Shell_lp15in_V4_FillHole
REV
SCALE: 2:1
WEIGHT: 0.29
SHEET 1 OF 1
UNCLASSIFIED

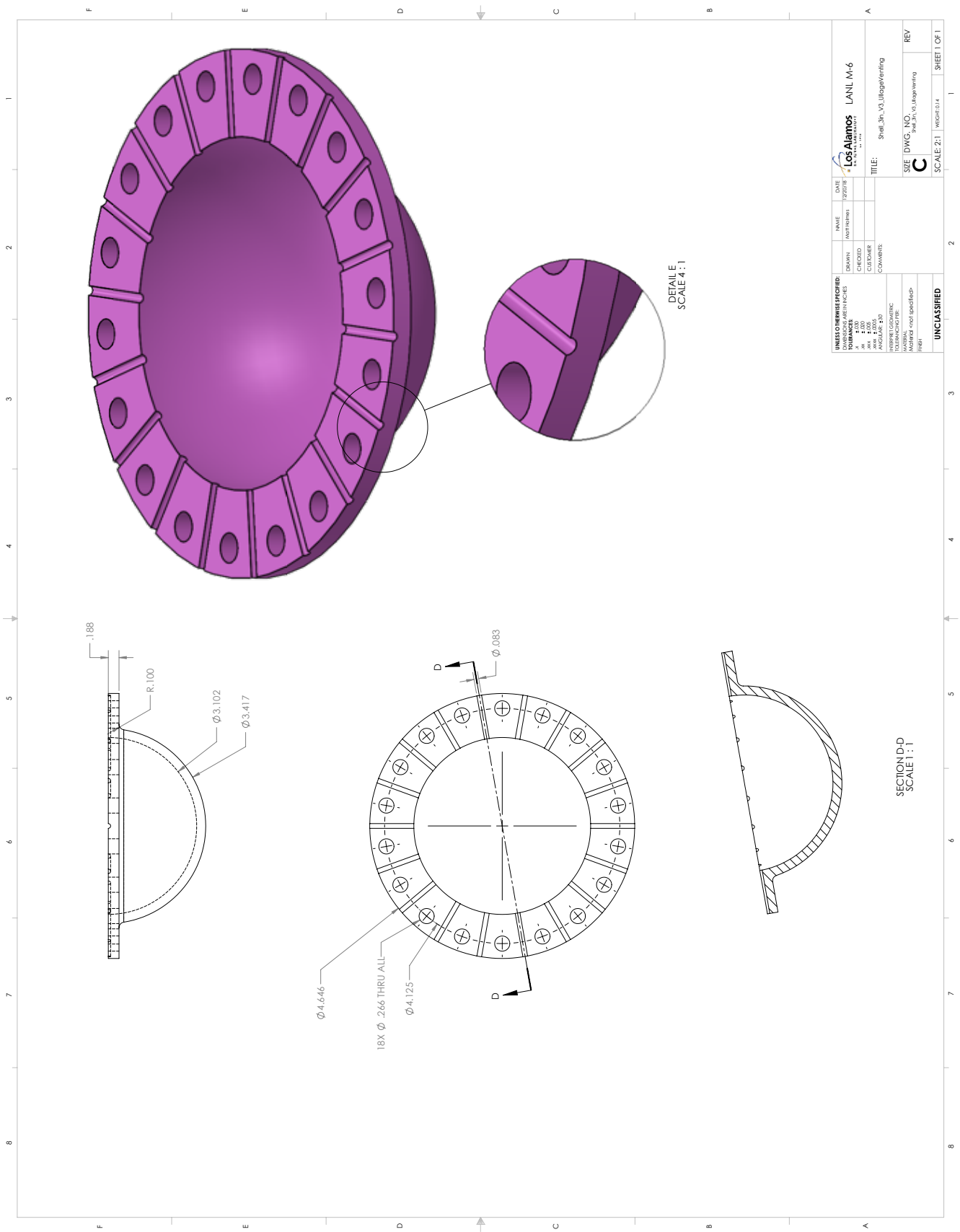
DETAIL E
SCALE 4 : 1
.188
R.100
Ø3.102
Ø3.417
Ø.083
D
D
Ø4.646
18X Ø .266 THRU ALL
Ø4.125
SECTION D-D
SCALE 1 : 1
UNLESS OTHERWISE SPECIFIED:
DIMENSIONS ARE IN INCHES
TOLERANCES:
DRAWN
CHECKED
CUSTOMER
COMMENTS:
NAME
DATE
Matt Holmes
12/20/18
Los Alamos
LANL M-6
TITLE:
Shell_3in_V3_UloggeVenting
SIZE
C
DWG. NO.
Shell_3in_V3_ULoggeVenting
REV
SCALE: 2:1
WEIGHT: 0.14
SHEET 1 OF 1
UNCLASSIFIED

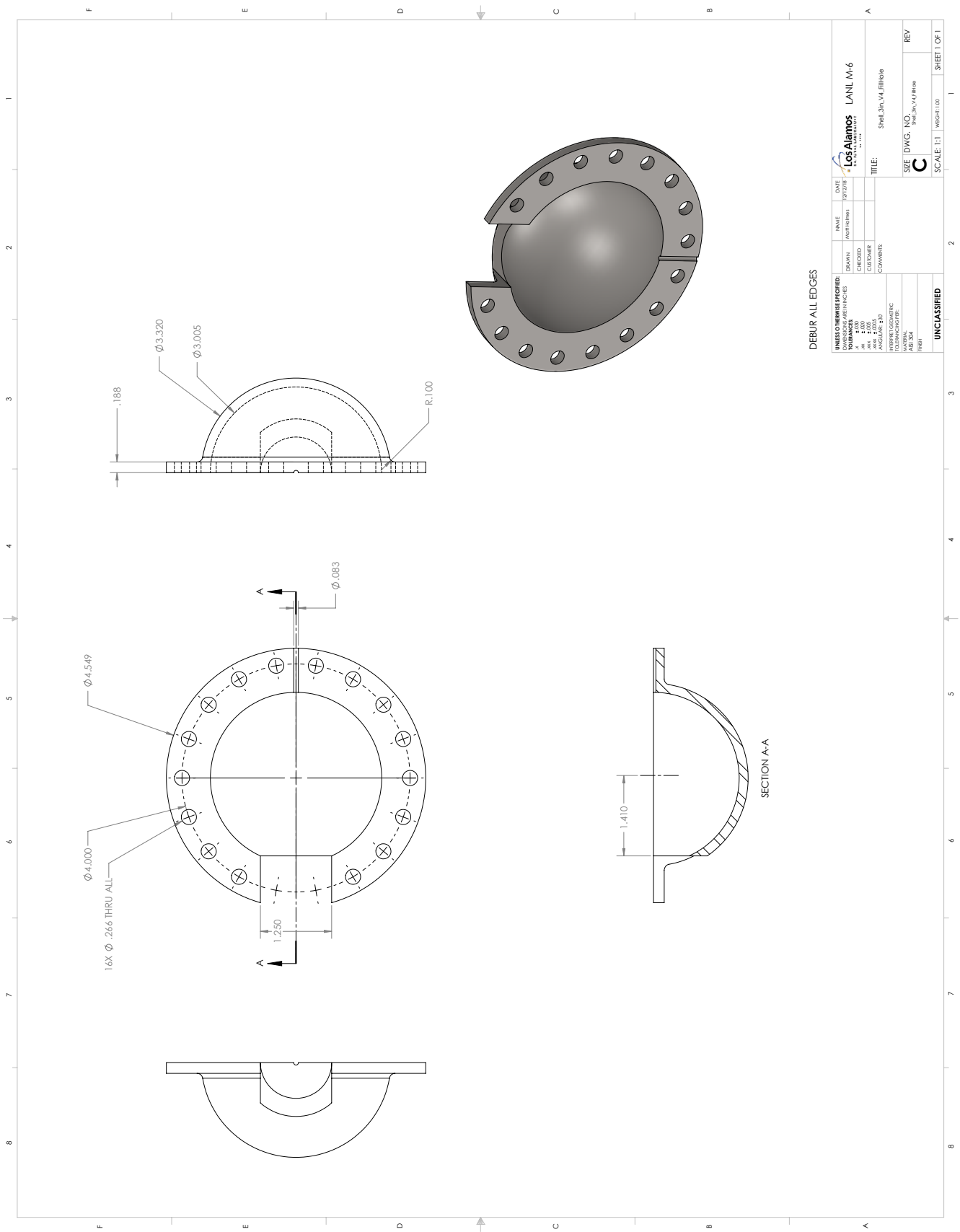
DEBUR ALL EDGES
UNLESS OTHERWISE SPECIFIED:
DIMENSIONS ARE IN INCHES
TOLERANCES:
UNCLASSIFIED
LANL M-6
Shell_3in_V4_FillHole
SIZE C
DWG. NO. Shell_3in_V4_FillHole
REV
SCALE: 1:1
WEIGHT: 1.00
SHEET 1 OF 1
Ø3.320
Ø3.005
.188
R.100
Ø.083
Ø4.549
Ø4.000
16X Ø .266 THRU ALL
1.250
SECTION A-A
1.410

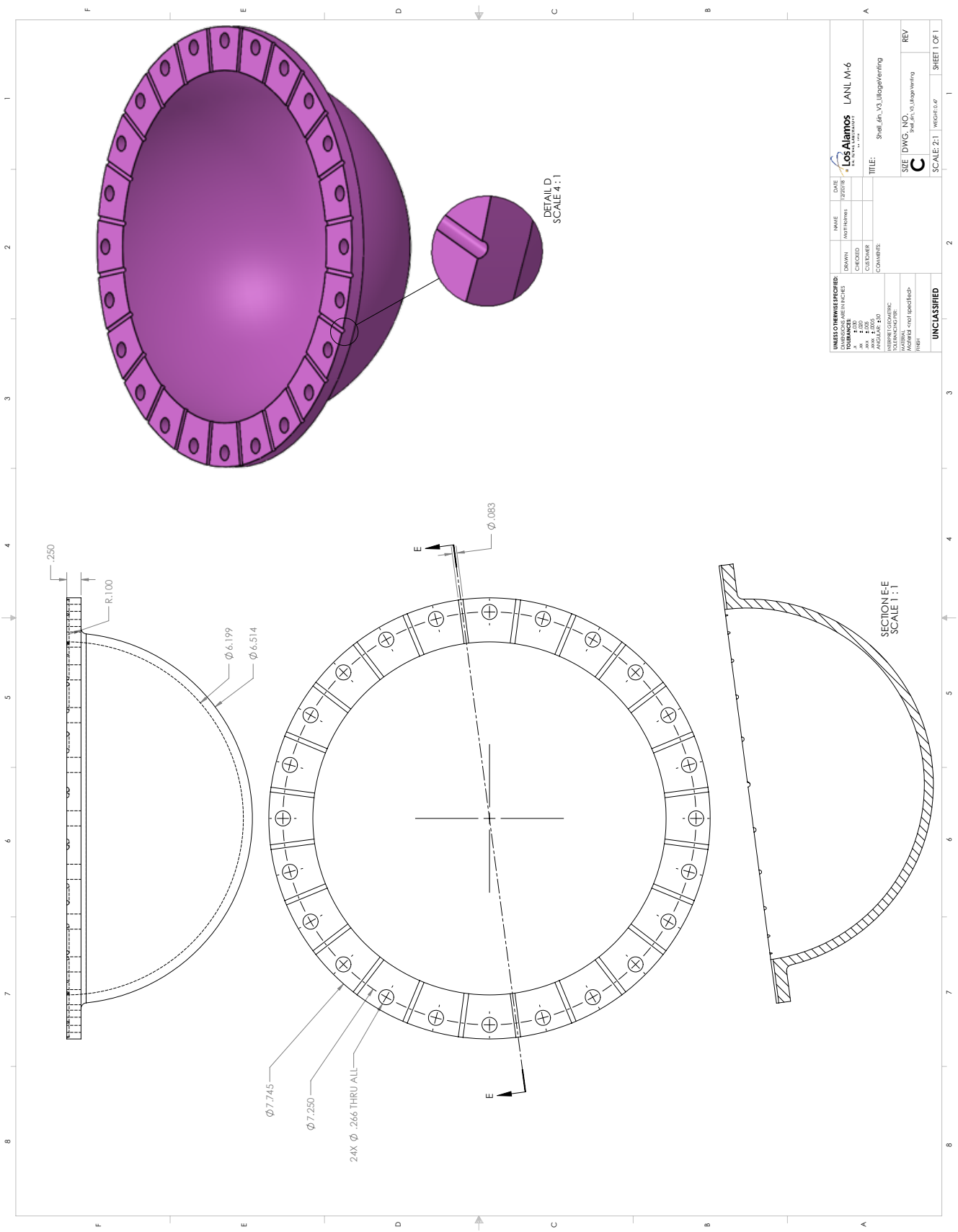
DETAIL D
SCALE 4 : 1
SECTION E-E
SCALE 1 : 1
Ø.083
Ø6.199
Ø6.514
Ø7.745
Ø7.250
24X Ø .266 THRU ALL
R.100
.250
LANL M-6
Shell_dsn_V3_UloggeVenting
UNCLASSIFIED

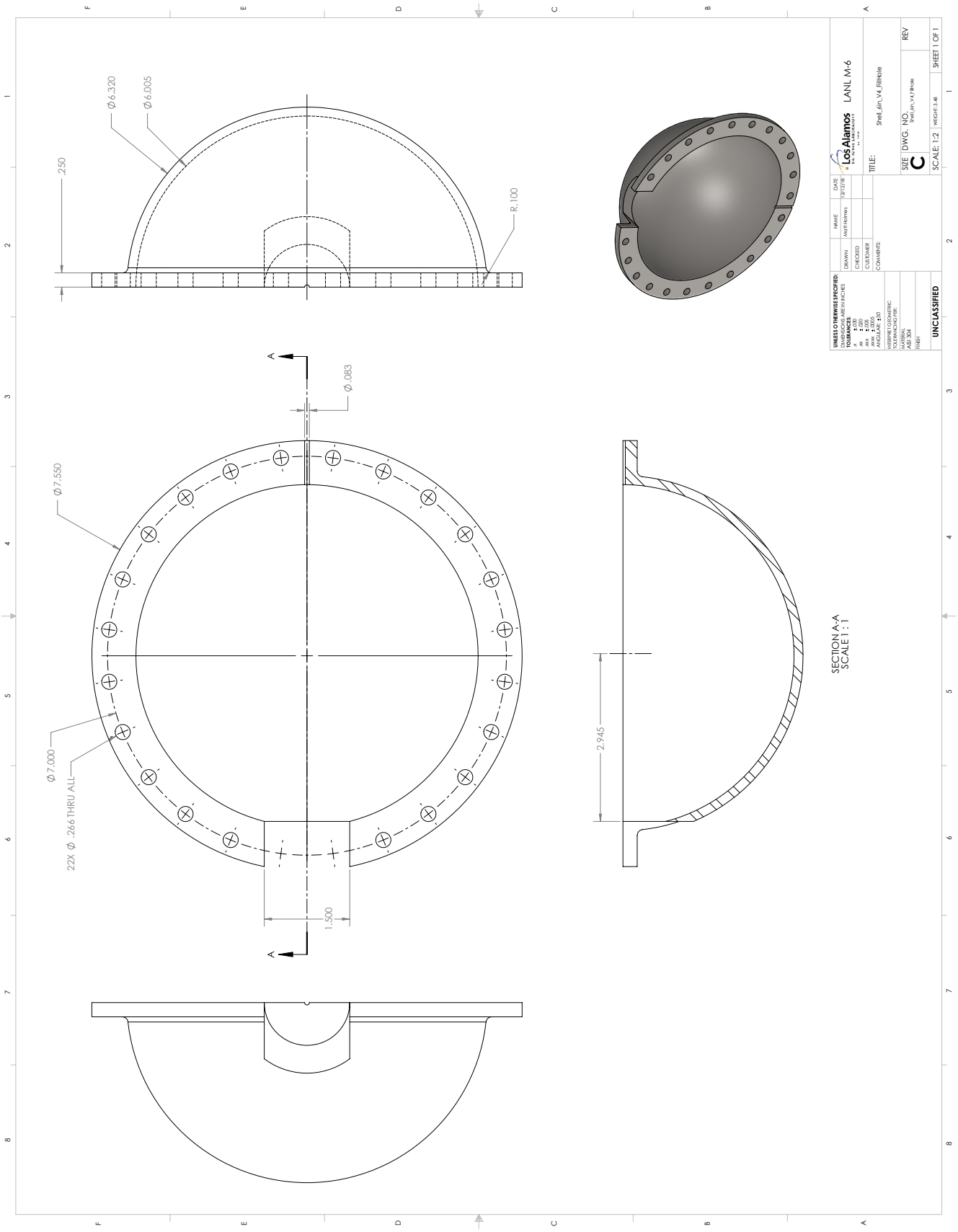
Ø6.320
Ø6.005
.250
R.100
Ø.083
Ø7.550
Ø7.000
22X Ø .266 THRU ALL
1.500
2.945
SECTION A-A
SCALE 1 : 1
UNCLASSIFIED
LANL M-6
Shell_6in_V4_FillHole
SIZE C
DWG. NO. Shell_6in_V4_FillHole
REV
SCALE: 1:2
WEIGHT: 3.48
SHEET 1 OF 1

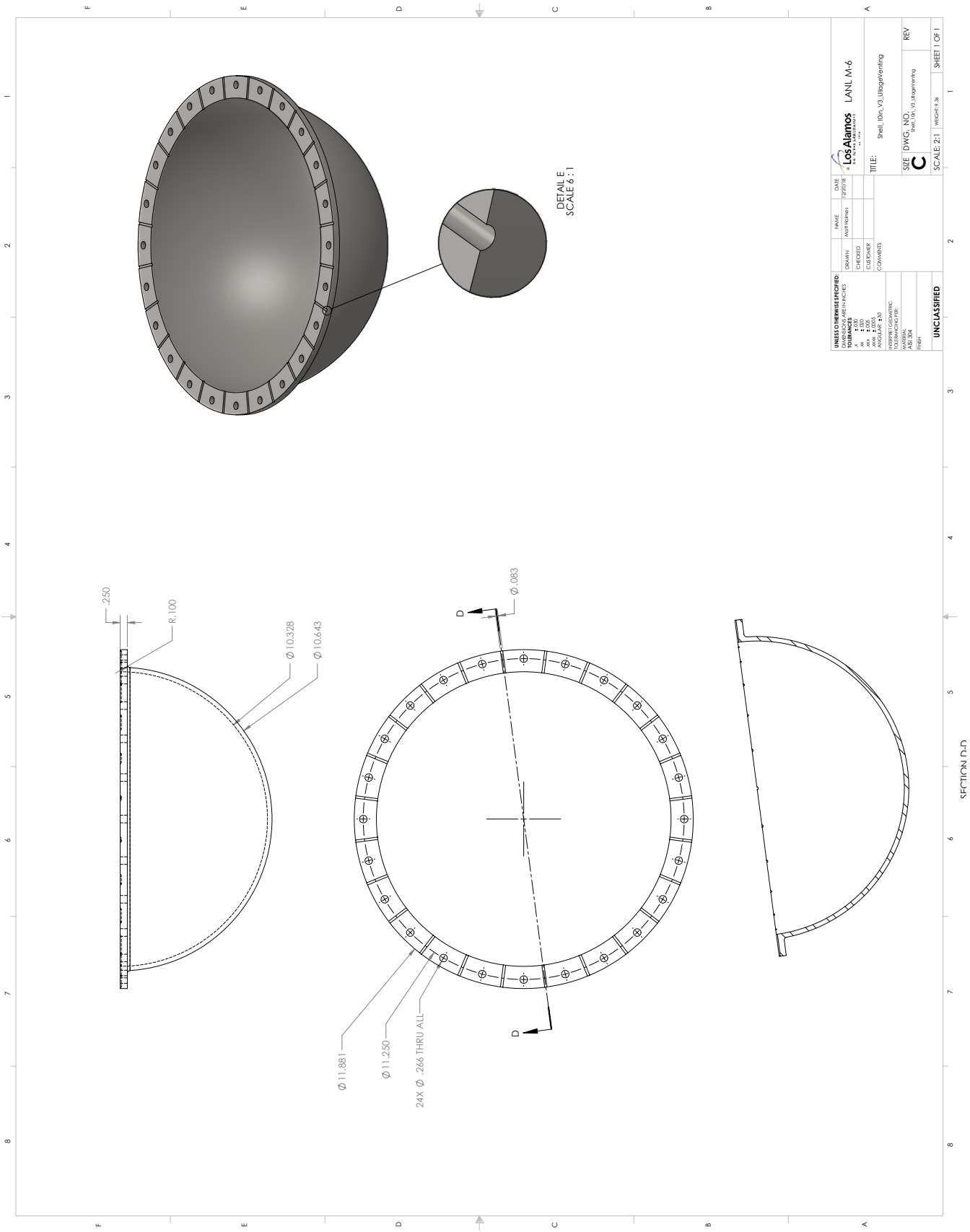
DETAIL E
SCALE 6 : 1
.250
R.100
Ø 10.328
Ø 10.643
Ø .083
D
D
Ø 11.881
Ø 11.250
24X Ø .266 THRU ALL
SECTION D-D
LANL M-6
Shell_10in_V3_UllageVenting
SIZE C
DWG. NO. Shell_10in_V3_UllageVenting
REV
SCALE: 2:1
WEIGHT: 9.36
SHEET 1 OF 1
UNCLASSIFIED

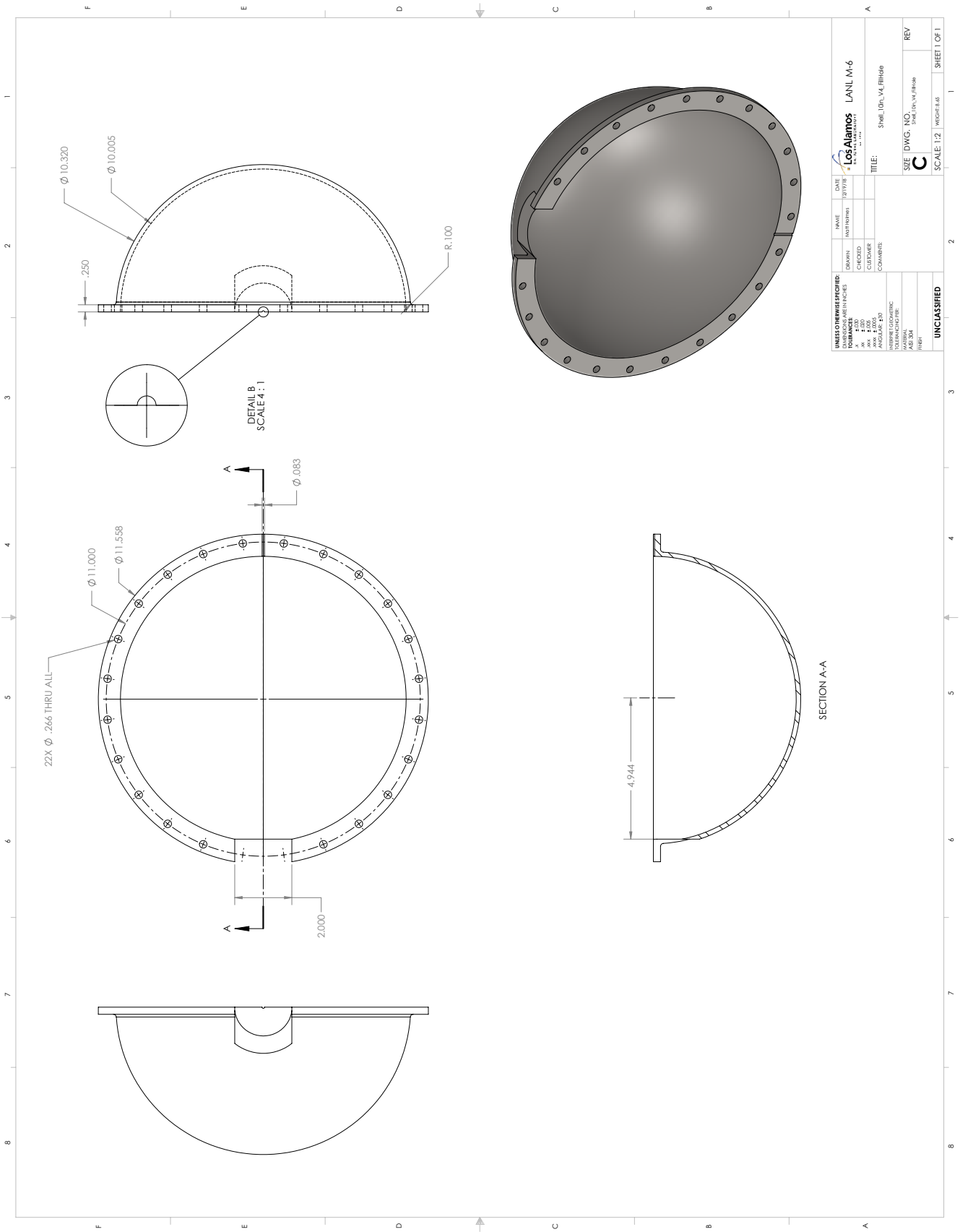
Ø 10.320
Ø 10.005
.250
R.100
DETAIL B
SCALE 4 : 1
Ø.083
Ø 11.558
Ø 11.000
22X Ø .266 THRU ALL
2.000
4.944
SECTION A-A
Los Alamos
LANL M-6
TITLE:
Shell_10in_V4_FillHole
SIZE C
DWG. NO. Shell_10in_V4_FillHole
REV
SCALE: 1:2
WEIGHT: 8.45
SHEET 1 OF 1
UNCLASSIFIED